

---

# Modeling microstructural evolution and phase transformations in material science

---

Von der Fakultät für Ingenieurwissenschaften  
der Universität Bayreuth  
zur Erlangung der Würde eines  
Doktor-Ingenieurs (Dr.-Ing.)  
genehmigte Dissertation

von  
M.Sc. Muhammad Ajmal Choudhary  
aus  
Sargodha

Erstgutachter:	Prof. Dr. Heike Ememrich
Zweitgutachter:	Prof. Dr. Hartmut Löwen
Drittgutachter:	Prof. Dr. Martin Oettel
Tag der mündlichen Prüfung:	19.07.2016

Lehrstuhl für Material- und Prozesssimulation  
Universität Bayreuth  
2016



Muhammad Ajmal Choudhary

---

Modeling microstructural  
evolution and phase  
transformations in material science

---



## My Family



# Acknowledgement

First and foremost, I would like to thank Allah Almighty for bestowing on me with the wisdom and strength to complete my PhD. This thesis would not have been possible without Allah's blessing.

I would like to express my utmost gratitude to Prof. Heike Emmerich for her support during the course of my PhD. Truly it was an honor and privilege to have had an opportunity to work in MPS. I would also like to give my sincere appreciation and gratitude to Julia Kundin for her valuable suggestions and thought provoking ideas throughout my Ph.D. It has been a great pleasure working with her on various tasks. I would also like to thank Michael Fleck, Juliane Böhm and Heiko Schoberth for their wonderful suggestions and support during my PhD. A big thanks to Paulina Horn, Henning Hörstermann, Leslie, Verena Reiss and the people I collaborated with during my PhD as well as my colleagues for the wonderful time that we spend over the years. It has been a pleasure working with all of them in terms of the countless discussions on science and otherwise, and the joint group activities which made my experience truly enjoyable. Lastly, I would like to thank all my friends for their friendship and fond memories.

Finally, a very special thanks to my family. My parents, for their unwavering love and support. No personal development could ever take place without proper guidance and prayers of parents. To my lovely daughter Barirah Choudhary, my wife, brothers, sisters and grand parents for their prayers, support and encouragement. I am truly blessed to have all of them in my life.

I would like to gratefully acknowledge the financial support of DFG for this work.



# Abstract

The main objective of the research work presented in this thesis was to develop a better understanding of the kinetics of crystal growth phenomenon where atomistic and microscale are tightly coupled as nucleation. To that end a new material science concept on atomistic length and diffusive time scales was developed further and applied to the fundamental studies of the nucleation kinetics for the binary alloy system beyond classical nucleation theory. The theoretical approach used in this thesis is the phase-field crystal (PFC) method. The originally introduced PFC approach [7] can only model certain classes of material systems with Poisson's ratio of  $1/3$ . Thus, it requires an appropriate extension of this approach to overcome these limitations and to extend the applicability of this approach to a wider range of material systems. This extension of the originally introduced PFC model to develop a more generalized model with the capability to model material systems of arbitrary Poisson's ratio [8, 9], is one of the important aims of this thesis. Furthermore, questions around the numerical efficiency as well as the recovery of physical details associated with the scale-bridging approach are also addressed by the development of the complex amplitude formalism which demonstrates the explicit connection between the PFC and PF models [10]. This development of a scale-bridging approach is an important aim of this thesis which facilitates the further advancement towards multi-scale modelling of microstructural evolution phenomena in a wide range of material systems. Finally, an application is presented which concerns a fundamental approach to study the nucleation mechanisms associated with binary systems motivated by their higher industrial relevance. This study successfully demonstrated the usefulness of the finite system size approach for a precise assessment of the equilibrium properties of the curved liquid-solid interface as well as the nucleation barriers beyond the predictions based on the classical nucleation theory and non-classical Tolman formula [12].



# Contents

<b>1</b>	<b>Thesis overview</b>	<b>1</b>
1.1	Thesis outline . . . . .	2
<b>2</b>	<b>Theoretical background</b>	<b>5</b>
2.1	Overview of the PFC method . . . . .	5
2.1.1	Phenomenological development . . . . .	8
2.1.2	Theoretical development . . . . .	11
2.1.3	Phase properties . . . . .	15
2.1.4	Elastic constants . . . . .	17
2.2	Amplitude expansion of the PFC model and its connection with the PF models . . . . .	19
2.3	Limitations of the originally introduced PFC model . . . . .	21
2.4	Further development of the PFC method . . . . .	22
<b>3</b>	<b>Modeling of anisotropic materials with arbitrary Poisson's ratio</b>	<b>25</b>
3.1	Investigation of the APFC model . . . . .	26
3.1.1	The APFC model . . . . .	26
3.1.2	Elastic properties . . . . .	30
3.2	DDFT based calibration of the APFC model . . . . .	34
3.3	Investigation of characteristic morphological features . . . . .	39
3.3.1	Anisotropic effects . . . . .	40
3.3.2	Undercooling effects . . . . .	42
3.3.3	Phase diagram . . . . .	43
3.3.4	A quantitative study of the impact of anisotropy on the result- ing microstructures . . . . .	44
3.4	Further evaluation of model parameters . . . . .	47

3.5	Bridging the PF and PFC approaches for anisotropic systems . . . . .	51
3.5.1	Amplitude expansion of the APFC model . . . . .	51
3.5.2	Connection between the APFC model and traditional PF models	56
3.5.3	Evaluation of computational efficiency . . . . .	59
3.6	Discussion . . . . .	61
<b>4</b>	<b>Investigating the equilibrium properties of the liquid-solid interface</b>	<b>63</b>
4.1	Theoretical picture of crystalline growth process via metastable nuclei	65
4.1.1	Finite size effect approach . . . . .	66
4.1.2	Existing theoretical models . . . . .	66
4.1.3	Support from computational studies . . . . .	67
4.2	PFC model for binary systems . . . . .	69
4.3	Equilibrium phase properties . . . . .	71
4.3.1	Phase diagram based on the coarse-graining assumption . . . . .	71
4.3.2	Further development of the full phase diagram in n-c-space . . . . .	74
4.4	Method of the investigation of the interfacial energy . . . . .	77
4.4.1	A theoretical picture . . . . .	77
4.4.2	Interfacial energy based on numerical analysis . . . . .	80
4.5	Simulation parameters . . . . .	82
4.6	Liquid-solid coexistence . . . . .	83
4.7	Influence of droplet size on the interfacial energy . . . . .	86
4.8	Calculation of the grand potential difference . . . . .	90
4.9	Discussion . . . . .	91
<b>5</b>	<b>Summary</b>	<b>93</b>
<b>6</b>	<b>Zusammenfassung</b>	<b>97</b>
	<b>Bibliography</b>	<b>101</b>
	<b>List of Publications</b>	<b>111</b>

# List of Figures

2.1	PFC based simulations of the crystal growth with defects in the resulting microstructure. . . . .	10
2.2	Fourier transform of the two point direction correlation function for a typical liquid. The dashed line represents the approximation to $k^4$ order. Figure follows from [29]. . . . .	14
2.3	Smooth variation of the amplitude of the density field from a finite value in the crystalline phase to zero in the liquid phase. . . . .	20
3.1	A square simulation box of size 512 x 512 with a sphere in the center to initialize the nucleus. . . . .	40
3.2	Simulation results of crystal growth calculated for $r = -0.4$ and (a) $s = 0$ (isotropic case) and (b) $s = 0.3$ (anisotropic case). . . . .	41
3.3	Form of triangles in the final triangular phase obtained with various values of anisotropic parameter. . . . .	42
3.4	Simulation results of crystal growth after 60,000 time steps for $s = 0$ and (a) $r = -0.2$ and (b) $r = -0.4$ . . . . .	43
3.5	The resulting phase diagram for the APFC model in $s$ - $r$ space. . . . .	44
3.6	Typical morphologies obtained from the APFC model (a) the crystal growth simulated at $s = 0$ and $r = -0.25$ and (b) the solidification of a crystal of the stripe phase simulated at $s = 0.5$ and $r = -0.25$ . . . . .	45
3.7	Typical stable morphologies obtained from simulations performed with (a) $s = 0.25$ , (b) $s = 0.5$ , (c) $s = 0.75$ and (d) $s = 1$ . . . . .	46
3.8	The distance between the neighboring stripes for various values of anisotropic parameter $s$ . . . . .	47
3.9	The principle reciprocal-lattice vectors of the anisotropic triangular lattice. . . . .	53

## List of Figures

---

3.10	The anisotropic crystal simulated by (a) the APFC model and (b) the amplitude evolution equation. . . . .	60
4.1	The phase diagram of the model in one-mode approximation, using $n_0 = 0$ and the parameters given in Table 4.1. It follows Figure 3 in [1].	74
4.2	The isothermal section of the phase diagram at $\Delta B_0 = 0.05$ for the parameters given in Table 4.1. Figure already published in [12]. . . . .	76
4.3	(a) A planar solid slab and (b) a solid nucleus with radius $r$ stabilized in the finite simulation box. Figure already published in [12]. . . . .	77
4.4	Typical initial states for the system size $L = 30$ unit cells and (a) $P_s = 0.1$ , (b) $P_s = 0.9$ , (c) $P_s = 0.5$ and (d) $P_s = 0.5$ (slab configurations). The x-axis represents $Lx/\Delta x$ whereas the y-axis represents $Ly/\Delta y$ . . . . .	84
4.5	The resulting (a) atomic density field and (b) the concentration field of a stabilized solid crystal in the surrounding liquid phase obtained from the simulations performed with $P_s = 0.2$ and $L = 30$ unit cells. The x-axis represents $Lx/\Delta x$ whereas the y-axis represents $Ly/\Delta y$ . Figure already published in [12]. . . . .	85
4.6	The resulting (a) atomic density field and (b) the concentration field of a stabilized liquid droplet in the surrounding solid phase obtained from the simulations performed with $P_s = 0.8$ and $L = 30$ unit cells. The x-axis represents $Lx/\Delta x$ whereas the y-axis represents $Ly/\Delta y$ . Figure already published in [12]. . . . .	86
4.7	Equimolar excess free energy density ( $F_{I,\text{equim}}/A_{\text{box}}$ ) as a function of the solid fraction ( $P_{s,\text{equim}}$ ) for various system sizes. Figure already published in [12]. . . . .	87
4.8	Equimolar interfacial line tension ( $f_{I,\text{equim}}$ ) as a function of the equimolar radius of the droplet ( $r_{\text{equim}}$ ) obtained from simulation performed for various system sizes. The dotted line is the interface tension for the slab configuration. Figure already published in [12]. . . . .	88
4.9	The difference in grand potential (nucleation barrier) $\Delta\Omega$ as a function of the equimolar radius $r_{\text{equim}}$ calculated from the numerical simulations for various system sizes and the predictions based on CNT ( $\Delta\Omega_{\text{CNT}}$ ). Figure already published in [12]. . . . .	91

## List of Tables

4.1	Values of the model parameters used in the simulations. . . . .	83
4.2	Initial values of $n_0$ and $c$ for the liquid and solid phases. . . . .	83
4.3	Typical values of the chemical potentials ( $\mu_n$ and $\mu_c$ ) for both phases at coexistence state with $P_s = 0.2$ . . . . .	86
4.4	Values of the fitting parameters for the resulting expression of inter- facial energy obtained from PFC based simulations. . . . .	89



# Nomenclature

## Abbreviations

APFC	Anisotropic phase-field crystal
CNT	Classical nucleation theory
DDFT	Dynamical density functional theory
DFT	Density functional theory
DIT	Diffusion interface theory
KMC	Kinetic Monte Carlo
MC	Monte Carlo
MD	Molecular dynamics
PF	Phase-field
PFC	Phase-field crystal

## List of Symbols

$\psi$	Phase-field variable
$\phi$	Order parameter
$M$	Mobility
$s$	Anisotropic parameter
$\nu$	Poisson's ratio
$c_0^{(2)}$	Two point direct correlation function
$q_0$	Wavelength of the system
$\sigma$	Dimensionless deformation
$K_B T$	Thermal energy
$n$	Atomic density field
$c$	Concentration field
$p$	Pressure at liquid-solid coexistence
$\mu_c$	Chemical potential
$\Delta\mu$	Difference of chemical potential between solid and liquid phase
$\gamma$	Surface tension
$\gamma_\infty$	Surface tension of a planar liquid-solid interface
$f_I$	Liquid-solid surface tension
$\delta_T$	Tolman length
$\Delta\Omega$	Nucleation barrier

# 1 Thesis overview

Over the past several decades, a tremendous amount of research has gone into the development of fundamental understanding of the nucleation kinetics and the evolution of successive initial microstructure formation processes which play a key role in the determination of material properties. The specific features of the resulting microstructures are often directly related to the metastable equilibrium state of the system, which usually arises during the processing stage. Many formalisms for calculating the equilibrium states were established by Gibbs, Boltzmann and others. However, there are many systems which never reach an equilibrium mainly due to the existence of metastable states. The presence of such nonequilibrium states strongly influences several material properties, for example, the Hall-Petch equation shows that the yield strength of polycrystalline materials varies as the inverse square of the average grain size [1, 2]. Therefore, the fundamental understanding of the complex dynamics of such systems out of equilibrium has always fascinated researchers due to its wide range of applications in materials science [3, 4, 5]. A classical example of such an application is solidification, which is an important step in the processing route of several materials. In order to describe the basics of the solidification process, it is very important to understand the complex phenomena of nucleation and the phase transformations occurring during the solidification process as initial stages determining characteristic material length scales and their properties. Although the basic principles of nucleation and phase transformation processes are well known, still many details about these processes require further explanation. Hence, the understanding of the process of nucleation and successive microstructure formation is of significant importance to guide optimal design aiming at specific microstructural properties [6].

### 1.1 Thesis outline

In this section, the outline of the topics covered in the following chapters of this thesis is presented. The organization of this thesis is structured in the following way:

Chapter 2 focuses solely on the basic introduction and further development of the theoretical approaches employed in this work. More specifically, it provides a detailed theoretical description of the PFC method along with its main features and important developments that have been made in recent years. It also highlights the relationship between the phenomenological model parameters and the real material properties which provides the physical justification to the model. Finally, important recent applications of the PFC approach as well as certain limitations of the originally introduced PFC model [7] in terms of its applicability to model material systems with Poisson's ratio other than  $1/3$  are also presented in this chapter. Thus, the objective of this chapter is to set the context for the main research topics covered in this thesis in order to justify the importance of the research work presented in the following chapters as well as to present a detailed picture of the development of the theoretical foundations used in this thesis.

In chapter 3, a detailed derivation of the newly developed anisotropic phase-field crystal (APFC) model, which has the capability of simulating isotropic as well as anisotropic materials with arbitrary Poisson's ratio, is presented. Since the applicability of the originally derived PFC model [7] was limited to a certain class of material systems with Poisson's ratio of  $1/3$ , therefore, it restricts the use of the PFC approach to model certain classes of materials with Poisson's ratio other than  $1/3$  such as steel and iron (with Poisson's ratio in a range of 0.21 - 0.3). The newly developed APFC model addresses this issue due to its capability to model materials with arbitrary Poisson's ratio and thus extends the applicability of the PFC approach to a wider range of material systems. Additionally, the APFC is fully calibrated through the derivation of its model parameters from the dynamical density functional theory (DDFT), which originally provided one physical justification to the model [8]. The analysis of the stable state phases and the corresponding

phase diagram for the APFC model is also presented in this chapter. Furthermore, to address questions concerning the computational efficiency as well as the transition to microscopic scale, the derivations of the amplitude formulation for the APFC model is also presented, which explicitly demonstrates the connection between the APFC model and the standard phase-field models and thus enhances the computational efficiency by building a bridge in the multiple-scale spirit. Most parts of this chapter, including the mathematical derivations and the simulation results, are already published in [8, 9, 10].

Chapter 4 focuses on the application of the PFC method to study the nucleation kinetics associated with binary systems as a step in the direction of industrially relevant material systems. In this study, the focus was not on the capacity to model arbitrary Poisson's ratio, but rather on establishing a precise assessment of the nucleation mechanisms beyond predictions based on classical nucleation theory (CNT). More specifically, a quantitative analysis of the equilibrium properties of the liquid-solid interface by means of a PFC model for binary alloys [1] is presented in this chapter. The details of the method used for the investigations of the equilibrium properties and the corresponding simulations results are also discussed. The main objective of this chapter is to establish the usefulness of the finite system size approach to study the liquid-solid phase transition as it was successfully demonstrated as a quantitative route to assess the nucleation kinetics associated with a liquid-vapour system as well as to assess a detailed picture of the nucleation kinetics beyond CNT. The main results presented in this chapter are published in [11, 12].

Finally, chapter 5 summarizes the key findings from the simulations carried out in this thesis and presents a brief concluding discussion as well as a possible future extension of the work presented in this thesis.



## 2 Theoretical background

This chapter focuses on the fundamental development of the modeling approaches used in the following chapters and thus provides the theoretical framework for the work presented in this thesis. More specifically, a detailed review of the origins of the PFC method in the context of its phenomenological as well as the theoretical development is presented in this chapter. The deviation of the parameters of the originally introduced PFC model by means of the classical DFT provides the physical justification to the model. The derivation of important material properties in terms of parameters of the PFC model is discussed in detailed. Furthermore, important limitations of the originally introduced PFC model and the corresponding further extensions to address these issues, are also discussed. Thus, this theoretical discussion provides the foundation to elaborate the physics behind the simulation results presented in the following chapters of this thesis.

### 2.1 Overview of the PFC method

A well known mathematical description for the dynamics of systems out of equilibrium was developed by Stefan and Boltzmann [13]. Since then, the problems which involve a moving sharp interface between two phases are termed as Stefan problem. This formalism was based on the basic laws of energy conservation and heat transportation. In the last few decades, several solutions are proposed for the continuum sharp interface Stefan problems.

Another continuum approach to model such systems has followed the introduction of the PF approach. This approach has its origin in the Ginzburg-Landau [14] and Cahn-Hilliard [15] theories on the interface between the solid and its melt. It differs

## 2 Theoretical background

---

from the Stefan problem in a way that it implicitly tracks the liquid and solid phases as well as the interface through a continuum order parameter field. The PF method couples a set of uniform order parameters to one or more diffusion fields (such as temperature or concentration) and the time evolution of the relevant order parameters is governed by a dissipative dynamics, driven by a free energy functional. In this approach, the evolution process is described through one order parameter which is a continuous function of space and time, and is known as phase-field variable  $\psi(x, t)$ . The constant values of the phase-field variable (locally) represent the presence of liquid or solid phases. However, close to the interface between two phases, the values of  $\psi$  changes smoothly. Due to this smooth interface between the phases, the PF method is also known as the diffuse interface approach. It allows to model and investigate the dynamics of the interface, that change the topology during evolution of  $\psi$  with time without the need of explicit tracking of the interface. For a problem related to a two-component system, this phase-field variable represents the local composition of both components. The simplest form of the energy functional for this approach is based on the Landau form of the free energy functional and can be expressed as

$$F = \int_V \left[ \frac{\epsilon^2}{2} |\vec{\nabla} \psi|^2 + f(\psi) \right] dV, \quad (2.1)$$

where the integration extends over the fixed volume  $V$ . The first term in the free energy functional expression penalizes for the existence of the interface between the phases whereas the second term, which is commonly known as the double well free energy, accounts for the bulk free energy for various phases and sets the equilibrium states of these phases. The corresponding dynamical evolution of the field equation can be expressed as

$$\frac{\partial \psi}{\partial t} = M \left( \frac{\delta F}{\delta \psi} \right) + \eta, \quad (2.2)$$

where  $M$  represents the mobility of the system and  $\eta$  is a Gaussian random variable.

For a detailed review of the PF modeling approach and its important applications, the readers are referred to [3, 15]. The PF formalism has been successfully applied to the study of solidification phenomena [16, 17, 18, 19, 20] as well as several complex phenomena which can not be described with the traditional Stefan approach such as non-equilibrium interfaces [21], multi-phases [22, 23] and defects [24].

While the PF method has proved remarkably successful there are many properties of materials which are directly controlled by the elasticity and symmetry, therefore, elasticity, multiple crystal orientations, grain boundaries and dislocations need to be incorporated into the free energy in order to model such systems. In other words, for a more comprehensive description of such systems, the free energy functional needs to be minimized by a periodic field which will naturally ensure the inclusion of the elastic energy and symmetry properties of that periodic field. Since the traditional PF models are usually formulated in terms of fields that are spatially uniform in equilibrium, it eliminates many physical features that arise due to the periodic nature of crystalline phases such as multiple orientations, elastic and plastic deformation and anisotropy. The explicit incorporation of these features into the traditional PF models leads to a very complicated model [25] to deal with and this limitation indicates a notable restriction of the PF models. Therefore, for a proper description of the crystalline phases, a spatially uniform phase field is not a good representation since it neglects properties associated with the symmetries of a crystal lattice such as elastic and plastic deformability.

To overcome the weaknesses of the traditional PF methods, very recently a new extension to the traditional PF models has emerged in the form of the PFC method which accounts for microscopic details of crystalline solids and elastic effects [1, 7, 26, 27, 28]. In this method the phase-field variable, which is constant in the bulk phase in the PF approach, is replaced by a field that exhibits the periodic crystal structure of the solid phase. The PFC method operates on atomic length scales and diffusive time scale and thus lies in between the traditional PF models and atomistic models.

The PFC model is capable of modeling a wide range of complex phenomena involving equilibrium as well as nonequilibrium phenomena on atomic length scales.

## 2 Theoretical background

---

Unlike the traditional PF models, the periodic nature of  $\phi$  naturally incorporates many physical effects such as elastic and plastic deformations, anisotropic interfacial energy and crystal orientations, which need to be explicitly incorporated into the free energy of the traditional PF models. The diffusive time scale of PFC models is much larger compared to the characteristic time scale of MD simulations. Thus, it is a computationally more efficient alternative to MD simulations for problems where atomic to continuum scale influences are tightly coupled. For a simple application such as diffusion in gold or copper it runs  $10^6 - 10^8$  times faster than the corresponding MD simulations [29]. In that sense it provides, from the point of view of multiscale materials modelling, an interesting link between the traditional PF method [31, 32] and the MD due to the fact that it operates on atomic length scales and diffusive time scales. The phenomenological as well as the theoretic development of the PFC method are discussed in the following section.

### 2.1.1 Phenomenological development

From the point of view of the phenomenological development, the PFC method is formulated from the concepts of the Ginzburg-Landau model for order-disorder phase transformations [33] and the Swift-Hohenberg [34] formulation of an amplitude approach to describe systems, where the stable states are periodic, as e.g. the case for the Rayleigh-Benard convection. The mathematical derivation is based on an order parameter  $\phi(x, t)$ , usually considered as density function, which represents the physical probability density of the position of atoms. This order parameter describes several physical quantities such as density field, concentration and crystalline order etc. For example, for a well documented case of solidification: consider a material which is disordered at high temperature and has two stable phases at low temperature. Upon quenching the material from high to low temperature, grains of different stable phases will arise and evolve in competition with each other. For such a system,  $\phi$  represents the relative mass fraction of various phases and the constant value of  $\phi$  represents the presence of both stable phases. A simple way to approximate the free energy functional is via the sum of a bulk term and a gradient term to represent contributions from inhomogeneities. The simplest form of the energy functional for

this approach can be expressed as

$$F = \int_V f(\phi) dr, \quad (2.3)$$

where  $f(\phi)$  is the free energy density. Unlike traditional PF models, the free energy functional in PFC method is constructed for the equilibrium state characterized by a non-uniform order parameter which represents crystalline phase by a periodic function. Elder et al. proposed such a free energy functional for the PFC method to study the pattern formation problems at atomistic level [7]. Typical form of the free energy functional is given by following expression:

$$f(\phi) = f_0(\phi) + \frac{\phi}{2}(q_0^2 + \nabla^2)^2\phi, \quad (2.4)$$

where  $(f_0(\phi) + \frac{1}{2}q_0^2\phi^2)$  is the bulk contribution which reflects the thermodynamics of an infinite system, the gradient term in the expression describes the energy associated with interfaces and  $q_0$  is a constant parameter which represent the wavelength of the system. The operator  $(q_0^2 + \nabla^2)^2$  in Eq. (2.4) is similar to one used in the Swift-Hohenberg (SH) equation [34] and it favors the gradient of the order parameter. The bulk contribution term can be written in the form of polynomial function of the order parameter which is similar to the Landau free energy expression, i.e.

$$f_0(\phi) = \alpha \frac{\phi^2}{2} + \beta \frac{\phi^4}{4} + \dots, \quad (2.5)$$

where coefficients  $\alpha$  and  $\beta$  are similar to the ones used in the Landau free energy expression [33] and  $\alpha$  is proportional to the undercooling. The phase-field variable  $\phi$  can have two equilibrium phases, i.e. a liquid phase with uniform profile and a crystalline phase with periodic profile, which may further have several patterns depending on the system. The corresponding evolution equation for the PFC model can be derived by assuming dissipative dynamics with mass conservation, i.e.

## 2 Theoretical background

---

$$\frac{\partial \phi}{\partial t} = M \nabla^2 \left( \frac{\delta F}{\delta \phi} \right) + \eta, \quad (2.6)$$

where  $M$  represents the mobility of the system and  $\eta$  is the stochastic thermal fluctuations.

The strength of the PFC method lies in the fact that it has the ability to explicitly track the atomic scale motion of a process during temporal evolution over diffusive time scales, e.g. the evolution of defects as well as the local atomic arrangement of atomics can be naturally captured by the PFC description because of its atomic scale resolution. Due to this ability, it can naturally incorporate many crystallographic effects emerging directly from the atomic scale, e.g. elastic and plastic deformations and topological defects such as dislocations [7, 26], which would have to be explicitly incorporated into the free energy of the traditional PF models. Fig. 2.1 demonstrates the ability of the PFC approach to track defects explicitly at atomic level.

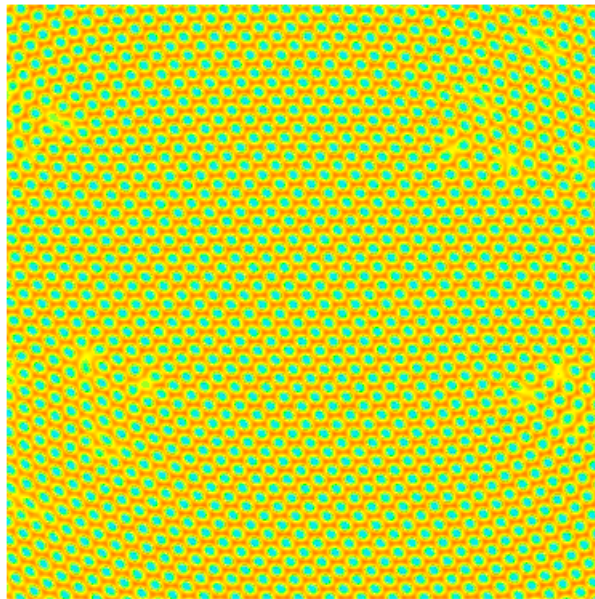


**Figure 2.1:** PFC based simulations of the crystal growth with defects in the resulting microstructure.

One of the practical challenges to the PFC method in its phenomenological develop-

ment was the modeling of real material systems and the difficulty to directly relate the model parameters with the material properties. To address these issues and to develop a better understanding of the methodological concepts of the PFC method, a verification of its phenomenological parameters via a fully established methodology as the classical density functional theory (DFT), was an important step [35].

### 2.1.2 Theoretical development

As outlined above, the PFC model was originally introduced [7] using the phenomenological arguments. Then it was further verified via a calibration of its phenomenological parameters based on the DFT [35, 36]. The theoretical development of the PFC method presented in this section follows [29, 30]. It is based on the classical DFT of freezing proposed by Ramakrishnan and Yussouff [35] and reviewed by Singh et al. [37]. This theory uses the structure factor of the liquid phase as input and then predicts a periodic density field for the solid phase and also defines the coexistence of both phases. This formulation provides the physical justification to the PFC model by establishing the relationship between the phenomenological parameters of the free energy functional of the originally introduced PFC model and the real physical properties of the material such as the elastic constants, lattice constant of crystalline phase and isothermal compressibility of the liquid phase [1]. Due to the periodic nature of the order parameter of the PFC model, it can be interpreted as the atomic density field of the system.

The first attempt to derive the PFC model from the classical DFT was proposed by Elder et al. [1]. The free energy expression of the PFC model is formulated by considering the Helmholtz free energy derived by expanding around the density of the liquid  $\bar{\rho}$ , corresponding to the liquid phase lying on the liquid side of the coexistence region. The free energy functional can be written in a generalized form as

$$F[\rho(\mathbf{r})] = F_{\text{id}}[\rho(\mathbf{r})] + F_{\text{ex}}[\rho(\mathbf{r})] + F_{\text{ext}}[\rho(\mathbf{r})], \quad (2.7)$$

## 2 Theoretical background

---

where  $F_{\text{id}}[\rho(\mathbf{r})]$  is the non-interacting ideal gas component of the free energy functional,  $F_{\text{ex}}[\rho(\mathbf{r})]$  is the excess energy component which corresponds to the higher order interactions and  $F_{\text{ext}}[\rho(\mathbf{r})]$  represents the potential energy of the interaction with external field. The expression for the free energy of a non-interacting ideal gas is given by

$$F_{\text{id}}[\rho(\mathbf{r})] = k_B T \int d\mathbf{r} \rho(\mathbf{r}) \{ \ln [\rho(\mathbf{r}) \Lambda^3] - 1 \} , \quad (2.8)$$

with  $\Lambda$  denoting the thermal de Broglie wavelength,  $T$  is the temperature and  $k_B$  is the Boltzmann constant. The expression for the  $F_{\text{ext}}[\rho(\mathbf{r})]$  can be written as

$$F_{\text{ext}}[\rho(\mathbf{r})] = \int d\mathbf{r} \rho(\mathbf{r}) V(\mathbf{r}, t) . \quad (2.9)$$

where  $V(\mathbf{r}, t)$  is the external one-body potential. It is important to mention here that an exact expression for the  $F_{\text{ex}}[\rho(\mathbf{r})]$  cannot be derived for most of the real systems, however, the contribution from the interactions between the particles can be approximated by expanding the total free energy in terms of the n-point direct correlation function  $c_0^{(n)}$ , which is defined as:

$$c_0^{(n)}(r_1, \dots, r_n; [\rho]) = (k_B T)^{-1} \frac{\delta^n F_{\text{ex}}[\rho(\mathbf{r})]}{\prod_{i=1}^{i=n} \delta \rho(r_i)} . \quad (2.10)$$

In the context of freezing, a well known approach is to approximate the by a functional Taylor expansion up to second order around a uniform density  $\bar{\rho}$ , that corresponds to the reference liquid phase density. By using the two point correlation function  $c_0^{(2)}$  and substituting all components into Eq. (2.7), the total free energy of the system can be expressed as:

$$\begin{aligned} \frac{F[\rho(\mathbf{r})]}{k_B T} &= \frac{F(\bar{\rho})}{k_B T} + (k_B T)^{-1} \bar{\mu} \int \Delta\rho(r) dr + \int \left( \rho(r) \ln \left[ \frac{\rho(r)}{\bar{\rho}} \right] - \Delta\rho(r) \right) dr \\ &- \frac{1}{2} \int dr_1 dr_2 \Delta\rho(r_1) c_0^{(2)}(r_1, r_2; [\bar{\rho}]) \Delta\rho(r_2). \end{aligned} \quad (2.11)$$

where  $\bar{\mu}$  is the chemical potential of the reference state,  $\Delta\rho(r) = \rho(r) - \bar{\rho}$ . This expression is only valid for small  $\Delta\rho(r)$ , therefore, this approximation of classical DFT indicates only the emergence of crystalline phases and can not fully describe the crystalline phase for the solidification process. The basic features of the free energy functional expression, Eq. (2.11) can be elaborated further by defining the non-dimensional atomic number density field  $n = (\rho - \bar{\rho})/\bar{\rho}$  and expanding the local portion of the free energy up to the fourth order, i.e.

$$(1+n)\ln(1+n) - n = \frac{1}{2}n^2 - \frac{1}{6}n^3 + \frac{1}{12}n^4. \quad (2.12)$$

The resulting expression for the free energy functional can be rewritten as:

$$\frac{F[\rho(\mathbf{r})]}{k_B T} = \int \left( n \left[ \frac{1 - \bar{\rho} c_0^{(2)}}{2} \right] n - \frac{1}{6}n^3 + \frac{1}{12}n^4 - \dots \right) dr. \quad (2.13)$$

The above expression can be further simplified by expanding the two point correlation function  $c_0^{(2)}$  in a Taylor series around  $k = 0$ , i.e.

$$c_0^{(2)} = \hat{C}_0 + \hat{C}_2 k^2 + \hat{C}_4 k^4 + \dots, \quad (2.14)$$

where  $C_0$ ,  $C_2$  and  $C_4$  are the fitting constants,  $k$  is the amplitude of the reciprocal vector and the hat represents the Fourier transform of the corresponding parameter. The above expression corresponds to  $\hat{C} = (\hat{C}_0 - \hat{C}_2 \nabla^2 + \hat{C}_4 \nabla^4 - \dots) \delta(r_1 - r_2)$  in real space. This approximation is relevant assuming that  $n$  varies much slower compared to the range of  $C$ . By assuming terms up to  $k^4$ , the material properties can be parameterized by three variables,  $\hat{C}_0$ ,  $\hat{C}_2$  and  $\hat{C}_4$ , i.e. lattice constant  $R \sim$

## 2 Theoretical background

---

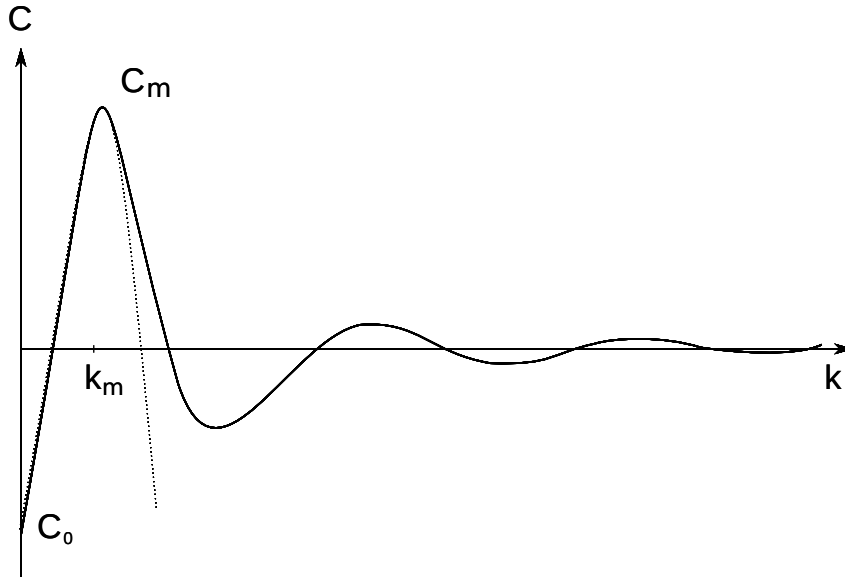


**Figure 2.2:** Fourier transform of the two point direction correlation function for a typical liquid. The dashed line represents the approximation to  $k^4$  order. Figure follows from [29].

$[(|\hat{C}_4|/C_2)^{1/2}]$ , bulk modulus of the crystal  $E \sim [\bar{\rho}C_2^2/|\hat{C}_4|]$  and the liquid isothermal compressibility  $B_l \sim [1 - \rho_l \hat{C}_0]$ . A sketch of  $\hat{C}$  for a typical liquid is shown in Fig. 2.2.

The term with  $k = 0$  in Fig. 2.2 represents the liquid phase isothermal compressibility and the height and position of the first peak is related to the bulk modulus of the solid phase and the lattice constant, respectively. With these approximations Eq. (2.13) can be further simplified as:

$$\frac{F[\rho(\mathbf{r})]}{k_B T} = \int \left( n \frac{B_l}{2} n + \frac{B_s}{2} n (2R^2 \nabla^2 + R^4 \nabla^4) n - \frac{t}{3} n^3 + \frac{v}{4} n^4 \dots \right) dr. \quad (2.15)$$

It is important to mention that with the level of simplification, it might not be enough to define all materials with only three parameters ( $\hat{C}_0$ ,  $\hat{C}_2$  and  $\hat{C}_4$ ). The originally introduced PFC model can predict a triangular phase in two dimensions and bcc structures in three dimensions [38]. These approximations can be further improved by using a higher order correlation function.

### 2.1.3 Phase properties

The equilibrium phases and the corresponding phase diagram for the PFC model can be calculated by applying the minimization procedure to the free energy functional [29]. To do so, a one-mode approximation technique is used to expand the atomic number density of the solid phase  $n$  in Fourier series and then the free energy is minimized with respect to the parameters of this expansion. For the originally introduced two-dimensional PFC model, the free energy expression is minimized by three different states by employing a periodic function of the atomic density field, namely, a constant density phase (liquid phase), one-dimensional periodic function (stripe phase) and a two-dimensional periodic function (triangular phase). The general two-dimensional periodic solution for the coexistence of liquid and stripes phases or stripes and triangular phases can be investigated by minimizing the free energy with the corresponding expansion of the density field. The atomic density field can be expanded around  $n_0$  in order to illustrate a generalized case for the liquid and triangular phases, i.e.

$$n = n_0 + \sum_{n_1, n_2} \eta e^{(i\vec{G}_j \cdot \vec{r})} + C.C, \quad (2.16)$$

where  $C.C$  is the complex conjugate,  $G$  is the sum of the reciprocal lattice vectors  $(\vec{v}_1, \vec{v}_2)$  which determine the geometry of the crystal lattice, i.e.

$$G = n_1 \vec{v}_1 + n_2 \vec{v}_2, \quad (2.17)$$

and  $\eta$  is the amplitude of the given reciprocal lattice vector. The reciprocal lattice vectors for a triangular system can be written as:

## 2 Theoretical background

---

$$\begin{aligned}\vec{v}_1 &= \frac{2\pi}{a} \left( \hat{x} + \frac{1}{\sqrt{3}} \hat{y} \right) \\ \vec{v}_2 &= \frac{2\pi}{a} \left( \frac{2}{\sqrt{3}} \hat{y} \right),\end{aligned}\tag{2.18}$$

where  $a$  is the lattice constant. A one-mode approximation, i.e. an expansion to the lowest order harmonics, corresponds to the technique of retaining only those reciprocal vectors which have a length of  $2\pi/(a\sqrt{3}/2)$ . These vectors correspond to the  $(v_1, v_2)$  pair,  $(1,0)$ ,  $(0,1)$  and  $(1,-1)$ . Keeping only the lowest order set reduces the one-mode approximation to the following expression

$$n = n_0 + A \left[ \frac{1}{2} \cos \left( \frac{2qy}{\sqrt{3}} \right) - \cos(qx) \cos \left( \frac{qy}{\sqrt{3}} \right) \right],\tag{2.19}$$

where  $q = 2\pi/(a\sqrt{3}/2)$ . Substituting the one-mode approximation expression into the free energy functional and then minimizing with respect to  $q_{eq}$  and the amplitude  $A$  gives

$$\begin{aligned}q_{eq} &= \frac{\sqrt{3}}{2} \\ A_{tri} &= \frac{4}{15v} \left( t - 3vn_0 + \sqrt{t^2 - 15va(B_t - B_s) + 12n_0v(2t - 3vn_0)} \right),\end{aligned}\tag{2.20}$$

and  $A_{liq} = 0$  for the liquid phase. The free energy of the solid and liquid phase can be calculated by using the above minimization procedure and then the coexistence region can be calculated by using the common tangent formulation. The corresponding phase diagram as well as the detailed mathematical derivation can be found in [29].

### 2.1.4 Elastic constants

As discussed above, one of the main features of the PFC method is the natural incorporation of the elastic energy into its free energy functional. More precisely, the elastic properties of the system can be evaluated by considering the deformations away from the equilibrium states. Following the procedure described by Elder et al. [7], the elastic constants can be determined by deforming the lattice under shear, bulk or deviatoric deformations and then calculating the corresponding change in energy, i.e. the cost of energy for the deformation. For the originally introduced two-dimensional PFC model [26], the expressions for the bulk, shear and deviatoric deformations can be obtained by considering:

$$\begin{aligned}
 (x, y) &\rightarrow (x/[1 + \sigma], y/[1 + \sigma]) \\
 (x, y) &\rightarrow (x + \sigma y, y) \\
 (x, y) &\rightarrow (x[1 + \sigma], y[1 - \sigma]), \tag{2.21}
 \end{aligned}$$

respectively, where  $\sigma$  is the dimensionless deformation. Eq. (2.21) can be substituted into the one-mode approximation expression Eq. (2.19) for the triangular lattice system in order to obtain modified expressions for these deformations. The resulting expressions for the bulk, shear and deviatoric deformations case are

$$\begin{aligned}
 n_b &= n_0 + A \left[ \frac{1}{2} \cos \left( \frac{2qy}{\sqrt{3}[1 + \sigma]} \right) - \cos \left( \frac{qx}{1 + \sigma} \right) \cos \left( \frac{qy}{\sqrt{3}[1 + \sigma]} \right) \right], \\
 n_s &= n_0 + A \left[ \frac{1}{2} \cos \left( \frac{2qy}{\sqrt{3}} \right) - \cos(q[x + \sigma y]) \cos \left( \frac{qy}{\sqrt{3}} \right) \right], \\
 n_d &= n_0 + A \left[ \frac{1}{2} \cos \left( \frac{2qy[1 - \sigma]}{\sqrt{3}} \right) - \cos(qx[1 + \sigma]) \cos \left( \frac{qy[1 - \sigma]}{\sqrt{3}} \right) \right], \tag{2.22}
 \end{aligned}$$

## 2 Theoretical background

---

respectively. By substituting Eq. (2.22) into the free energy functional expression and solving with respect to the amplitude  $A$  and then further expanding around  $\sigma = 0$  leads to the final expression for the free energy corresponding to the bulk, shear and deviatoric deformations [7], i.e.

$$\begin{aligned}
 F_{bulk} &= F_0 + \frac{4}{3}(q_{eq}^2 A_{eq})^2 \sigma^2 + f(\sigma^3) + \dots \\
 F_{shear} &= F_0 + \frac{1}{6}(q_{eq}^2 A_{eq})^2 \sigma^2 + f(\sigma^3) + \dots \\
 F_{deviatoric} &= F_0 + \frac{2}{3}(q_{eq}^2 A_{eq})^2 \sigma^2 + f(\sigma^3) + \dots
 \end{aligned} \tag{2.23}$$

$q_{eq}$  and  $A_{eq}$  are defined by Eq. (2.20). These energy expressions can be compared with the standard equations to establish a connection with the elastic constants by following the approach used in [7, 29]. This comparison results into the following expressions for the elastic constants of an isotropic system:

$$\frac{C_{11}}{3} = C_{12} = C_{44} = \frac{q_{eq}^4 A_{eq}^2}{3}. \tag{2.24}$$

For these coefficients the resulting Poisson's ratio is  $\nu = 1/3$ . This derivation demonstrates that the parameters of the PFC model can be adjusted to match the given experimental system in order to establish the connection with the real material systems. However, it is important to mention that the Poisson's ratio calculated for the originally introduced PFC model is always  $1/3$  which limits its applicability to a certain class of material systems. An essential focus of this thesis is the further extension of this approach to model systems with arbitrary Poisson's ratio as discussed from sect. 2.4 onwards.

## 2.2 Amplitude expansion of the PFC model and its connection with the PF models

The PFC method was introduced to create a bridge between the atomistic approaches and the traditional PF models which operates on length scale considerably larger than that of the PFC method. Although the PFC method is considered as a computationally more efficient tool compared to other atomistic approaches, the atomic length-scale fluctuations of the atomic density field still restrict its applicability to capture experimentally observable length scales since it demands high computational resources. Thus, the need of high computational resources certainly would make it difficult to model larger-scale microstructure problems in materials science.

Several efforts have been made to address issues concerning the computational efficiency of the PFC method by successfully bridging the atomistic and continuum scales [39, 40, 41, 42, 43]. The main techniques that have been widely used in this context are the so called quick and dirty renormalization group [44, 45, 46] and the multiple scale analysis [41]. An important technique based on the multiple scale analysis approach was proposed by Goldenfeld et al. [44, 45, 46], commonly known as the amplitude expansion technique for the PFC method, where the amplitudes are coupled to the average atomic density fields. The motivation behind this technique can be demonstrated by considering a simple example of a liquid-solid interface in which the interface can be described by only tracking the amplitude, i.e. by smoothly varying the amplitude from a finite value in the crystalline phase to zero value in the liquid phase. Fig. 2.3 illustrates the basic idea of the amplitude expansion technique.

The amplitude expansion formulation has been successfully developed for the standard PFC model of triangular crystal symmetry [39] and for the binary PFC model with triangular, bcc, and fcc crystal symmetries [41]. Athreya et al. developed a further extension to the amplitude expansion technique by introducing a hybrid algorithm that solves the amplitude equation using a polar representation of the amplitude [46]. This methodology demonstrated that the amplitude can vary on

## 2 Theoretical background

---

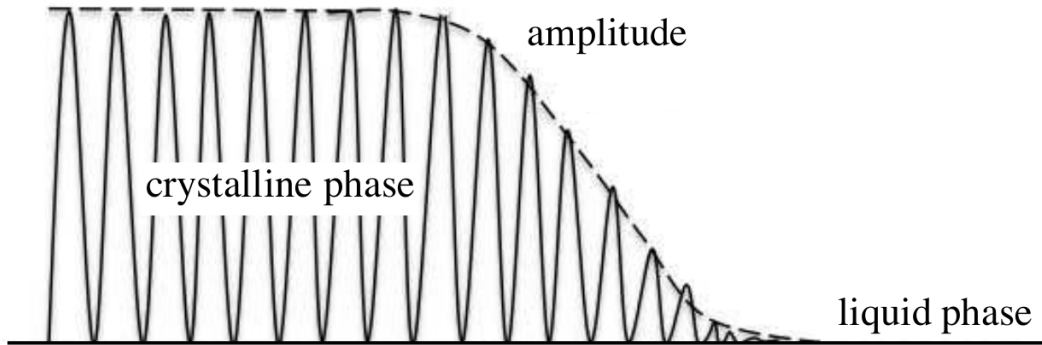


**Figure 2.3:** Smooth variation of the amplitude of the density field from a finite value in the crystalline phase to zero in the liquid phase.

the same scale as the atomic density field at any crystal orientation. This newly introduced hybrid approach increased the computational efficiency by three orders of magnitude compared to the simulations performed for the growth of solid precipitates using a uniform grid in two dimensions [46].

Apart from increasing the computational efficiency, these coarse-graining approaches have recently been further exploited to derive an evolution equation for these amplitudes in order to establish a connection between parameters of the PFC model and the traditional PF models. This connection relates the parameters of the PFC model with the traditional PF models and thus provides more physical justification to the phenomenological phase-field order parameter. More specifically, the complex amplitudes in a small deformation limit can be related to the order parameter of traditional PF models. This complex amplitude has a value of zero in the liquid phase and a finite value in the solid phase. Similar to the order parameter of the PF model, the amplitude varies near dislocations and liquid/solid surfaces. These amplitude formulations can retain many salient atomistic level features while operating on larger scale than that of the original PFC model, which is currently outside the focus of the standard PF approach [40].

Recently these amplitude expansion approaches have been widely used to describe various important phenomena such as solidification of multiple crystallites using an adaptive mesh [46], segregation and alloy solidification [40], liquid-solid interface

[38] and pattern formation phenomena [47, 48, 49].

The capability of the amplitude formulations, given the length scales and time scales on which it operates, allows a way to develop a better understanding of how and where the microscopic parameters enter mesoscale theories. Thus it opens a possibility to study applications which involve experimentally relevant microstructural phenomena on a desired length scale. Following a similar concept, a detailed derivation of the amplitude representation of a newly developed PFC model [10] is discussed in sect. 3.5.

## 2.3 Limitations of the originally introduced PFC model

The PFC approach has been widely applied to model crystallization and a variety of other important materials science phenomena taking place at atomic length scales and diffusive time scales. Some of the important applications reported in the scientific literature include the elastic and plastic deformation of materials [27, 50], crystal growth phenomena [51, 52], fluid crystal interfaces [53, 54], melting [55], the structure [26, 55] and dynamics of grain boundaries [52, 56], crack propagation problems [26] and the glass formation processes [57].

Although the PFC model has successfully been used to study several of these important phenomena, there are certain limitations which restrict its applicability to a specific class of material systems with fixed Poisson's ratio. In PFC method, the elastic behavior of material systems is modeled through the adjustment of its model parameters to match the elastic moduli of a given experimental system, as discussed in previous sections. The detailed derivation of the elastic constants based on the originally introduced PFC model (discussed in sect. 2.1.4) revealed that the Poisson's ratio calculated for this model is always  $1/3$ . Thus the applicability of the originally introduced PFC model [7] is restricted to systems with the Poisson's ratio of  $1/3$ , which excludes several important material systems with higher industrial relevance such as steel and iron with Poisson ratios in a range of  $0.21 - 0.3$  and

which also exist as anisotropic or sheared lattice systems.

Moreover, since in the originally introduced PFC model the physical properties of the material systems are defined by only three parameters, it also restricted the model to describe only certain crystal lattice structures, which include a triangular symmetries in two dimensions and bcc symmetry in three dimensions [38]. Later developments indicated that there are regions of stability for fcc and hcp structures [59] and other crystal symmetries <sup>1</sup>. Thus, in order to extend the applicability of the PFC approach to a wider class of material systems, there was a demand for a more generalized PFC model capable of addressing such shortcomings.

### 2.4 Further development of the PFC method

Based on the brief review of limitations of the originally introduced PFC model discussed in the previous section, one aim of this thesis was the further extension of the applicability of the model to allow a quantitative study of thermodynamic properties of material systems with arbitrary Poisson's ratio as well as to model the anisotropic crystal structures other than the ones captured by the originally introduced PFC model. To do so, here the PFC approach is extended further by developing a generalized PFC model with a capability of modeling both isotropic and anisotropic crystal lattice systems of arbitrary Poisson's ratio as well as condensed matter systems built-up from non-spherical units such as anisotropic systems with oriented particles [8, 60]. This recently introduced model, known as anisotropic phase-field crystal model (APFC), is an extension of the PFC model proposed by Elder et al. [7] to a conservative, anisotropic Langevin equation. The APFC model is fully calibrated from the dynamical density functional theory (DDFT), i.e. its model parameters are derived from the DDFT, which provides the physical justification for the model [8]. This derivation highlights how the APFC model includes the dynamics of the anisotropic particles obtained from the DDFT. Thus the newly

---

<sup>1</sup>Other crystal symmetries implying to protein crystals in a membrane could principally be obtained by including higher order correlation functions, as suggested by P. F. Tupper et al. [58].

developed APFC model has the ability to model both isotropic as well as anisotropic crystal lattice systems with arbitrary Poisson's ratio, which consequently extends the applicability of the PFC approach to a wider class of material systems. The detailed derivation as well as the evaluation of its model parameters is discussed in chapter 3. Moreover, in order to address issues concerning the computational efficiency, the amplitude expansion formulation for the APFC model and the explicit connection of its model parameters with the traditional PF models is also presented and discussed in chapter 3. Furthermore, the application of the PFC model to study the fundamental concepts associated with the nucleation mechanisms in binary systems are discussed in chapter 4 as a step further in the direction of industrially relevant material systems. The main focus of this study is to assess a detailed picture of the nucleation mechanisms beyond the predictions based on the CNT.



### 3 Modeling of anisotropic materials with arbitrary Poisson's ratio\*

The previous chapter provided the basic overview of the PFC theory and highlighted important applications and limitations of the originally introduced PFC model. Although, the PFC method has been applied to a wide range of problems in material science from atomic-to-microscale, however, in the form originally introduced in [7], the model is only capable of modeling materials with Poisson's ratio of  $1/3$ , as discussed in chapter 2. Apart from this limitation, the use of the PFC method is also numerically limited by the resolution of small atomistic length scales and the large simulation time steps required in case of slow system relaxation. To address these limitations, two further development directions were demanded: (a) an extension of the PFC model to a more generalized model with a capability to model material systems of arbitrary Poisson's ratio; and (b) an amplitude expansion formulation to address the computational efficiency issues. The aim of this chapter is to develop a more generalized theoretical model within the framework of the PFC method with the capability of modeling material systems with arbitrary Poisson's ratio as well as to further derive the amplitude formulation for this model in order to address the numerical efficiency issues and thus to extend the applicability of the PFC approach to a wider range of material systems.

This chapter presents a detailed derivation of the newly developed APFC model which has the capability of simulating isotropic as well as anisotropic material systems with arbitrary Poisson's ratio. This chapter is organized as follows. Firstly, a detailed derivation of the APFC model is presented in sect. 3.1, which includes the evaluation of its model parameters as well as the derivation of elastic constants

---

\*Parts of this chapter are already published in [8, 9, 10].

in terms of its model parameters. Then, in sect. 3.2, the DDFT based calibration of the APFC model is presented, which provides the physical justification for the model. In sect. 3.3, some unique features of the APFC are explored by showing some typical simulation results along with a precise phase diagram for the APFC model. Then, to address questions concerning its computational efficiency, an amplitude formulation for the APFC model is derived and explored further by means of a quantitative analysis of the corresponding simulation results in sect. 3.5. This amplitude formulation of the APFC model explicitly demonstrates the connection between the APFC model and the standard PF models and thus enhances the computational efficiency by building a bridge upon the multiple-scale approach. Finally, the important concluding remarks are summarized in sect. 3.6.

## 3.1 Investigation of the APFC model

In this section, the APFC model is introduced and the evaluation of its model parameters is explicitly discussed. The analytical expressions of the elastic constants in terms of the model parameters are also presented, which emphasises the applicability of the APFC model to simulate isotropic as well as anisotropic crystal lattice systems of arbitrary Poisson's ratio.

### 3.1.1 The APFC model

The original PFC model derived by Elder et al. [7] is based on the following equation of motion:

$$\frac{\partial \phi}{\partial t} = M \nabla^2 \left( \frac{\delta F}{\delta \phi} \right), \quad (3.1)$$

where  $M$  is the mobility. The functional (in dimensionless form)

$$F = \int_V \left( \frac{\phi}{2} \left[ r + (1 + \nabla^2)^2 \right] \phi + \frac{\phi^4}{4} \right) dr \quad (3.2)$$

can be extended to an anisotropic PFC model by replacing the laplacian with more general differential operators which allow spatial anisotropy. Doing so, the following free energy functional can be obtained for the APFC model

$$F = \int_V \left( \frac{\phi}{2} \left[ r + 1 + a_{ij} \frac{\partial^2}{\partial x_i \partial x_j} + b_{ijkl} \frac{\partial^4}{\partial x_i \partial x_j \partial x_k \partial x_l} \right] \phi + \frac{\phi^4}{4} \right) dr, \quad (3.3)$$

where  $\phi$  is the phase field,  $r$  represents the undercooling,  $a_{ij}$  is a symmetric matrix and  $b_{ijkl}$  is a fourth rank tensor with the symmetry of an elastic tensor:  $i \leftrightarrow j, k \leftrightarrow l, (i, j) \leftrightarrow (k, l)$ .

From the free energy functional of the APFC model, the corresponding Langevin differential equation of motion for anisotropic lattice system can be written as

$$\rho \frac{\partial \phi}{\partial t} = M \nabla^2 \left( \left[ r + 1 + a_{ij} \frac{\partial^2}{\partial x_i \partial x_j} + b_{ijkl} \frac{\partial^4}{\partial x_i \partial x_j \partial x_k \partial x_l} \right] \phi + c \phi^3 \right). \quad (3.4)$$

The APFC model can be reduced to the original isotropic PFC model [7] by setting the anisotropic parameters  $a_{11} = a_{22} = 2$  and  $b_{1111} = b_{1122} = b_{2222} = 1$ .

An anisotropic triangular stationary state solution to the APFC model can be constructed for a triangular state

$$\phi = \phi_0 + \phi_1 (\cos(k_1 x) \cos(k_2 y / \sqrt{3}) - 1/2 \cos(2k_2 y / \sqrt{3})), \quad (3.5)$$

where  $\phi_0$  and  $\phi_1$  are the amplitude of the phase-field and  $k_1$  and  $k_2$  represent the wave numbers. The free energy expression can be obtained by substituting Eq. (3.5) in Eq. (3.3), i.e.

$$\begin{aligned}
 F = & (3/16)\phi_1^2 r - (3/16)\phi_0\phi_1^3 + (1/2)\phi_0^2 + (1/4)\phi_0^4 \\
 & + (1/2)r\phi_0^2 + (9/16)\phi_0^2\phi_1^2 \\
 & + (1/12)\phi_1^2 b_{1212} k_1^2 k_2^2 - (1/4)\phi_1^2 a_{22} k_2^2 + (1/8)\phi_1^2 b_{1111} k_2^4 \\
 & + (1/8)\phi_1^2 b_{2222} k_1^4 - (1/4)\phi_1^2 a_{11} k_1^2 + (45/512)\phi_1^4 + (3/16)\phi_1^2. \quad (3.6)
 \end{aligned}$$

Minimizing the above free energy expression with respect to the wave numbers, i.e.  $k_1$  and  $k_2$  yields

$$\begin{aligned}
 k_1^2 &= \frac{3(3a_{11}b_{1111} - a_{22}b_{1122})}{(9b_{1111}b_{2222} - b_{1122}^2)} \\
 k_2^2 &= \frac{3(3a_{22}b_{2222} - a_{11}b_{1122})}{(9b_{1111}b_{2222} - b_{1122}^2)}. \quad (3.7)
 \end{aligned}$$

The derivative of the free energy with respect to the amplitude  $\phi_1$  is

$$\begin{aligned}
 F_{\phi_1} = & (45/128)\phi_1^3 + (1/6)\phi_1 b_{1122} k_1^2 + \\
 & (1/4)\phi_1 b_{2222} k_1^2 - (1/2)\phi_1 a_{11} k_1 + (1/4)\phi_1 b_{1111} k_2^2 - \\
 & (1/2)\phi_1 a_{22} k_2 + (9/8)\phi_0^2 \phi_1 - (9/16)\phi_0 \phi_1^2 + (3/8)\phi_1 r + (3/8)\phi_1. \quad (3.8)
 \end{aligned}$$

The solution for stationary state can be obtained by setting this derivative to zero. The resulting expression for the amplitude  $\phi_1$  is

$$\phi_1 = \frac{4}{5} \left( \phi_0 + \frac{1}{3} \sqrt{-15(r + R_1) - 36\phi_0^2} \right), \quad (3.9)$$

where

$$R_1 = 1 - \frac{2(3(a_{11}^2 b_{1111} + a_{22}^2 b_{2222}) - 2b_{1122} a_{11} a_{22})}{(9b_{1111} b_{2222} - b_{1122}^2)}. \quad (3.10)$$

For the case of equal wave numbers, i.e.  $k_1 = k_2 = q_t$ , the resulting expression for  $q_t$  is

$$q_t^2 = \frac{3(a_{11} + a_{22})}{2b_{1122} + 3(b_{1111} + b_{2222})}, \quad (3.11)$$

which reduce to  $q_t = \sqrt{3}/2$  for the isotropic case, i.e. by setting  $a_{11} = a_{22} = 2$  and  $b_{1111} = b_{1122} = b_{2222} = 1$ . Finally, the derivative of the free energy with respect to the amplitude  $\phi_1$  using  $q_t$  from Eq. (3.11) transforms to

$$\begin{aligned} F_{\phi_1}(q_t) = & (3/32)\phi_1 b_{1122} + (3/8)\phi_1 r \\ & + (9/64)\phi_1 b_{2222} - (3/8)\phi_1 a_{11} + (9/8)\phi_0^2 \phi_1 \\ & + (3/8)\phi_1 + (45/128)\phi_1^3 - (3/8)\phi_1 a_{22} \\ & + (9/64)\phi_1 b_{1111} - (9/16)\phi_0 \phi_1^2. \end{aligned} \quad (3.12)$$

A solution for stationary state similar to Eq. (3.9) can be obtained by setting the derivative of the free energy expressed in Eq. (3.12) to zero, where

$$R_1(q_t) = 1 + (1/4)b_{1122} + (3/8)(b_{1111} + b_{2222}) - (a_{11} + a_{22}). \quad (3.13)$$

Unlike the originally introduced PFC model [7], Eq. (3.3) of the APFC model can

model the whole range of Poisson ratios (even different from  $1/3$ ). The relevance of this point for material science is high, since several materials usually have Poisson ratios in the range of  $[0 - 0.5]$  such as steel and iron have Poisson ratios in the range of  $[0.21 - 0.3]$ . Even negative Poisson ratios are known for material systems called anti-rubber, dilational materials [61, 62] or auxetics [63], as reviewed in [64]. More recently, so called gum metals [65] displaying ideal strength in bulk form are discussed intensively for their not yet understood interesting mechanical behavior, which also comes along with Poisson's ratio different from  $1/3$ . To contribute to a more detailed mechanistic understanding of such material systems based on the APFC model, a detailed analysis of the derivation of its Poisson's ratio range is presented in the following section.

#### 3.1.2 Elastic properties

In order to further elaborate the applicability of the APFC model to material systems of arbitrary Poisson's ratio, the elastic properties are evaluated in terms of its model parameters by using the procedure described by Elder et al [7]. The modified forms of Eq. (3.5) for bulk, shear and deviatoric deformations are

$$\begin{aligned}\phi_b &= \phi(x/(1 + \sigma), y/(1 + \sigma)) \\ \phi_s &= \phi(x + \sigma y, y) \\ \phi_d &= \phi(x(1 + \sigma), y(1 - \sigma)),\end{aligned}\tag{3.14}$$

respectively, where  $\sigma$  is the dimensionless deformation. The free energies for these three deformations can be calculated from Eq. (3.3) by using the stationary state parameters  $k_1$  and  $k_2$  from Eq. (3.7). To obtain the elastic constants, the second order derivative of the free energies ( $F_b$ ,  $F_s$ ,  $F_d$ ) are calculated for the three deformations with respect to the dimensionless deformation. The following expressions can be obtained by using the stationary state parameters, i.e.  $k_1$  and  $k_2$ :

$$\begin{aligned}
 \frac{1}{2} \frac{d^2 F_b}{d\sigma^2} &= C_{11} + C_{12} = \frac{1}{12}(\phi_1)^2(15(k_2^4 b_{1111} + k_1^4 b_{2222}) \\
 &\quad - 9(a_{11}k_1^2 + k_2^2 a_{22}) + 10k_2^2 k_1^2 b_{1122}) \\
 \frac{1}{2} \frac{d^2 F_s}{d\sigma^2} &= \frac{C_{44}}{4} = \frac{1}{4}(\phi_1 k_1)^2(b_{1111}k_2^2 - a_{22} + k_1^2 b_{1122}) \\
 \frac{1}{2} \frac{d^2 F_d}{d\sigma^2} &= C_{11} - C_{12} = \frac{1}{12}(\phi_1)^2(15(k_1^4 b_{2222} + k_2^4 b_{1111}) \\
 &\quad - 9(k_2^2 a_{22} + k_1^2 a_{11}) + 2k_2^2 k_1^2 b_{1122}).
 \end{aligned} \tag{3.15}$$

Finally from the above equation, the Poisson's ratio for the two-dimensional case can be defined as function of the model parameters, i.e.

$$\nu = \frac{C_{12}}{C_{11}} = \frac{1}{3} \frac{4k_1^2 k_2^2 b_{1122}}{(5(k_2^4 b_{1111} + k_1^4 b_{2222}) - 3(k_1^2 a_{11} + k_2^2 a_{22}) + 2k_1^2 k_2^2 b_{1122})}, \tag{3.16}$$

where  $k_1$  and  $k_2$  are defined by Eq. (3.7).

The free energies for these three deformations  $F_b$ ,  $F_s$ ,  $F_d$  can also be calculated by Eq. (3.3) using the stationary state parameter  $q_t$  from Eq. (3.11). The corresponding resulting expressions are

$$\begin{aligned}
 \frac{1}{2} \frac{d^2 F_b}{d\sigma^2} &= C_{11} + C_{12} = \frac{1}{2}(q_t \phi_1)^2(a_{11} + a_{22}) \\
 \frac{1}{2} \frac{d^2 F_s}{d\sigma^2} &= \frac{C_{44}}{4} = \frac{1}{4}(q_t \phi_1)^2 \frac{3a_{11}(b_{1122} + b_{1111}) + a_{22}(b_{1122} - 3b_{2222})}{2b_{1122} + 3(b_{1111} + b_{2222})} \\
 \frac{1}{2} \frac{d^2 F_d}{d\sigma^2} &= C_{11} - C_{12} = \frac{1}{6}(q_t \phi_1)^2 q_t (3(b_{1111} + b_{2222}) - 2b_{1122}).
 \end{aligned} \tag{3.17}$$

### 3 Modeling of anisotropic materials with arbitrary Poisson's ratio

---

This yields the Poisson's ratio for the two dimensional case as

$$\nu = \frac{C_{12}}{C_{11}} = \frac{2}{3} \frac{b_{1122}}{(b_{1111} + b_{2222})}. \quad (3.18)$$

It is important to mention that for the isotropic version of PFC model, the above expression transforms to  $\nu = 1/3$ .

In order to further demonstrate the capacity of the APFC model in three dimensions, the model is treated for the bcc lattice system developed in the work [38] for isotropic material system. The crystal density field can be expressed as

$$\phi = \phi_0 + 4\phi_1 [\cos(q_t x) \cos(q_t y) + \cos(q_t x) \cos(q_t z) + \cos(q_t y) \cos(q_t z)]. \quad (3.19)$$

The corresponding free energy expression can be obtained by substituting Eq. (3.19) in Eq. (3.3), i.e.

$$\begin{aligned} F = & (3/4)\phi_1^3\phi_0 + (3/8)\phi_1^2r + (9/8)\phi_0^2\phi_1^2 \\ & + (3/8)\phi_1^2 + (1/2)r\phi_0^2 + (1/2)\phi_0^2 + (1/4)\phi_0^4 \\ & - (3/2)\phi_1^2a_{11}q_t^2 + (3/4)\phi_1^2b_{1111}q_t^4 \\ & + (3/4)\phi_1^2b_{1122}q_t^4 + (135/256)\phi_1^4. \end{aligned} \quad (3.20)$$

Minimizing the above free energy expression with respect to  $\phi_1$  and  $q_t$  yields

$$q_t^2 = \frac{a_{11}}{b_{1111} + b_{1122}}, \quad (3.21)$$

$$\phi_1 = -\frac{2}{15}\phi_0 - \frac{1}{15}\sqrt{-5(r + R_2) - 11\phi_0^2}, \quad (3.22)$$

where

$$R_2 = 1 + (1/2)(b_{1111} + b_{1122}) - 2a_{11}. \quad (3.23)$$

For the isotropic case, the parameters transform to  $q_t^2 = 1/2$ ,  $R_2 = 0$ .

Finally, the resulting elastic relations for the three deformation variants in three dimensions can be calculated by using the procedure mentioned above for the two-dimensional case, i.e.

$$\begin{aligned} \frac{1}{2} \frac{d^2 F_b}{d\sigma^2} &= \frac{3}{2}C_{11} + 3C_{12} = 24(\phi_1)^2 a_{11} \\ \frac{1}{2} \frac{d^2 F_s}{d\sigma^2} &= C_{44}/4 = (\phi_1)^2 (3(b_{1122} + b_{1111}) - 4a_{11}) \\ \frac{1}{2} \frac{d^2 F_d}{d\sigma^2} &= C_{11} - C_{12} = 16(\phi_1)^2 \frac{a_{11}^2 (2b_{1111} - b_{1122})}{(b_{1111} + b_{2222})^2}. \end{aligned} \quad (3.24)$$

The resulting expression for the Poisson's ratio in terms of the model parameters for the three-dimensional case can be written as

$$\nu = \frac{C_{12}}{C_{11} + C_{12}} = \frac{1 - Q}{2 + Q} \quad (3.25)$$

where

$$Q = \frac{2b_{1111} - b_{1122}}{(b_{1111} + b_{1122})^2}. \quad (3.26)$$

It can be seen that the Poisson's ratio becomes negative at  $b_{1122} < (1/2)b_{1111}$ . The

resulting expressions for the Poisson's ratio reveal that, depending on the parameters of the APFC model, the whole range of Poisson ratios can be obtained and thus, a wide class of material systems can be modeled by the APFC model.

This section provided a detailed introduction of the APFC model. Just as the original PFC model was legitimated via recovery of important material parameters, particularly elastic one, it is demonstrated here how the elastic parameters for the APFC model can be recovered. A second important legitimation for PFC models is its full calibration via DDFT. This is demonstrated, as well, in the following section via original work on the calibration for the APFC model. The DDFT is the time-dependent analogue of the static DFT which provides its dynamic generalization [37, 66, 67, 68]. The DDFT can be regarded as a high level of microscopic description, which has been successfully used as a fully established classical approach to justify and to calibrate coarse-grained models as the PFC model [1, 51]. The PFC method can be understood as a truncated form of the DDFT. In general, there are two different aspects of the PFC modeling, i.e. statics aspect based on a free-energy expression for order parameters and a dynamical aspect that describes the time evolution of the order parameters by a diffusion or continuity equation [51]. The static free energy expression was first derived and justified from DFT by Elder et al. [1] (as discussed in chapter 2), while the corresponding dynamics was derived from the DDFT by van Teeffelen et al. [51]. A similar approach is used to calibrate the APFC model via DDFT in the following section.

## 3.2 DDFT based calibration of the APFC model

In this section, the DDFT based derivation of the parameters of the APFC model is presented which provides physical justification for the model. This DDFT based calibration of the APFC model is developed by Hartmut Löwen in the joint work [8]. This derivation is based on the methodology proposed recently by van Teeffelen et al [51] for radially symmetric interactions, however, in this current derivation it is generalized to anisotropic interactions and leads to the publication [8].

Cartesian coordinates  $\mathbf{r} = (x_1, x_2, \dots, x_d)$  are used in the following derivation with  $d$  as the spatial dimension. The anisotropic colloids are assumed to be completely aligned in space. The hard ellipsoids with fixed orientation are formally equivalent to hard-sphere systems by scaling, however, this equivalence is no longer valid if interactions are soft and involve an explicit energy scale. In general, an anisotropic function,  $u(\mathbf{r})$  is taken as the interaction pair potential between two aligned particles. There are several examples which demonstrate this kind of anisotropic interactions with fixed orientations, such as the oriented hard spherocylinders [69], charged rods [70, 71], anisotropic Gaussian potentials [72], board-like colloidal particles [73], colloidal molecules [74], as well as patchy colloids [75] and proteins [76, 77]. Henceforth the inversion symmetry is assumed as

$$u(-\mathbf{r}) = u(\mathbf{r}). \quad (3.27)$$

Here, the DDFT for anisotropic situations [78] is generalized from the isotropic case. The corresponding dynamical evolution of the time-dependent one-particle density field  $\rho(\mathbf{r}, t)$  is:

$$\dot{\rho}(\mathbf{r}, t) = (k_B T)^{-1} \nabla \cdot \left[ \mathcal{D} \rho(\mathbf{r}, t) \nabla \frac{\delta F[\rho(\mathbf{r}, t)]}{\delta \rho(\mathbf{r}, t)} \right], \quad (3.28)$$

where  $k_B T$  is the thermal energy,  $\nabla = (\partial/\partial x_1, \partial/\partial x_2, \dots, \partial/\partial x_d)$  is the  $d$  dimensional gradient and  $\mathcal{D} = \text{diag}(D_1, D_2, \dots, D_d)$  denotes the diagonalized diffusion tensor with the anisotropic short-time translational diffusivities of the anisotropic particle. In general, for any given (hydrodynamic) shape of the particle, the corresponding explicit expressions for  $D_i$  are available in [79, 80]. Furthermore, in Eq. (3.28),  $F[\rho(\mathbf{r}, t)]$  is the equilibrium density functional which can be split as

$$F[\rho(\mathbf{r})] = F_{\text{id}}[\rho(\mathbf{r})] + F_{\text{ex}}[\rho(\mathbf{r})] + F_{\text{ext}}[\rho(\mathbf{r})], \quad (3.29)$$

where

$$F_{\text{id}}[\rho(\mathbf{r})] = k_B T \int d\mathbf{r} \rho(\mathbf{r}) \{ \ln [\rho(\mathbf{r}) \Lambda^d] - 1 \}, \quad (3.30)$$

with  $\Lambda$  denoting the thermal de Broglie wavelength. The external part involves an external one-body potential  $V(\mathbf{r}, t)$  and is given by

$$F_{\text{ext}}[\rho(\mathbf{r})] = \int d\mathbf{r} \rho(\mathbf{r}) V(\mathbf{r}, t). \quad (3.31)$$

The excess part  $F_{\text{ex}}[\rho(\mathbf{r})]$  embodies the nontrivial correlations between particles and must be further approximated. Therefore, to approximate it further, small deviations of the inhomogeneous density profile around a homogeneous reference density  $\rho$  is assumed. In this limit, the leading approximation for  $F_{\text{ex}}[\rho(\mathbf{r})]$  is given by the Ramakrishnan and Yussouff [35] expression:

$$F_{\text{ex}}[\rho(\mathbf{r})] \simeq F_{\text{ex}}(\rho) - \frac{k_B T}{2} \int \int d\mathbf{r} d\mathbf{r}' \Delta\rho(\mathbf{r}) \Delta\rho(\mathbf{r}') c_0^{(2)}(\mathbf{r} - \mathbf{r}'; \rho), \quad (3.32)$$

where  $c_0^{(2)}(\mathbf{r} - \mathbf{r}'; \rho)$  is the anisotropic direct correlation function of the fluid at density  $\rho$  which possesses the same symmetry as the underlying pair potential  $u(\mathbf{r})$ . In particular, it is inversion symmetric, i.e.

$$c_0^{(2)}(-\mathbf{r}, \rho) = c_0^{(2)}(\mathbf{r}, \rho). \quad (3.33)$$

Moreover,  $\Delta\rho(\mathbf{r}) = \rho(\mathbf{r}) - \rho$ . In Fourier space Eq. (3.32) reads

$$\mathcal{F}_{\text{ex}}[\rho(\mathbf{r})] = F_{\text{ex}}(\rho) - \frac{k_B T (2\pi)^d}{2} \int d\mathbf{k} \Delta\tilde{\rho}(\mathbf{k}) \Delta\tilde{\rho}(-\mathbf{k}) \tilde{c}_0^{(2)}(\mathbf{k}, \rho) \quad (3.34)$$

with  $\sim$  denoting a Fourier transform. The direct correlation function  $c_0^{(2)}(\mathbf{k}, \rho)$  can be expanded in terms of  $\mathbf{k}$  around  $\mathbf{k} = 0$  (Alternatively fitting procedures can be used, e.g. around the first peak of  $c_0^{(2)}(\mathbf{k}, \rho)$ ). This leads to the Taylor expansion in Fourier space

$$\tilde{c}_0^{(2)}(\mathbf{k}, \rho) = \hat{C}_0 + \sum_{i,j=1}^d a_{ij} k_i k_j + \sum_{i,j,k,l=1}^d b_{ijkl} k_i k_j k_k k_l + \dots, \quad (3.35)$$

corresponding to a gradient expansion in real-space. Inversion symmetry Eq. (3.33) enforces all odd orders to vanish. Possible additional symmetries in the shape of particles will lead to the corresponding restrictions on the tensorial coefficients  $a_{ij}$  and  $b_{ijkl}$  as discussed below. Inserting this expansion into Eq. (3.28) resulted in the following expression for  $\dot{\rho}(\mathbf{r}, t)$ :

$$\begin{aligned} \dot{\rho}(\mathbf{r}, t) = & \nabla \cdot \mathcal{D} \nabla \rho(\mathbf{r}, t) + \nabla \cdot \mathcal{D} \nabla \left[ (k_B T)^{-1} V(\mathbf{r}, t) \right. \\ & \left. - \left( \hat{C}_0 - \sum_{i,j=1}^d a_{ij} \frac{\partial^2}{\partial x_i \partial x_j} + \sum_{i,j,k,l=1}^d b_{ijkl} \frac{\partial^4}{\partial x_i \partial x_j \partial x_k \partial x_l} \right) \rho(\mathbf{r}, t) \right]. \end{aligned} \quad (3.36)$$

By using the constant mobility approximation, i.e.  $\rho(\mathbf{r}, t) = \rho$  in front of the functional derivatives in Eq. (3.28) and by approximating

$$F_{\text{id}}[\rho(\mathbf{r})] \approx k_B T \rho \int d\mathbf{r} \left\{ \frac{1}{2} \phi(\mathbf{r}, t)^2 - \frac{1}{6} \phi(\mathbf{r}, t)^3 + \frac{1}{12} \phi(\mathbf{r}, t)^4 - \text{const.} \right\} \quad (3.37)$$

with  $\phi(\mathbf{r}, t) = \Delta \rho(\mathbf{r}, t) / \rho$ , the final expression for  $\dot{\phi}(\mathbf{r}, t)$  can be written as

$$\begin{aligned} \dot{\phi}(\mathbf{r}, t) = & \rho \nabla \cdot \mathcal{D} \nabla \left[ \phi(\mathbf{r}, t) - \frac{1}{2} \phi(\mathbf{r}, t)^2 + \frac{1}{3} \phi(\mathbf{r}, t)^3 + (k_B T)^{-1} V(\mathbf{r}, t) \right. \\ & \left. - \rho \left( \hat{C}_0 - \sum_{i,j=1}^d a_{ij} \frac{\partial^2}{\partial x_i \partial x_j} + \sum_{i,j,k,l=1}^d b_{ijkl} \frac{\partial^4}{\partial x_i \partial x_j \partial x_k \partial x_l} \right) \phi(\mathbf{r}, t) \right]. \end{aligned} \quad (3.38)$$

This expression exactly reduces to the APFC model for the special case with  $d = 2$

### 3 Modeling of anisotropic materials with arbitrary Poisson's ratio

---

and a neglected cubic term in the ideal gas functional expansion in Eq. (3.37). As a remark the latter was retained in other variants of the PFC model [1, 53]. With that, the parameters of the APFC model are fully derived and justified from the DDFT, however, this derivation illustrates to be a more realistic approximation for anisotropic diffusivities. Furthermore, if Eq. (3.37) is used, some approximations can be avoided but these were not found to change the results significantly for spherical interactions [51]. A second remark concerns the phenomenological symmetry arguments for the expansion coefficients  $a_{ij}$  and  $b_{ijkl}$  of the APFC model.

The orientation of the fixed particles is assumed to be set by a single unit vector  $\vec{E}$  only. The free energy is invariant under space inversion. This is the case for  $d = 2$  and for rotationally symmetric particles in  $d = 3$ . Then, any gradient term in the scalar free energy functional must involve an even number of gradients due to space inversion symmetry. For the rotational symmetry of space, only combinations of  $\vec{E} \cdot \vec{\nabla}$  and  $\vec{\nabla} \cdot \vec{\nabla}$  are required to be nonvanishing in the functional. Therefore the only possibility for physically relevant gradient terms is

$$\sum_{i,j=1}^d a_{ij} \frac{\partial^2}{\partial x_i \partial x_j} = \lambda_1 (\vec{E} \cdot \vec{\nabla})^2 + \lambda_2 \Delta \quad (3.39)$$

and

$$\sum_{i,j,k,l=1}^d b_{ijkl} \frac{\partial^4}{\partial x_i \partial x_j \partial x_k \partial x_l} = \lambda_3 (\vec{E} \cdot \vec{\nabla})^4 + \lambda_4 (\vec{E} \cdot \vec{\nabla})^2 \Delta + \lambda_5 \Delta^2, \quad (3.40)$$

where  $\lambda_1$ ,  $\lambda_2$ ,  $\lambda_3$ ,  $\lambda_4$ , and  $\lambda_5$  are scalar prefactors. Thus the number of independent degrees of freedom in  $a_{ij}$  and  $b_{ijkl}$  is reduced down to 5. In case, if there are different fixed vectors, i.e.  $\vec{E}$  and  $\vec{B}$ , then there are correspondingly more terms allowing for more freedom in  $a_{ij}$  and  $b_{ijkl}$ . This is realized, e.g. for biaxial colloidal particles in two crossed external fields along  $\vec{E}$  and  $\vec{B}$ .

### 3.3 Investigation of characteristic morphological features

In this section, a phase diagram is established as first step to access the fundamental phase transition features of the APFC model. The stable state phases obtained from numerical simulations are investigated with respect to characteristic morphological features. As initial condition, a square domain is defined with a sphere in the center to initialize the nucleus. Periodic boundary conditions are used on all sides of the square box. Fig. 3.1 demonstrates the initial conditions used in simulations. The results presented in this sections are based on the simulations performed with a specific set of model parameters defined in [8], i.e.  $a_{11} = a_{22} = 2$ ,  $b_{1111} = b_{2222} = b_{1122} = 1$  and  $b_{1212} = 0$ . The constant values are also used for the mobility and the parameter  $c$ , i.e.  $M = 1$  and  $c = 1$  in these simulations. However, a typical set of values is used for the anisotropic parameter  $s$  and the undercooling parameter  $r$  in order to investigate the influence of the anisotropy and undercooling on the overall crystal growth phenomena as well as on the resulting microstructures.

Simple explicit numerical schemes are used to ensure the convergence of results and to obtain a reasonably well approximated solution. A forward Euler scheme is used for the time derivative with a sufficiently small time step of  $\Delta t = 0.00075$  to ensure the stability of the scheme, whereas, the Laplace operators are approximated by using a second order difference scheme given by

$$\nabla^2 \phi = \left( \phi_{i+1,j} + \phi_{i-1,j} + \phi_{i,j+1} + \phi_{i,j-1} - 4\phi_{i,j} \right) / (\Delta x)^2. \quad (3.41)$$

The simulations are performed for 512 times 512 numerical grid units with  $\Delta x$  is chosen as  $\pi/4$ . Convergence of simulation results is ensured via convergence studies.

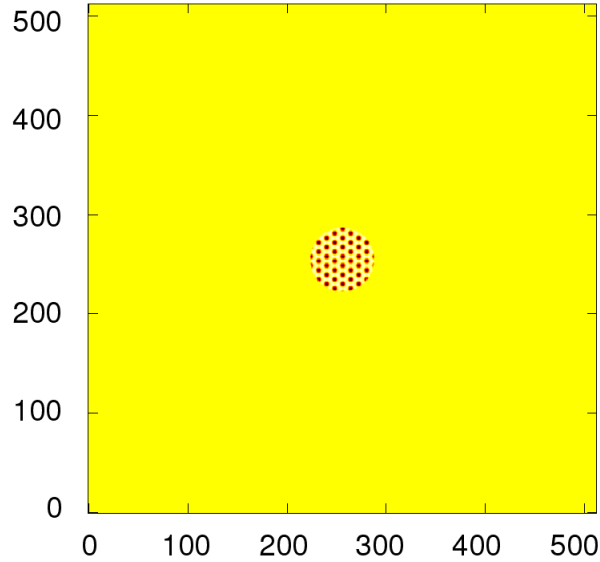


**Figure 3.1:** A square simulation box of size 512 x 512 with a sphere in the center to initialize the nucleus.

#### 3.3.1 Anisotropic effects

The anisotropy of the material at the atomic scale is quantified by a dimensionless parameter  $s$  which can be defined in terms of the model parameters as

$$s = -\frac{b_{1112}}{b_{1111}}. \quad (3.42)$$

The effect of the anisotropic parameter on the resulting microstructures is studied by performing numerical simulations with  $s = 0$  and  $s = 0.3$ . The boundary conditions as well as values used for all other model parameters in these simulations are the same as given in the beginning of sect. 3.3. The results obtained for both cases after 60,000 time steps are demonstrated in Fig. 3.2.

As expected the simulation results obtained for the isotropic case resulted in a sym-

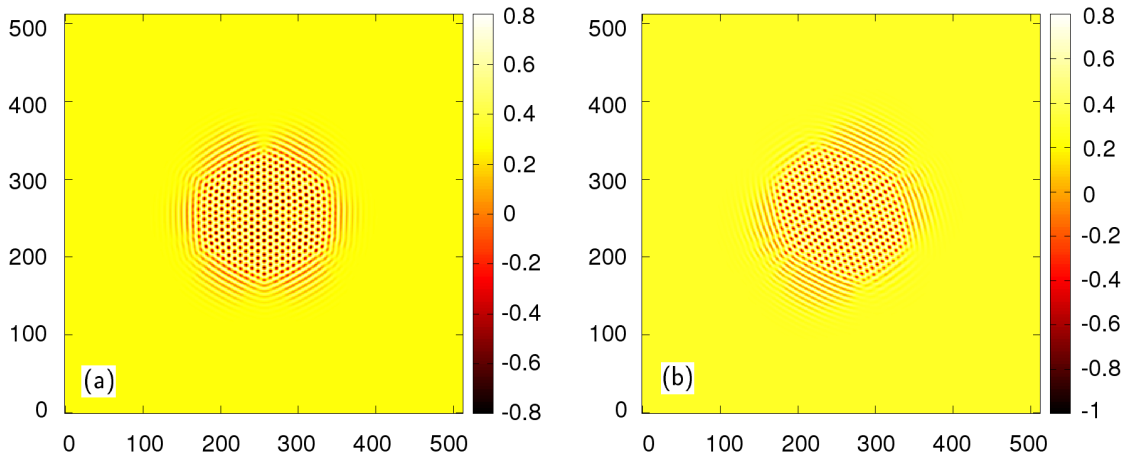


**Figure 3.2:** Simulation results of crystal growth calculated for  $r = -0.4$  and (a)  $s = 0$  (isotropic case) and (b)  $s = 0.3$  (anisotropic case).

metric triangular phase morphology. However, in order to further demonstrate the anisotropic effects, the form of triangles in the resulting microstructures obtained for both isotropic and anisotropic case are analyzed. The form of a triangle is determined in terms of the three internal angles of the triangle. The results show that the triangular phase obtained in case of  $s = 0$ , i.e. without any anisotropy, consists of triangles with all three internal angles of  $60^\circ$  each. However, the triangular phase obtained for the anisotropic case contains triangles with dissimilar sides. This underlines the capability of the APFC model to give rise to truly anisotropic morphologies. In the following, the effect of the anisotropy on the resulting microstructures is analyzed in a more quantitative manner by calculating the internal angles of the triangles for the microstructures obtained from simulations performed with various values of anisotropic parameter. Fig. 3.3 demonstrates the variation of the internal angles as function of the anisotropic parameter.

The anisotropic crystal lattices obtained from the APFC model can be qualitatively compared with the distorted lattices found from experimental investigation of the structures formed in aqueous dispersions of charged colloidal spheres [81] and the phase behavior of highly charged colloidal spheres in a confining wedge geometry [82].

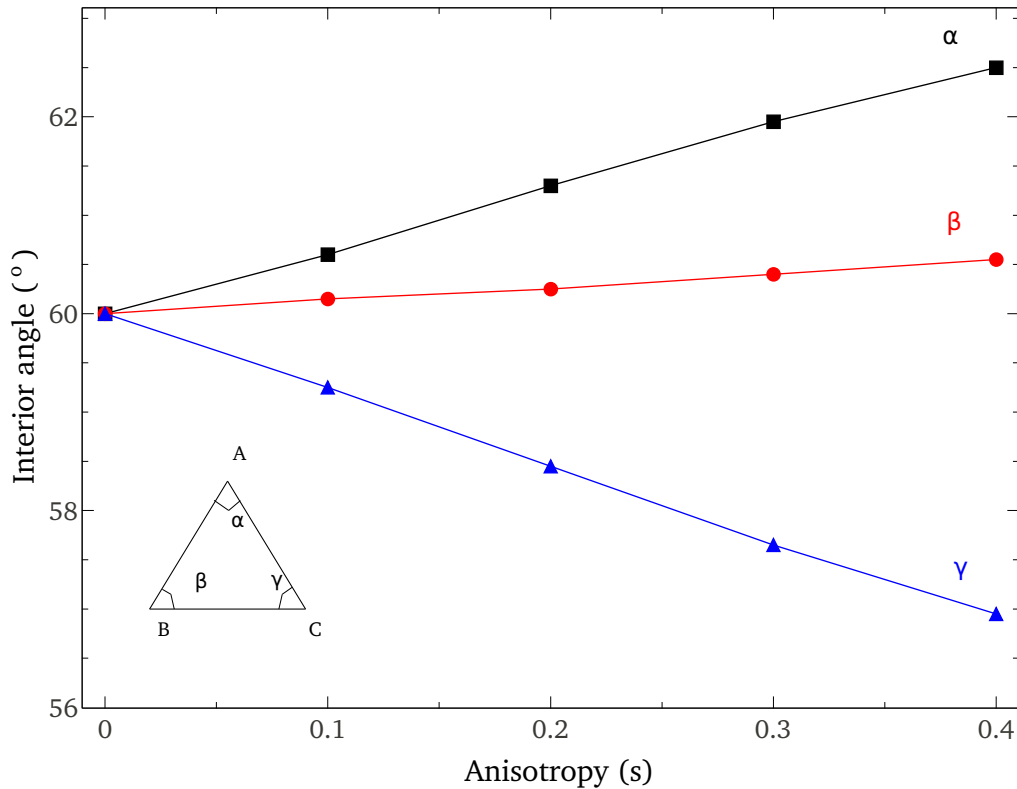


**Figure 3.3:** Form of triangles in the final triangular phase obtained with various values of anisotropic parameter.

### 3.3.2 Undercooling effects

When a liquid is supercooled just below the melting temperature the crystal starts to grow and this growth of the crystal is directly related to the undercooling in the system. Depending on the undercooling, which quantifies the distance from the phase-equilibrium line in the phase diagram, the resulting final states can have different morphologies.

In this section, the rate of crystal growth from a supercooled liquid state is investigated. In the APFC model  $r$  represents the undercooling. Simulations are performed with various values of  $r$  in order to investigate the effect of  $r$  on the resulting microstructures. However, for simplicity, a constant value of anisotropic parameter  $s$  is used in these simulations. The initial condition used in these simulations are the same as described in sect. 3.3). The simulation results showed that the rate

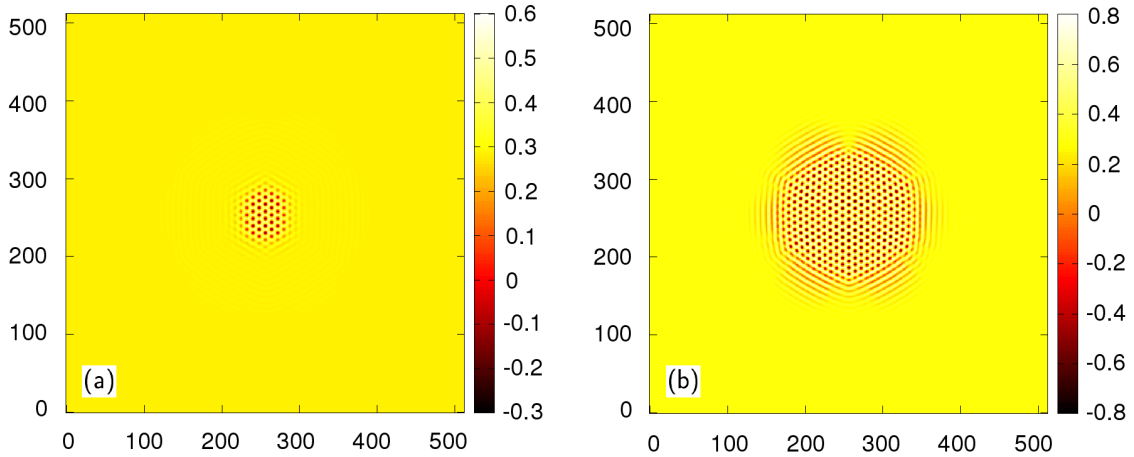


**Figure 3.4:** Simulation results of crystal growth after 60,000 time steps for  $s = 0$  and (a)  $r = -0.2$  and (b)  $r = -0.4$ .

of crystal growth decreases with an increase in the value of  $r$ , which demonstrates that  $r$  truly represents the undercooling in the APFC model. The simulation results obtained with  $s = 0$  (isotropic case) for two typical values of  $r$ , i.e. with  $r = -0.4$  and  $r = -0.2$ , after 60,000 time steps are depicted in Fig. 3.4.

#### 3.3.3 Phase diagram

In this section, the influence of the anisotropy and undercooling on the stable state phase is investigated in detail. More specifically, simulations are performed with various values of  $s$  and  $r$  to obtain the corresponding stable state phases for the phase diagram in  $s$ - $r$  space. Fig. 3.5 demonstrates the resulting phase diagram in  $s$ - $r$  space. Fig. 3.5 illustrates that the stable state phase always consists of stripes if  $s \geq 0.25$  irrespective of the  $r$  value. The co-existence phases is found only in case of  $s = 0.125$  and  $r \leq -0.5$ , while for other values of  $s$  and  $r$ , the stable state consist of a triangular phase.

Typical resulting microstructures for various points of the phase diagram obtained after 1000000 time steps with  $dt = 0.00075$  are illustrated in Fig. 3.6. These morphologies reflect the evolution of a crystal of triangular phase at  $s = 0$  and  $r = -0.25$

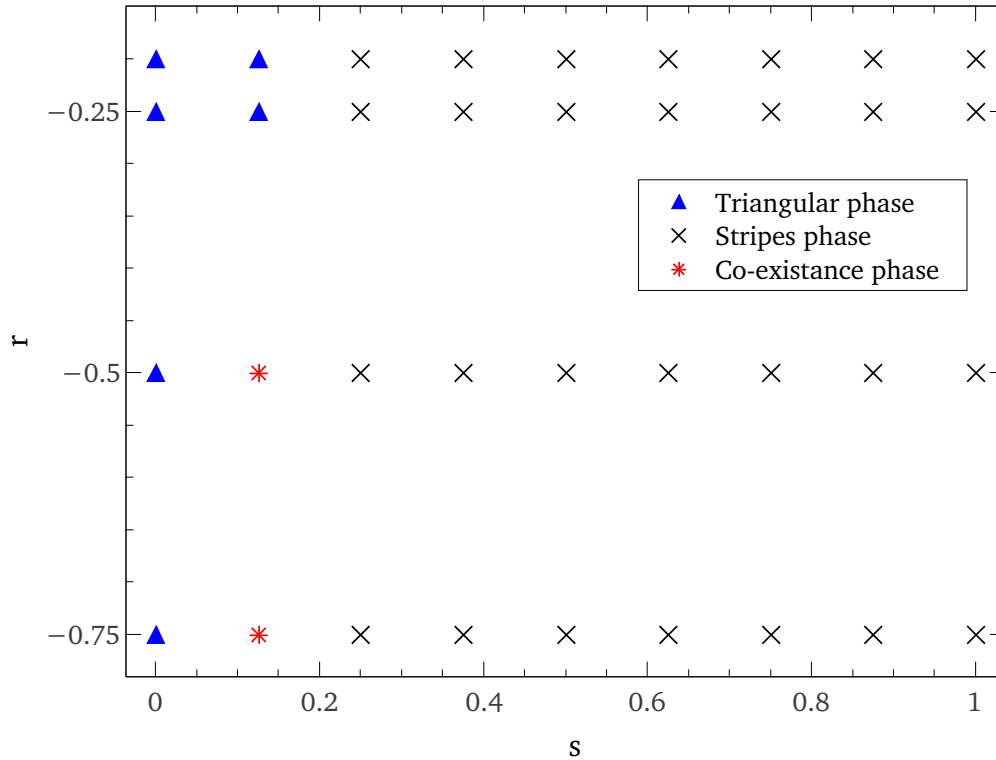
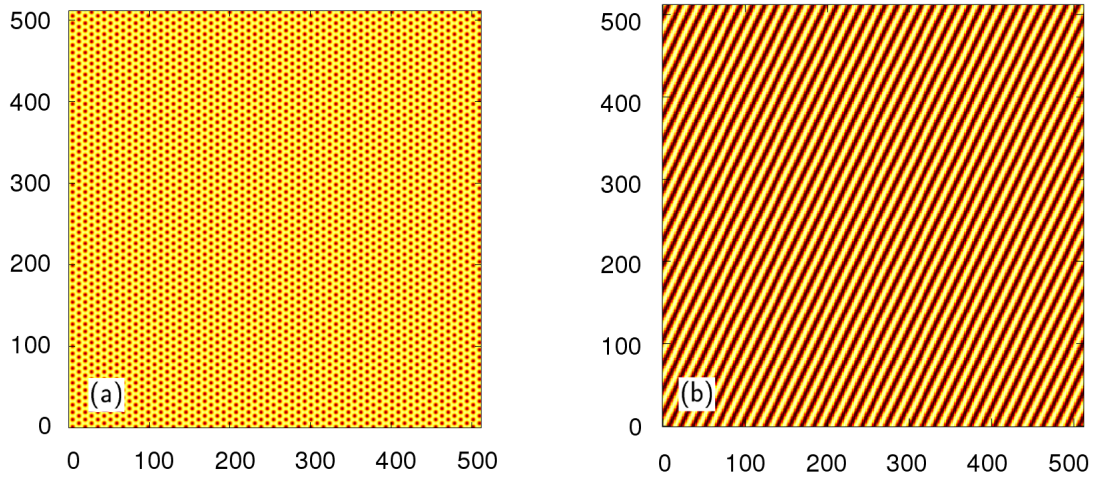


Figure 3.5: The resulting phase diagram for the APFC model in  $s$ - $r$  space.

and the evolution of a crystal of the stripe phase simulated at  $s = 0.5$  and  $r = -0.25$ .

#### 3.3.4 A quantitative study of the impact of anisotropy on the resulting microstructures

In this section, the impact of the anisotropy (expressed as shear deformation, i.e.  $\phi_s = \phi(x, y + sx)$ ) on the resulting microstructures obtained from the APFC model is further investigated in a more quantitative manner. More specifically, numerical simulations are performed with a certain set of parameter values (given in the beginning of sect. 3.3) and varying the anisotropic parameter  $s$ . For simplification, the stripe phases are used as a reference case in order to demonstrate the influence of the anisotropy on the resulting microstructures in the following simulations. The initial



**Figure 3.6:** Typical morphologies obtained from the APFC model (a) the crystal growth simulated at  $s = 0$  and  $r = -0.25$  and (b) the solidification of a crystal of the stripe phase simulated at  $s = 0.5$  and  $r = -0.25$ .

conditions for the following numerical simulations are the same as given in sect. 3.3, however, a relatively smaller simulation box of  $256 \times 256$  is used in these simulation. Typical stable state phase morphologies of stripe phases obtained from simulations performed with various values of the anisotropic parameter  $s$  are depicted in Fig. 3.7.

Fig. 3.7 demonstrates that the distance between the neighboring stripes decreases with an increase of  $s$ . In order to further investigate the dependence of the distance between the neighboring stripes on the anisotropy  $s$  in a more quantitative manner, the dimensionless distance between the neighboring stripes  $d$  (in units of the lattice parameter  $a_0 = 10\Delta x$ ) obtained from simulations is plotted for various values of  $s$  in Fig. 3.8.

The influence of  $s$  on the stripe morphology can be described best by a Boltzmann function, which in general form can be expressed as

$$y = A_2 + \frac{A_1 - A_2}{1 + \exp\left[\frac{x-x_0}{\alpha}\right]} \quad (3.43)$$

### 3 Modeling of anisotropic materials with arbitrary Poisson's ratio

---

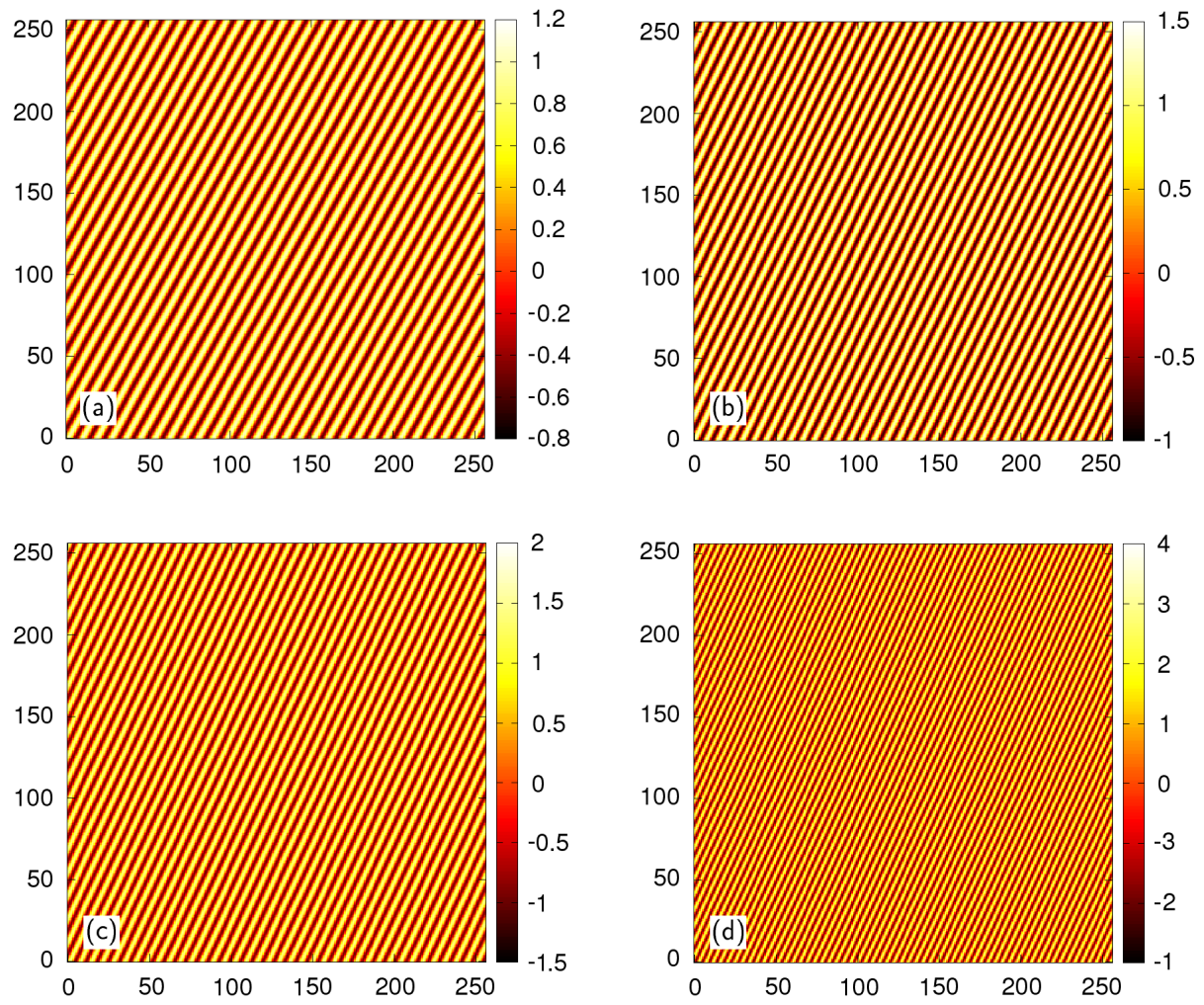


**Figure 3.7:** Typical stable morphologies obtained from simulations performed with (a)  $s = 0.25$ , (b)  $s = 0.5$ , (c)  $s = 0.75$  and (d)  $s = 1$ .

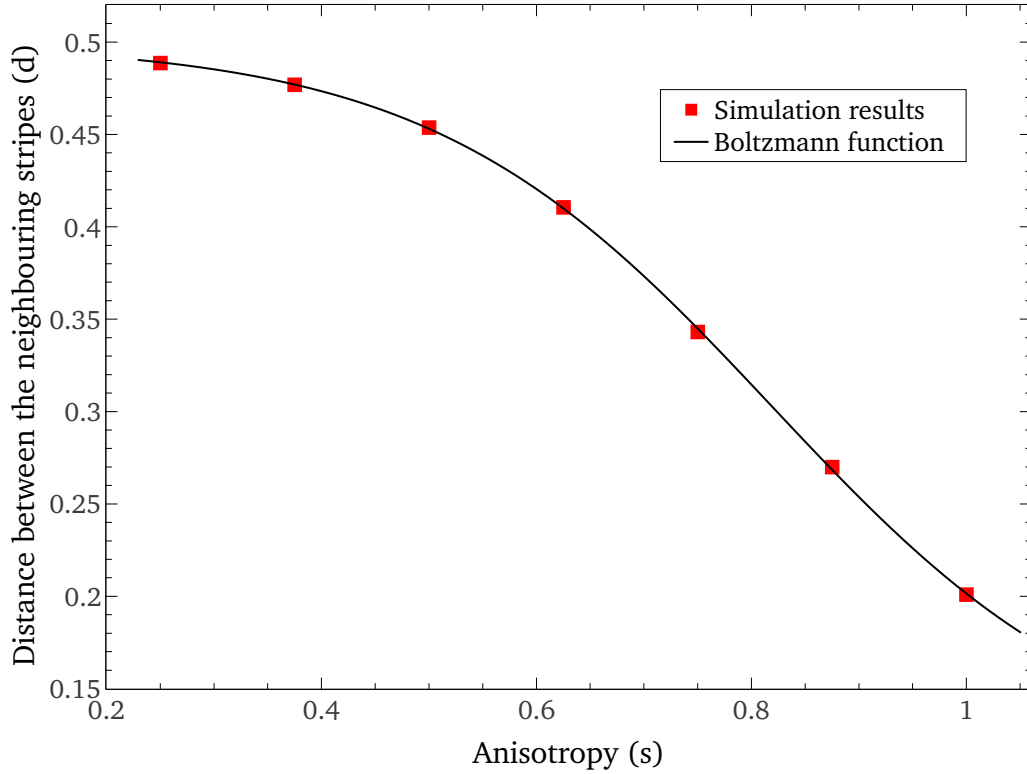


**Figure 3.8:** The distance between the neighboring stripes for various values of anisotropic parameter  $s$ .

with four constant parameters, i.e.  $A_1$ ,  $A_2$ ,  $x_0$  and  $\alpha$ . The values for these parameters are obtained from the curve fitting technique which yields the following function to describe the dependence of  $d$  on  $s$ :

$$d = 0.106 + 0.394 / [1 + \exp(\frac{s - 0.82}{0.16})]. \quad (3.44)$$

### 3.4 Further evaluation of model parameters

In this section, the evaluation of model parameters of the APFC model is explicitly discussed. The anisotropy is considered as a shear of a triangle lattice in the following derivation. This anisotropy of the material at the atomic scale is quantified by a

### 3 Modeling of anisotropic materials with arbitrary Poisson's ratio

---

dimensionless parameter  $s$  which represents the shear of the lattice and the parameters  $a_1$  and  $a_2$  define the tensions in  $x$  and  $y$  directions, respectively. This detailed evaluation provides the definition of all components of the matrix  $a_{ij}$  and the tensor  $b_{ijkl}$  of the free energy functional of the APFC model expressed in Eq. (3.3) in terms of  $s$ ,  $a_1$  and  $a_2$ . In addition to the previous section where the components of the tensor  $b_{ijkl}$  were defined as fixed values, this detailed evaluation considered a more generalized case to further elaborate the model parameters. The main objective of this section is to establish the connection between various model parameters in order to develop a better understanding of the model.

The dimensionless free energy functional of APFC model in Eq. (3.3) can be expressed in the following anisotropic form:

$$F = \int_V \left( \frac{\phi}{2} \left[ r + (1 + \overrightarrow{\nabla}_s^2)^2 \right] \phi + \frac{\phi^4}{4} \right) dr, \quad (3.45)$$

where  $\phi$  is the phase field,  $r$  represents the undercooling and  $\nabla_s$  is the anisotropic gradient term. For an anisotropic triangular crystal lattice, the APFC model uses the following atomic function (one more approximation)

$$\phi = \phi_0 + \phi_1 \left[ \cos(k_1 x) \cos \left( k_2 \frac{(y + sx)}{\sqrt{3}} \right) + \frac{1}{2} \cos \left( 2k_2 \frac{(y + sx)}{\sqrt{3}} \right) \right], \quad (3.46)$$

where  $\phi_0$  and  $\phi_1$  are the average value and the amplitude of the phase field,  $k_1$  and  $k_2$  are the wave numbers and  $s$  is a parameter which quantifies the anisotropy of the material at the atomic scale. As it is clear from Eq. (3.46) the unit vector of the crystal lattice  $\vec{e}_y$  is shifted to the anisotropic vector  $\vec{e}_y^s = \vec{e}_y - s\vec{e}_x$  due to the shear  $s$  in  $x$ -direction. Therefore, the corresponding anisotropic gradient term in Eq. (3.45) is defined in 2D as

$$\overrightarrow{\nabla}_s = a_1 \nabla_x \vec{e}_x + a_2 \nabla_y \vec{e}_y^s. \quad (3.47)$$

where  $a_1$  and  $a_2$  represent the extension of the crystal lattice in  $x$  and  $y$  directions. Here and in the following  $\nabla_i, \nabla_{ij}, \nabla_{ijkl}$  represents the partial derivatives. The above equation can be further expanded to obtain an expression for the gradient square term in 2D, i.e

$$\vec{\nabla}_s^2 = a_1^2 \nabla_{xx} |\vec{e}_x|^2 + 2a_1 a_2 \nabla_{xy} (\vec{e}_x \cdot \vec{e}_y^s) + a_2^2 \nabla_{yy} |\vec{e}_y^s|^2, \quad (3.48)$$

Eq. (3.48) can be rewritten by introducing the vector product calculated as  $(\vec{e}_x \cdot \vec{e}_y^s) = -s \cdot 1 + 1 \cdot 0 = -s$  and the vector norm  $|\vec{e}_y^s| = \sqrt{1 + s^2}$ , i.e

$$\vec{\nabla}_s^2 = a_1^2 \nabla_{xx} - 2a_1 a_2 s \nabla_{xy} + a_2^2 (1 + s^2) \nabla_{yy}. \quad (3.49)$$

Similarly Eq. (3.49) can be further expanded to obtain an expression for  $\vec{\nabla}_s^4$ , i.e

$$\begin{aligned} \vec{\nabla}_s^4 &= (\vec{\nabla}_s^2)^2 = a_1^4 \nabla_{xxxx} - 4a_1^3 a_2 s \nabla_{xxxxy} \\ &+ 2a_1^2 a_2^2 (1 + s^2) \nabla_{xxyy} + 4a_1^2 a_2^2 s^2 \nabla_{xyxy} \\ &- 4a_1 a_2^3 s (1 + s^2) \nabla_{xyyy} + a_2^4 (1 + s^2)^2 \nabla_{yyyy}. \end{aligned} \quad (3.50)$$

For the simplest case (as discussed in [8]), the derivatives used in the free energy functional of the APFC model can be expanded in the following form

$$a_{ij} \frac{\partial^2}{\partial x_i \partial x_j} = a_{11} \frac{\partial^2}{\partial x^2} + 2a_{12} \frac{\partial^2}{\partial x \partial y} + a_{22} \frac{\partial^2}{\partial y^2} \quad (3.51)$$

and

### 3 Modeling of anisotropic materials with arbitrary Poisson's ratio

---

$$\begin{aligned}
 b_{ijkl} \frac{\partial^4}{\partial x_i \partial x_j \partial x_k \partial x_l} &= b_{1111} \frac{\partial^4}{\partial x^4} + 4b_{1112} \frac{\partial^4}{\partial x^3 \partial y} + 2b_{1122} \frac{\partial^4}{\partial x^2 \partial y^2} \\
 &\quad + 4b_{1212} \frac{\partial^4}{\partial x^2 \partial y^2} + 4b_{1222} \frac{\partial^4}{\partial x \partial y^3} + b_{2222} \frac{\partial^4}{\partial y^4}. \quad (3.52)
 \end{aligned}$$

The components of the matrix  $a_{ij}$  and the tensor  $b_{ijkl}$  of the APFC model can be evaluated by comparing the coefficients of Eq. (3.49) and Eq. (3.50) with Eq. (3.3), i.e.

$$\begin{aligned}
 a_{11} &= a_1^2, \\
 a_{22} &= a_2^2(1 + s^2), \\
 a_{12} &= -a_1 a_2 s, \quad (3.53)
 \end{aligned}$$

and

$$\begin{aligned}
 b_{1111} &= a_1^4, \\
 b_{1112} &= -a_1^3 a_2 s, \\
 b_{1122} &= a_1^2 a_2^2 (1 + s^2), \\
 b_{1212} &= a_1^2 a_2^2 s^2, \\
 b_{1222} &= -a_1 a_2^3 s (1 + s^2), \\
 b_{2222} &= a_2^4 (1 + s^2)^2. \quad (3.54)
 \end{aligned}$$

Eq. (3.53) and Eq. (3.54) demonstrate that all the model parameters can be expressed in terms of three independent parameters, namely  $s$ ,  $a_1$  and  $a_2$  with  $s$  defines shear and the parameter  $a_1$  and  $a_2$  define the tensions in  $x$  and  $y$  directions, respectively.

## 3.5 Bridging the PF and PFC approaches for anisotropic systems

The use of the PFC method is often limited to small systems due to the high computational demand since it needs 8 – 10 spatial grid points per atomic spacing as discussed in sect. 2.2. To overcome this computational limitation and to extend the applicability the PFC model, the concept of amplitude expansion (introduced by Goldenfeld et al. [44, 45]) is widely used. In this concept, the amplitudes are coupled to the average atomic density field. Following a similar concept, the amplitude representation of the APFC model is derived for a triangular crystal lattice [11] in this section. Furthermore, the method of multiple-scale analysis (discussed in [39, 40]) is used to further exploit the amplitude expansion technique in order to derive the relationship between the amplitude equation for the APFC model and the standard PF model with elasticity effects, which provides an explicit connection between the PF and PFC modeling approaches.

A comparison of the simulation results for an anisotropic crystal growth obtained from the originally introduced APFC model and the newly derived amplitude representation of APFC model is also presented in order to illustrate the capacity of the amplitude representation to model the similar characteristic features as well as to establish its link to the standard PF model. Thus, the amplitude expansion presented in this section leads to a computationally more efficient model and highlighted its potential as a bridge between the PF and PFC models with anisotropic interface energies and kinetics.

### 3.5.1 Amplitude expansion of the APFC model

In this section the evolution equation of the APFC model is transformed to the evolution equation for the slowly varying amplitudes which describe the triangular crystalline system. The evolution equation for the APFC model given by Eq. (3.4) can also be expressed in the following form:

### 3 Modeling of anisotropic materials with arbitrary Poisson's ratio

---

$$\frac{\partial \phi}{\partial t} = \nabla^2 (\Lambda_s^0 \phi + r\phi + c\phi^3), \quad (3.55)$$

where  $\Lambda_s^0 = (1 + \nabla_s^2)^2$ .

For a periodic structure the atomic density field ( $\phi$ ) can be expressed (in one-mode approximation) with three amplitudes  $\eta_j$  in the complex form as

$$\phi = \phi_0 + \sum_{j=1}^3 \eta_j e^{(i\vec{q}_j \cdot \vec{r})} + \sum \eta_j^* e^{(-i\vec{q}_j \cdot \vec{r})}, \quad (3.56)$$

where  $\vec{q}_j$  are the principle reciprocal lattice vectors and  $\eta_j^*$  is the complex conjugate. The model equations will be developed only for the lowest-order amplitudes which are needed to reconstruct a given crystal symmetry as well as the elastic and plastic effects in solidification.

The free energy of the APFC model given by Eq. (3.45) is minimized by a triangular lattice Eq. (3.46) in two-dimensional case, from which the principle reciprocal lattice vectors can be derived. The cosine parts of Eq. (3.46) can be rewritten as

$$\begin{aligned} & \cos(k_1 x) \cos\left(k_2 \frac{(y+sx)}{\sqrt{3}}\right) + \frac{1}{2} \cos\left(2k_2 \frac{(y+sx)}{\sqrt{3}}\right) = \\ & -\frac{1}{2} \cos\left(q_{eq} \left(-x - \frac{(sx+y)}{\sqrt{3}}\right)\right) + \frac{1}{2} \cos\left(q_{eq} \left(x - \frac{(sx+y)}{\sqrt{3}}\right)\right) + \\ & \frac{1}{2} \cos\left(2q_{eq} \frac{(y+sx)}{\sqrt{3}}\right). \end{aligned} \quad (3.57)$$

The corresponding set of principle reciprocal lattice vectors are given by

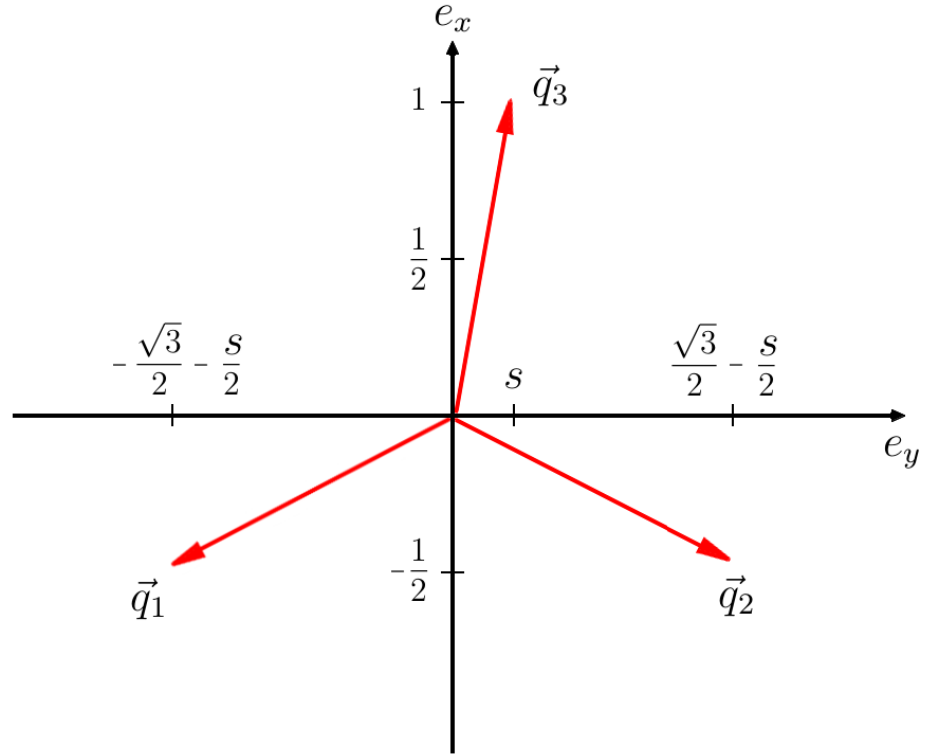


**Figure 3.9:** The principle reciprocal-lattice vectors of the anisotropic triangular lattice.

$$\begin{aligned}
 \vec{q}_1 &= q_{eq} \left( \left( -1 - \frac{1}{\sqrt{3}}s \right) \vec{e}_x - \frac{1}{\sqrt{3}}\vec{e}_y \right) = \left\{ -\frac{\sqrt{3}}{2} - \frac{1}{2}s; -\frac{1}{2} \right\}, \\
 \vec{q}_2 &= q_{eq} \left( \left( 1 - \frac{1}{\sqrt{3}}s \right) \vec{e}_x - \frac{1}{\sqrt{3}}\vec{e}_y \right) = \left\{ \frac{\sqrt{3}}{2} - \frac{1}{2}s; -\frac{1}{2} \right\}, \\
 \vec{q}_3 &= q_{eq} \left( \frac{2}{\sqrt{3}}s\vec{e}_x + \frac{2}{\sqrt{3}}\vec{e}_y \right) = \{s; 1\}. \tag{3.58}
 \end{aligned}$$

These principle reciprocal lattice vectors are illustrated in Fig. 3.9. A minimal model of a triangular lattice can be constructed by considering only the lowest order reciprocal lattice vectors which correspond to  $\vec{q}_1$  and  $\vec{q}_2$  and  $\vec{q}_3 = -\vec{q}_1 - \vec{q}_2$ .

### 3 Modeling of anisotropic materials with arbitrary Poisson's ratio

---

The equation of motion for the amplitudes is determined by using a standard method of multiple-scale analysis [46, 83] in the limit of small parameter  $\chi$  which is  $-r$  in case of the APFC model. The density field amplitudes  $\eta_j$  need to be expanded in a power series in  $\chi^{1/2}$  and substituted into Eq. (3.55) to obtain dynamical equations at each order of  $\chi$ . These equations can be further solved by using a standard solvability condition [83] for complex amplitudes of the lowest-order reciprocal lattice vectors and to all orders in  $\chi$ . The corresponding resulting equations for the complex amplitudes  $\eta_j$  is given by

$$\frac{\partial \eta_j}{\partial t} = \mathcal{L}_j \left[ \Lambda_{j,s}^0 \eta_j + (3c\phi_0^2 + r)\eta_j + 3c\eta_j \left( 2 \sum_{k=1}^3 |\eta_k|^2 - |\eta_j|^2 \right) + 6c\phi_0 \prod_{k \neq j}^3 \eta_k^* \right], \quad (3.59)$$

where

$$\begin{aligned} \mathcal{L}_j &= \nabla^2 + 2i\vec{q}_j \cdot \vec{\nabla} - |\vec{q}_j|^2 \approx -|\vec{q}_j|^2, \\ \Lambda_{j,s}^0 &= (\widehat{\nabla}_{j,s}^2 + 1)^2. \end{aligned} \quad (3.60)$$

The expression for the  $\mathcal{L}_j$  can be simplified as  $\mathcal{L}_j = -|\vec{q}_j|^2$  for a long-wavelength approximation. The complex operator  $\widehat{\nabla}_{j,s}^2$  is derived from the Laplace operator Eq. (3.48) in the following form

$$\begin{aligned} \widehat{\nabla}_{j,s}^2 &= \nabla_{xx} + 2iq_{j,x}\nabla_x - q_{j,x}^2 \\ &\quad - 2s(\nabla_{xy} + i[q_{j,x}\nabla_y + q_{j,y}\nabla_x] - q_{j,x}q_{j,y}) \\ &\quad + (1 + s^2)(\nabla_{yy} + 2iq_{j,y}\nabla_y - q_{j,y}^2). \end{aligned} \quad (3.61)$$

The above expression can be further simplified as

$$\begin{aligned}
 \widehat{\nabla}_{j,s}^2 &= \nabla_s^2 + 2i\vec{q}_j \cdot \vec{\nabla}_s - [q_{j,x}^2 - 2sq_{j,x}q_{j,y} + (1+s^2)q_{j,y}^2] \\
 &\quad - 2siq_{j,y}\nabla_x + s^2 2iq_{j,y}\nabla_y \\
 &= \nabla_s^2 + 2i\vec{q}_j \cdot \vec{\nabla}_s - 2siq_{j,y}(\nabla_x - s\nabla_y) - 1,
 \end{aligned} \tag{3.62}$$

where the expression  $[q_{j,x}^2 - 2sq_{j,x}q_{j,y} + (1+s^2)q_{j,y}^2]$  is equal to 1 for all vectors  $\vec{q}_j$ . Using the anisotropic gradient

$$\vec{\nabla}_s = \nabla_x \vec{e}_x + \nabla_y (\vec{e}_y - s\vec{e}_x) \tag{3.63}$$

and the relation

$$\vec{q}_j \cdot \vec{\nabla}_s = \vec{q}_j \cdot \vec{\nabla} - sq_{j,x}\nabla_y, \tag{3.64}$$

the Eq. (3.62) can be expressed as:

$$\widehat{\nabla}_{j,s}^2 = \nabla_s^2 + 2i\vec{q}_j \cdot \vec{\nabla} - 2is(q_{j,x}\nabla_y + q_{j,y}\nabla_x) + 2is^2q_{j,y}\nabla_x - 1. \tag{3.65}$$

The newly derived equation of motion Eq. (3.59) can be written in a form of a PF model, i.e.

$$\frac{\partial \eta_j}{\partial t} = -|\vec{q}_j|^2 \frac{\delta F}{\delta \eta_j^*}, \tag{3.66}$$

with the free energy functional

$$\begin{aligned}
 F = & \int_V \left\{ \frac{1}{2}(3c\phi_0^2 + r)A^2 + \frac{3c}{4}A^4 + \sum_{j=1}^3 \left( |(\widehat{\nabla}_{j,s}^2 + 1)\eta_j|^2 - \frac{3c}{2}|\eta_j|^4 \right) \right. \\
 & \left. + 6c\phi_0 \left[ \prod_{j=1}^3 \eta_j + \prod_{j=1}^3 \eta_j^* \right] \right\} d\vec{r}, \tag{3.67}
 \end{aligned}$$

where  $A^2 = 2 \sum_{j=1}^3 |\eta_j|^2$ . This energy can be compared to the previously developed representation [39, 40] with exception of the anisotropic gradient term.

#### 3.5.2 Connection between the APFC model and traditional PF models

For a small deformation limit, the amplitudes  $\eta_j$  can be written in the form

$$\eta_j = \psi e^{i\vec{q}_j \cdot \vec{u}}, \tag{3.68}$$

where  $\psi$  is a phase-field variable which changes from 0 (in liquid phase) to a finite value (in solid phase) and  $\vec{u} = \{u_x, u_y\}$  is a vector which describes the displacement of atoms from a perfectly ordered crystal lattice. The connection with the standard PF model can be established by substituting  $\eta_j$  into Eq. (3.67) and expanding it up to the lowest-order nontrivial gradients in  $\psi$ . The resulting equation for the evolution of the phase-field variable can be expressed as

$$\begin{aligned}
 \frac{\partial \psi}{\partial t} = & \sum_j |\vec{q}_j|^2 \left[ 4 \left( \vec{q}_j \cdot \vec{\nabla}_s - sq_{j,y} (\nabla_x - s\nabla_y) \right)^2 \psi - 6(3c\psi_0^2 + r)\psi \right. \\
 & \left. - 12c\phi_0\psi^2 - 45c\psi^3 - 4(A_j + B_j s + C_j s^2)^2 \psi \right]. \tag{3.69}
 \end{aligned}$$

The first gradient term in Eq. (3.69) represents the anisotropy and the last term in

brackets accounts for the linear elastic energy. The terms  $A_j$ ,  $B_j$  and  $C_j$  depend on the displacement vector which could be obtained in each step of the simulation by solving the mechanical equilibrium equations. The above evolution equation contains the terms of the standard PF model such as the gradient term, the double well potential term and the chemical driving force. With the elastic energy contribution, the above evolution equation becomes similar to the recently developed PF models with elastic effects [84, 85]. Additionally, it contains the elastic terms which follow from the interaction of the small deformations with the lattice anisotropy  $s$  which provides the anisotropic elastic constants.

In order to further illustrate the terms appeared in the equation for the evolution of the phase-field variable (as given by Eq. (3.69)), the term  $A_j$  is defined from the second term of Eq. (3.62) as

$$\begin{aligned}
 A_j &= \left( \vec{q}_j \cdot \vec{\nabla} \right) (\vec{q}_j \cdot \vec{u}) \\
 &= (q_{j,x} \nabla_{j,x} + q_{j,y} \nabla_y) (q_{j,x} u_x + q_{j,y} u_y) \\
 &= q_{j,x}^2 U_{xx} + q_{j,y} q_{j,x} \nabla_y u_x + q_{j,x} q_y \nabla_x u_y + q_{j,y}^2 U_{yy} \\
 &= q_{j,x}^2 U_{xx} + q_{j,y}^2 U_{yy} + 2q_{j,y} q_{j,x} \left( \frac{\nabla_y u_x + \nabla_x u_y}{2} \right) \\
 &= q_{j,x}^2 U_{xx} + q_{j,y}^2 U_{yy} + 2q_{j,y} q_{j,x} U_{xy}, \tag{3.70}
 \end{aligned}$$

where  $u_i$  are the components of the displacement vector and  $U_{ij}$  are the components of the strain tensor and  $U_{xy} = \frac{1}{2} (\nabla_x u_y + \nabla_y u_x)$ . These components of the displacement vector and strain tensor can be obtained from the mechanical equilibrium equations. The sum  $\sum_j |\vec{q}_j|^2 A_j^2$  can be calculated as

$$\begin{aligned}
 \sum_j |\vec{q}_j|^2 A_j^2 &= \sum_j (q_{j,x}^2 + q_{j,y}^2) (q_{j,x}^4 U_{xx}^2 + q_{j,y}^4 U_{yy}^2 + 4q_{j,x}^2 q_{j,y}^2 U_{xy} \\
 &\quad + 2q_{j,x}^2 q_{j,y}^2 U_{xx} U_{yy} + 4q_{j,y}^3 q_{j,x} U_{yy} U_{xy} + 4q_{j,x}^3 q_{j,y} U_{xy} U_{xx}). \tag{3.71}
 \end{aligned}$$

### 3 Modeling of anisotropic materials with arbitrary Poisson's ratio

---

The above expression can be further simplified for an isotropic case by using  $s = 0$ , i.e.

$$\sum_j A_j^2 = \frac{3}{4} \left[ \frac{3}{2} U_{xx}^2 + \frac{3}{2} U_{yy}^2 + 2U_{xy}^2 + U_{xx}U_{yy} \right]. \quad (3.72)$$

This resulting expression is comparable to the equation derived for an isotropic binary PFC model [41].

Similarly, second and third terms ( $B_j$  and  $C_i$ ) can also be evaluated on the similar lines from the third and fourth terms of Eq. (3.62), i.e.

$$\begin{aligned} B_j &= (q_{j,x} \nabla_y + q_{j,y} \nabla_x) (\vec{q}_j \cdot \vec{u}) \\ &= (q_{j,x} \nabla_y + q_{j,y} \nabla_x) \cdot (q_{j,x} u_x + q_{j,y} u_y) \\ &= q_{j,x}^2 \nabla_y u_x + q_{j,x} q_{j,y} U_{xx} + q_{j,x} q_{j,y} U_{yy} + q_{j,y}^2 \nabla_x u_y, \end{aligned} \quad (3.73)$$

and

$$\begin{aligned} C_j &= q_{j,y} \nabla_y (\vec{q}_j \cdot \vec{u}) \\ &= q_{j,y} \nabla_y (q_{j,x} u_x + q_{j,y} u_y) \\ &= q_{j,y} q_{j,x} \nabla_y u_x + q_{j,y}^2 U_{yy}. \end{aligned} \quad (3.74)$$

Finally, from the above expressions of  $B_j$  and  $C_i$ , the important gradient term can be calculated as

$$\begin{aligned}
 \sum_j |\vec{q}_j|^2 B_j^2 &= \sum_j (q_{j,x}^2 + q_{j,y}^2) (q_{j,x}^2 q_{j,y}^2 (U_{xx} + U_{yy})^2 + q_{j,x}^4 (\nabla_y u_x)^2 + q_{j,y}^4 (\nabla_x u_y)^2 \\
 &+ 2q_{j,x}^3 q_{j,y} (\nabla_y u_x) (U_{xx} + U_{yy}) + 2q_{j,y}^3 q_{j,x} (\nabla_x u_y) (U_{xx} + U_{yy}) \\
 &+ 2q_{j,x}^2 q_{j,y}^2 (\nabla_y u_x) (\nabla_x u_y)) \quad (3.75)
 \end{aligned}$$

and

$$\sum_j |\vec{q}_j|^2 C_j^2 = \sum_j (q_{j,x}^2 + q_{j,y}^2) (q_{j,y} q_{j,x} \nabla_y u_x + q_{j,y}^2 U_{yy}). \quad (3.76)$$

### 3.5.3 Evaluation of computational efficiency

In this section, a detailed analysis of the computational efficiency is performed by comparing the simulation results obtained from the originally introduced APFC model based on Eq. (3.55) with the PF model expressed by eq. (3.69) without elastic terms. More specifically, the growth of a crystalline phase from the liquid phase is simulated with the evolution equations based on both the originally introduced APFC model and the phase-field evolution equation by initialization a small crystal nucleus in the center of a square simulation box of size 512 x 512. The phase-field evolution equation is further simplified by omitting the term  $sq_{j,y}(\nabla_x - s\nabla_y)$  which is responsible for the gradient anisotropy. Fig. 3.10 illustrates the results obtained from the simulation performed with the originally introduced APFC model and the amplitude evolution equation for  $s = 0.2$ ,  $r = -0.25$ ,  $c = 1$  and  $\phi_0 = 0.28$  without elastic effects.

Fig. 3.10 clearly demonstrates that the resulting crystalline phase has a pronounced anisotropic form extended in the direction of  $\vec{e}_y^s$ . The anisotropic strength which is characterized by the parameter  $s$ , can be compared to the standard twofold anisotropy in the phase-field model. Furthermore, the anisotropic growth kinetic in the phase-field representation is related to the anisotropy of the crystal inter-plane distances for various crystal facets (just like the APFC model) and hence to the anisotropic surface energy.

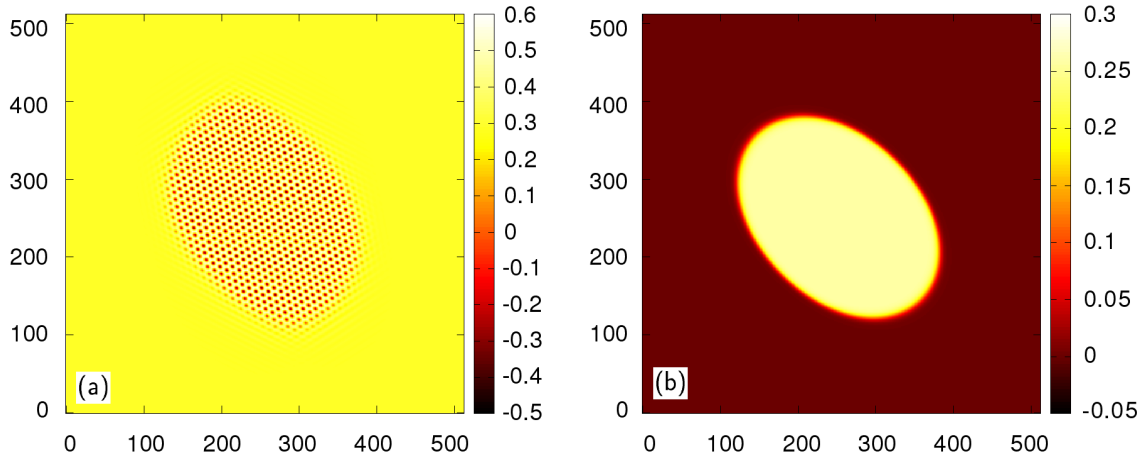


**Figure 3.10:** The anisotropic crystal simulated by (a) the APFC model and (b) the amplitude evolution equation.

The comparison of the simulation results obtained for both cases shows that the phase-field evolution equation follows the evolution of the crystal calculated from the APFC model without resolving the details of atomic structure and with smoothening of the crystal edges. However, for a quantitative comparison of the computational efficiency, the CPU time of both simulations is calculated for a typical run of 20,000 steps with  $dt = 0.00075$ . The comparison shows that simulations performed with the APFC model took 10 minutes to reach the typical reference state, whereas, simulations performed with the phase-field amplitude evolution equation took only 1 second to reach the similar state. Thus it can be concluded that the computational efficiency is increased by 600 times in case of the phase-field amplitude evolution equation. This increase in computational efficiency illustrates that the newly derived amplitude evolution equation allows a fast estimation of the solidification behavior of anisotropic crystals and crystals under applied stress by building a bridge upon the multiple-scale approach.

## 3.6 Discussion

In this chapter, the basic formulation of the APFC model is presented along with the DDFT based calibration of the model, i.e. the derivation of its model parameters from the DDFT which provided the physical justification for the model. The unique feature of the APFC model, that it can simulate isotropic as well as anisotropic materials with arbitrary Poisson's ratio, is highlighted by demonstrating the simulation results obtained with various set of model parameters. These distinguish features of the APFC model overcome the limitations of the originally introduced PFC model [7] (which can only model materials with Poisson's ratio of 1/3) and thus allows further extension of the applicability of the PFC approach to a wider class of material systems. In particular, this offers the chance of prospectively contributing to a mechanistic understanding of material systems of recent interest such as gum metals or dilational materials.

Furthermore, the amplitude formulation of the APFC model is also presented which can be applied to dynamics of two-phase systems with anisotropic properties. In particular, the relationship between the amplitude evolution equation and the corresponding evolution equation for the standard PF models with elasticity is established which bridges the PF and PFC approaches for anisotropic crystals and thus provides an explicit connection between the APFC model and the standard PF models. Moreover, the simulation results demonstrated that these amplitude evolution equations increased the computational efficiency by many times and are capable of performing fast simulations of the solidification of anisotropic crystals and crystals under stress with additional elastic effects by building a bridge upon the multiple-scale approach. Thus, the deviation of the amplitude formulation for the APFC model provided on one hand a tremendous enhancement in the computational efficiency as well as a bridge between the PFC and traditional PF models on the other hand.



## 4 Investigating the equilibrium properties of the liquid-solid interface \*

The previous chapter demonstrated the development of a more generalized APFC model within the framework of the PFC method with the capability of modeling material systems with arbitrary Poisson's ratio [8, 9, 10]. This chapter goes a step further by focusing on the basic application of this thesis to study nucleation mechanisms associated with binary systems which certainly have higher industrial relevance. Particularly it is applied here to advance beyond classical nucleation theory (CNT).

Most of the binary systems rely heavily on the physics associated with the important morphological features of interface boundaries between different phases at atomistic level in order to achieve desired properties. In particular, liquid-solid interfaces play an important role in a number of phenomena encountered in physical processes. The understanding of structural and thermodynamic aspects of liquid-solid interfaces is a key element to understand various phenomena such as vaporization and condensation transformations, because interface boundaries play an important role in recrystallization. The role of interfaces is not only restricted to the growth process, since interfaces are also an important feature of the resulting microstructures which indeed play a vital role in determining the material properties. One of the most important interfacial properties is the surface tension, which is a key ingredient to determine the behavior and control of several phenomena of high industrial applications [86]. For example, nanoparticles can be directed to self-assemble into thin films at an oil/water interface by manipulating the solid/water and solid/oil surface tensions [87]. Therefore, keeping in mind the importance of liquid-solid interfaces

---

\*Parts of this chapter are already published in [11, 12].

and associated surface energies, the motivation behind this chapter is to establish a new methodological approach, that can get hand on interfacial energies beyond classical predictions.

There have been many theoretical attempts to estimate the surface tension, but, these estimates only reflect an approximate value of the surface tension due to the number of assumptions used in these calculations. In contrast, several simulation techniques provide the possibility to compute the surface tension with much higher accuracy. In particular, the PFC method derives its attractiveness from the fact that unlike other traditional methods, it allows to model and simulate the dynamics of interfaces without any explicit tracking of the interface [1, 7]. This chapter presents a detailed investigation of the curved liquid-solid interface using the finite system size approach. More specifically, a quantitative analysis of the liquid-solid surface tensions of critical nuclei and nucleation barriers is presented in this chapter. A two-dimensional PFC model for binary systems based on Elder et al. [1] is used to study critical nuclei near the liquid-solid phase boundary. The main aim of these investigations is to establish the usefulness of the finite box size approach (as evolves in [88, 89, 90]) to the study of critical nuclei for the liquid-solid transition as well as to address the problem of defining droplet radii in a two-component mixture. In addition to that, these investigations are also aimed to obtained a more precise assessment of crystal nucleation in the context of binary systems beyond predictions based on CNT.

This chapter is organized as follows. Firstly, a brief overview of the theoretical aspects of the crystalline growth process via metastable nuclei and the existing theoretical models, is presented in sect. 4.1. Then a detailed description of the PFC model for binary alloys is presented in sect. 4.2. Then, the development of the phase diagram by considering the one-mode approximation technique and full dynamics is presented in sect. 4.3. The method used to extract the surface energy from the free energy of a finite size simulation box containing a crystal cluster in equilibrium with the surrounding liquid phase as well as liquid droplets in equilibrium with the surrounding solid phase, is discussed in sect. 4.4. The free energies of the curved liquid-solid interface and the nucleation barriers are calculated for various cluster sizes depending on the initial supersaturation and the corresponding

equilibrium solid fraction in sect. 4.7 and 4.8. Furthermore, a comparison of simulation results with the CNT and the well established non-classical Tolman theory is also presented. Finally, the important concluding remarks from this study are summarized in sect. 4.9.

### 4.1 Theoretical picture of crystalline growth process via metastable nuclei

The formation of a crystalline phase in an undercooled melt proceeds via the appearance and disappearance of nanoscopic crystalline nuclei. Once these nuclei have reached a certain size, commonly known as critical size, they are able to grow. The time scale for entering this particular growth regime is mainly determined by the difference of the grand free energy between the critical nucleus and the reference state of the homogeneous undercooled melt. This difference of the grand free energy is commonly termed as nucleation barrier. The use of the notion of free energy for such a nonequilibrium process implicitly means the use of a picture of quasi-equilibrium changes making up the process. Furthermore, these critical nuclei are described as saddle point solutions in the free energy landscape in the context of a mean-field picture for the quasi-equilibrium changes. For a proper description of crystalline growth process, it is very important to develop a better understanding of the kinetics associated with the nanoscopic crystalline nuclei [12].

In general, proper investigation of metastable configurations through numerical simulations does require large system sizes in order to ensure a reasonable solution. Simulation performed for such large system sizes poses many new challenges concerning the computational efficiency. To overcome this limitation, a relatively new technique known as finite size approach, has been proposed and is being widely used in a very successful manner.

### 4.1.1 Finite size effect approach

This approach suggests that instead of determining metastable configurations in large volumes or boxes, a smaller simulation box with a fixed particle number (i.e. the canonical ensemble) may be utilized to stabilize critical nuclei. This has been demonstrated successfully as a quantitative route in Monte-Carlo (MC) simulations to assess the nucleation barriers for the nucleation of liquid droplets in vapor [88, 89, 90], and it works equally well using DFT [89, 90]. For a given box size, the transitions from supersaturated vapor to undersaturated liquid follow the subsequent sequence:

supersaturated vapor  $\rightarrow$  liquid droplets  $\rightarrow$  liquid cylinders  $\rightarrow$  planar liquid slabs  $\rightarrow$  vapor cylinders  $\rightarrow$  vapor droplets  $\rightarrow$  undersaturated liquid,

as the number of particles are increased in the box (i.e. increase in the density from the one of the coexisting vapor to the one of the coexisting liquid) [91]. Therefore, droplets with a radius falling into a limited range can be stabilized for a given finite box size. A larger range of droplet radii can be obtained by combining the droplet stability windows of boxes with different sizes. After the successful implementation of this approach in the investigation of nucleation of liquid droplets in vapor, it can be stated that this route should also work for crystal nucleation in the liquid phase, as long as there is a density difference between the coexisting crystal and liquid phases. Furthermore, this technique can also be used for analyzing solid-solid demixing [92].

### 4.1.2 Existing theoretical models

In 1990's, several non-classical relations were developed to describe the dependence of the surface energy on the undercooling as well the critical nucleus size beyond the predictions based on CNT. Some well recognized non-classical theories in this context include the modified self-consistent classical theory [93, 94], the field theo-

retic approaches based on the DFT [95, 96, 97] and the Granasy's diffusion interface theory (DIT) [98, 99]. The promising features of these existing theories are summarized by Granasy et al. in a recent review [100]. Furthermore, these non-classical theories [94, 101] also proposed phenomenological dependence of the surface tension on the nucleus size.

A well established non-classical thermodynamic theory to describe the surface tension for a liquid droplet existing in equilibrium with the vapour phase was developed by Tolman [102]. This theory suggests that the curvature dependence of the surface tension of small droplets can be described as

$$\gamma(r) = \frac{\gamma_\infty}{1 + \frac{\delta_T}{r}}, \quad (4.1)$$

where the phenomenological length scale  $\delta_T$  being the famous Tolman length. It is still difficult to give  $\delta_T$  a precise meaning in the context of statistical mechanics [91] and the dependence of  $\delta_T$  on temperature is also still under discussion [103, 104, 105]. The details of all important developments in this context are summarized by Tröster et al. in a recent review [90]. The interfacial free energy of small crystalline particles is also expected to depend on size, due to the decrease in the average number of solid neighbors for molecules on curved surfaces relative to that on a planar interface [106].

### 4.1.3 Support from computational studies

The theoretical picture of the crystalline growth process has received support from simulation work in which slow variables (reaction coordinates, such as radius of particles or particle numbers in crystalline nuclei) are defined and quasi-equilibrium averages are computed with respect to all other variables [107, 108]. Results for the nucleation barrier  $\Delta\Omega$  from such computations are often interpreted using the expression from CNT:

$$\Delta\Omega = -\Delta\mu\rho_c V + \gamma A, \quad (4.2)$$

where  $V$  and  $A$  are the volume and surface area of the nucleus,  $\Delta\mu$  is the chemical potential difference between the undercooled liquid and the crystalline state in the nucleus,  $\rho_c$  is the crystal density in the nucleus and  $\gamma$  is the surface tension. For further simplification,  $\gamma$  can be assumed to be the surface tension of a planar liquid-solid interface ( $\gamma_\infty$ ). However, some recently reported simulation results indicate deviations from this approximation depending on size and shape of the nuclei [108]. Furthermore, even if  $\gamma_\infty$  is strictly not constant (as it would be in the liquid-vapor case), it depends on the orientation of the crystal with respect to the interface normal [12].

Therefore, it is desirable to analyze critical crystalline nuclei in mean-field theories where they are not as elusive as in simulations. In DFT, reliable functionals are usually nonlocal in the particle density field and computationally much expensive technique, thus, due to its high computational resources requirements, the investigation of critical crystalline nuclei have not been performed yet. However, quite a number of investigations exists for a liquid droplet nucleation in supersaturated vapor (for recent work see e.g. Ref. [109]). As an alternative to the CDFT, the PFC method being local in the order parameter field can be used as a computationally more efficient approach to address such a problem. Nevertheless, direct methods to determine saddle points corresponding to a critical nucleus are still not easy to handle and they are also rather time consuming. For the simplest one-component PFC model in three dimensions, this has been done for one particular undercooled state [110]. Furthermore, a two-dimensional study of critical nuclei at walls using direct methods for saddle point location is also reported by G. I. Toth et al. [111] and R. Backofen et al. [112]. Even though the PFC model is computationally much more accessible and an attractive alternative to the still more demanding nonlocal DDFT calculations for crystals, the equilibration of the droplet solutions is occasionally slow. However, the PFC simulations in conjunction with the finite system size technique certainly can have prospective to assess more sophisticated systems with perhaps a variety of shapes of critical nuclei.

## 4.2 PFC model for binary systems

A two-dimensional PFC model for binary systems based on Elder et al. [1] is used to investigate the equilibrium properties of the liquid-solid interface. This model has been chosen due to its potential for future investigations, i.e. besides a liquid-solid transition its phase diagram has an eutectic point and thus it can also be used to investigate the solid-solid phase transition. To that end the following representation follows [1, 12].

### Free energy functional and systems dynamics

A binary system composed of two components A and B is considered with each component having its own representative (coarse-grained) atomic number densities, i.e.  $\rho_A$  and  $\rho_B$ , respectively. The free energy of such a binary system includes the contribution from the energy of the density fields of both components and their interaction. The dimensionless and shifted atomic density field,  $n$ , and the relative concentration field,  $c$ , are introduced to simplify the model. The dimensional atomic density field and the concentration field can be expressed as,

$$\begin{aligned} n &= \frac{\rho_A + \rho_B}{\bar{\rho}_A + \bar{\rho}_B} - 1, \\ c &= \frac{\rho_B - \rho_A}{\bar{\rho}_A + \bar{\rho}_B}, \end{aligned} \quad (4.3)$$

where  $\bar{\rho}_A$  and  $\bar{\rho}_B$  are the average atomic number densities of components in the liquid phase.

The free energy functional for a binary system is derived in [1] in the form

$$\mathcal{F} = \int F(n, c) d\vec{r}, \quad (4.4)$$

## 4 Investigating the equilibrium properties of the liquid-solid interface

---

with the total free energy density

$$\begin{aligned}
 F(n, c) &= \frac{n}{2} [B^l + B^s(2R^2\nabla^2 + R^4\nabla^4)] n - \frac{t}{3}n^3 + \frac{v}{4}n^4 \\
 &+ \Gamma c + \frac{w}{2}c^2 + \frac{\xi}{2}c^3 + \frac{u}{4}c^4 + \frac{\epsilon^2}{2}|\vec{\nabla}c|^2 + \dots,
 \end{aligned} \tag{4.5}$$

where  $t$ ,  $v$ ,  $\Gamma$ ,  $w$ ,  $\xi$ ,  $u$  and  $\epsilon$  are constant model parameters. However,  $B^l$ ,  $B^s$  and  $R$  depend on the concentration and can be expressed by Taylor expansion. For simplicity, it is assumed that  $B_0^l$ ,  $B_0^s$ ,  $B_2^l$ ,  $R_0$  and  $R_1$  are the only non-zero Taylor coefficients. These non-zero Taylor coefficients can be expressed as

$$\begin{aligned}
 B^l &= B_0^l + B_2^l c^2, \\
 B^s &= B_0^s, \\
 R &= R_0 + R_1 c.
 \end{aligned} \tag{4.6}$$

Here, the difference  $\Delta B_0 = B_0^l - B_0^s$  plays the role of a shifted and rescaled temperature. The gradient terms in front of  $n$  favor crystalline order with a lattice constant of order  $R$ . If  $R_1 \neq 0$ , the lattice constant will be concentration dependent (lattice misfit). It can be assumed that this model can describe a solid solution since the prefactor of the gradient term  $|\vec{\nabla}c|^2$  is positive (free energy cost for a spatially varying concentration) and a term  $\propto c\nabla^4 c$  is absent.

Considering substitutional diffusion between both components  $A$  and  $B$ , i.e. equal mobility of the components, results in decoupled dynamical equations for  $n$  and  $c$ . Moreover, the dynamical equations can be further simplified by assuming a constant mobility ( $M$ ). The resulting dynamical equations (introduced in [1]) can be written as

$$\frac{\partial n}{\partial t} = M\nabla^2 \frac{\delta \mathcal{F}}{\delta n}, \tag{4.7}$$

$$\frac{\partial c}{\partial t} = M\nabla^2 \frac{\delta \mathcal{F}}{\delta c}. \tag{4.8}$$

The derivative of the free energy with respect to the atomic density can be obtained by using the free energy expression Eq. (4.5), i.e.

$$\begin{aligned} \frac{\delta \mathcal{F}}{\delta n} &= nB^l - tn^2 + vn^3 + \frac{B_0^s R^2}{2} [(2\nabla^2 + R^2\nabla^4)n] \\ &+ \frac{B_0^s}{2} [2\nabla^2(nR^2) + \nabla^4(nR^4)] \end{aligned} \quad (4.9)$$

and the derivative of the free energy with respect to the concentration field, i.e.

$$\begin{aligned} \frac{\delta \mathcal{F}}{\delta c} &= B_2^l cn^2 + 2B_0^s nR_1R [\nabla^2 + R^2\nabla^4] n \\ &+ \Gamma + wc + \xi c^2 + uc^3 - \epsilon^2 \nabla^2 c. \end{aligned} \quad (4.10)$$

## 4.3 Equilibrium phase properties

In this section, a brief explanation of the method of the evaluation of the equilibrium phase diagram for the free energy functional of the binary PFC model using one-mode approximation and the coarse-graining assumption (according to the ref.[1]), is presented. The method is further extended by taking into account the periodic variation of the concentration in the bulk state at the scale of the atoms and developing the full phase diagram in a  $n$ - $c$ -space (discussed in sect. 4.3.2) . The isothermal section of the calculated phase diagram is used for the investigation of the interface tension as discussed in the following sections of this chapter.

### 4.3.1 Phase diagram based on the coarse-graining assumption

The phase diagram of the binary PFC model has been studied in [1] using the coarse-graining assumption that  $c$  varies more smoothly (on a larger length scales) than  $n$ . Thus, in bulk crystalline states  $n$  varies periodically while  $c$  is constant and coexisting

## 4 Investigating the equilibrium properties of the liquid-solid interface

---

phases can be characterized by a constant average total density  $n_0$ , an equality of the chemical potential  $\mu_c = \partial F/\partial c$  and the pressure  $p = \mu_n n + \mu_c c - F(n, c)$  at coexistence values  $c_l$  and  $c_s$  of the concentration in liquid and solid phases. In other words, the conditions for the existence of a stationary solution correspond to the equality of chemical and grand potentials. The calculation of the bulk free energy can be simplified using the one-mode approximation (as discussed in [1]). This technique is applied to initialize the total density  $n$  in the solid phase as

$$n = n_0 + A \left[ 0.5 \cos(2qy/\sqrt{3}) - \cos(qx) \cos(qy/\sqrt{3}) \right]. \quad (4.11)$$

Inserting this expression into Eq. (4.5) and then minimizing with respect to  $q$  and  $A$  gives the equilibrium wave number and the minimized amplitude:

$$\begin{aligned} q_{\text{eq}} &= \frac{\sqrt{3}}{2R}, \\ A_{\text{min}} &= \frac{4 \left( t - 3vn_0 + \sqrt{t^2 + 24tvn_0 - 36v^2n_0^2 - 15v\Delta B} \right)}{15v} \end{aligned} \quad (4.12)$$

where  $\Delta B = B^l - B^s = \Delta B_0 + B_2^l c^2$ .

It is important also to mention that the lattice constant  $a$  can be defined in terms of  $q_{\text{eq}}$  as:

$$a = 2\pi/q_{\text{eq}} = 4\pi R/\sqrt{3}. \quad (4.13)$$

Substituting Eq. (4.12) into Eq. (4.5) and using  $n_0 = 0$  gives an expression for the free energy density of the solid phase that is minimized with respect to crystal lattice constant and amplitude, i.e.

$$F_s = \Gamma c + \frac{w}{2}c^2 + \frac{\xi}{2}c^3 + \frac{u}{4}c^4 + \frac{3}{16}\Delta B A_{\min}^2 - \frac{t}{16}A_{\min}^3 + \frac{45v}{512}A_{\min}^4. \quad (4.14)$$

In liquid-solid coexistence region, the free energy of the liquid phase can be compared with the free energy of the solid phase. The expression for the mean field free energy for the liquid phase can be obtained from Eq. (4.14) by setting  $n_0 = 0$ , i.e.

$$F_l = \Gamma c + \frac{w}{2}c^2 + \frac{\xi}{2}c^3 + \frac{u}{4}c^4. \quad (4.15)$$

The Maxwell's construction rule is then used to identify the liquid-solid coexistence lines. Using this technique, it has been found for the exemplary choice  $n_0 = 0$  in both phases that for  $w > 0$  there are two separate branches in the phase diagram (temperature-concentration  $[\Delta B_0-c]$  plane) [1]. For temperatures above a critical one,  $\Delta B_0 > \Delta B_{0,1}$ , there is liquid-solid coexistence, for temperatures below a second critical one,  $\Delta B_0 < \Delta B_{0,2}$ , there is solid-solid demixing. Both branches are separated in temperatures  $\Delta B_{0,1} > \Delta B_{0,2}$  for  $w$  being larger than a certain threshold value  $w_0$ . For  $w < w_0$ , the two branches meet and  $\Delta B_{0,1} = \Delta B_{0,2} = \Delta B_{0,c}$  corresponds to a eutectic temperature. Fig. 4.1 demonstrates an example of the one-mode phase diagram in the eutectic regime for the parameters given in Table 4.1.

The calculations based on [1] results in a dotted line at  $\Delta B_{0,c} \approx 0.0282$  in Fig. 4.1 which shows the location of the eutectic temperature, above this line there is possible liquid-solid coexistence and below is the solid-solid coexistence. The dashed lines in Fig. 4.1 indicate a metastable solid-solid transition and the full line at  $\Delta B_0 = 0.05$  indicates where nucleation is investigated in this chapter.

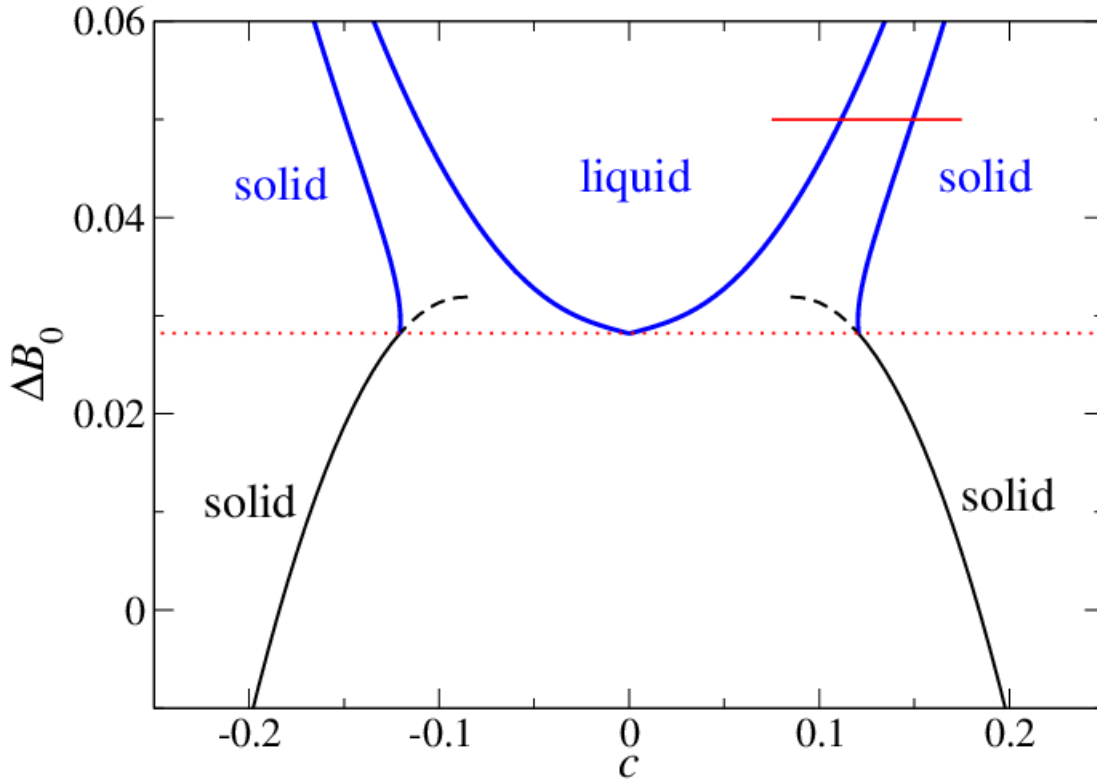


**Figure 4.1:** The phase diagram of the model in one-mode approximation, using  $n_0 = 0$  and the parameters given in Table 4.1. It follows Figure 3 in [1].

### 4.3.2 Further development of the full phase diagram in $n$ - $c$ -space

The coarse-graining assumption (discussed in sect. 4.3.1) used in the development of the one-mode phase diagram [1] is not valid strictly, i.e. the concentration field also vary periodically for a bulk crystal. Therefore, coexistence is characterized by a pair of variables  $(n_l, c_l)$  and  $(n_s, c_s)$  for liquid and solid density and concentration, respectively, where  $n_l \neq n_s$  in general. It is important to mention that at coexistence, the values for both chemical potentials  $\mu_c = \partial F / \partial c$ ,  $\mu_n = \partial F / \partial n$  and the pressure  $p = \mu_n n + \mu_c c - F(n, c)$  must agree in the liquid and solid phase.

### Validation of PFC results through mode expansion technique

The calibration of the PFC model for binary alloys based on the classical DFT was proposed by Elder et al. [1]. More specifically, its connection with the DFT was established through the parameterization of the direct two-point correlation function which enters in DFT by the quantities which are related to the elastic energy stored in the solid and liquid phases, as well as the lattice constant of the material systems [1].

However, in order to further extend the one-mode phase diagram (shown in Fig. 4.1) and to develop a full phase diagram in  $n$ - $c$  space, the co-existence data obtained from the PFC simulations needs to be verified through some well established method. A fast routine for determining crystal solutions with minimized free energy is most crucial for obtaining coexistence in order to verify the PFC results. This can be found by expanding both  $n$  and  $c$  in reciprocal lattice modes of a triangular lattice and rewriting the free energy Eq. (4.5) in terms of these modes. Then  $F$  is minimized by using the simulated annealing method (as described in Ref. [113]) and a truncation to 5 modes. This free energy routine was subsequently employed to determine the phase boundaries via the Maxwell construction. The set of numerical equations for the equality of pressure and the two chemical potentials on the liquid and solid side was solved with a Newton-Raphson method. This DDFT type expansion is developed and applied by Martin Oettel in the joint work [12]. More specifically, the coexistence data (chemical potentials  $\mu_n$  and  $\mu_c$  as well as the free energies of phases) obtained from the PFC code is validated through a close comparison with the values calculated from the mode expansion technique for the given  $c^{\text{eq}}$  and  $n_0^{\text{eq}}$ . The difference of the resulting values obtained from both methods is found to be smaller than 0.1%.

### Isothermal phase diagram

The following summarizes the further results by which the PFC method is established and employed in the finite system size technique for fundamentals of nucleation theory (it follows [12]). For a specific set of model parameters (as given in

#### 4 Investigating the equilibrium properties of the liquid-solid interface

Table 4.1) used in the following investigations, the equilibrium densities of phases at coexistence ( $n^{eq}, c_0^{eq}$ ) at the temperature  $\Delta B_0 = B_0^l - B_0^s = 0.05$  are calculated according to the procedure described above. The corresponding isothermal section of the phase diagram is presented in Fig. 4.2. The range of the mean density and the mean composition ( $\bar{n}_0, \bar{c}$ ) used to perform simulations in this chapter is illustrated by a dashed line and the liquid-solid coexistence line are shown as dotted lines in Fig. 4.2.

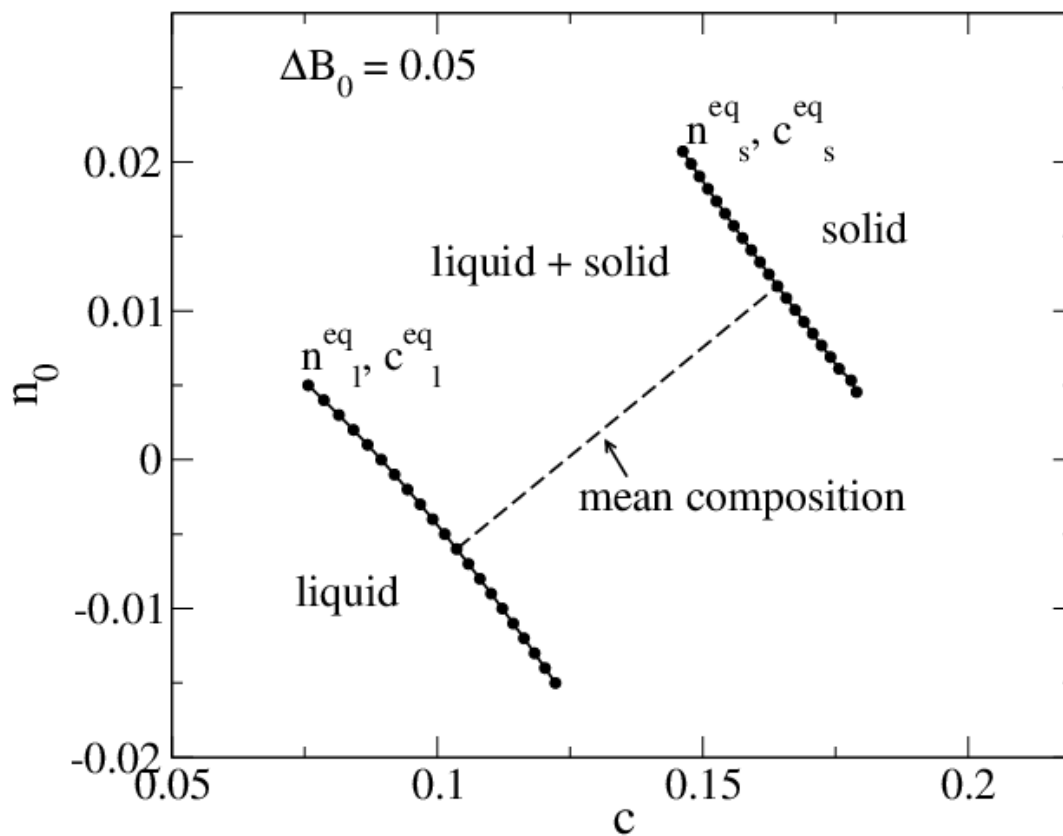
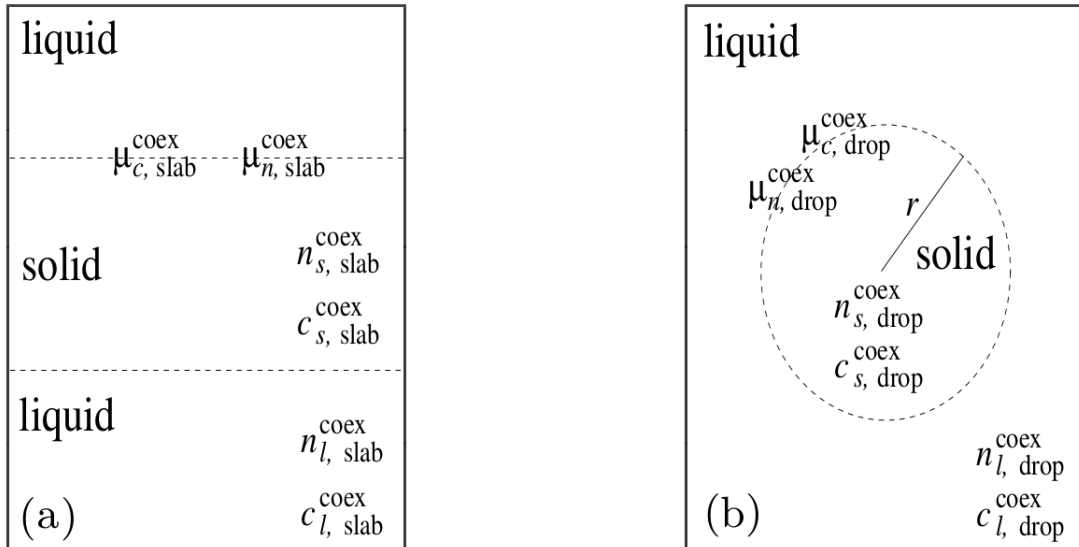


**Figure 4.2:** The isothermal section of the phase diagram at  $\Delta B_0 = 0.05$  for the parameters given in Table 4.1. Figure already published in [12]

## 4.4 Method of the investigation of the interfacial energy

### 4.4.1 A theoretical picture

In this section, the method of the extraction of the interfacial free energy  $\mathcal{F}_I$  and the interface line tension  $f_I = \mathcal{F}_I/l$  (where  $l$  is the circumference of the interface) from the numerical data is discussed in detail following [12]. Fig. 4.3 illustrates the definitions of some necessary parameters used in this section.



$$\text{use } \textit{bulk} \text{ equilibrium: } \begin{aligned} n_{s[l], \text{ drop}}^{\text{coex}} &= n_{s[l]}(\mu_n^{\text{coex}}, \mu_c^{\text{coex}}) \\ c_{s[l], \text{ drop}}^{\text{coex}} &= c_{s[l]}(\mu_n^{\text{coex}}, \mu_c^{\text{coex}}) \end{aligned}$$

**Figure 4.3:** (a) A planar solid slab and (b) a solid nucleus with radius  $r$  stabilized in the finite simulation box. Figure already published in [12].

Fig. 4.3(a) indicates that the chemical potentials for the two species are constant across the simulation box and are at the coexistence values  $\mu_{n[c], \text{slab}}^{\text{coex}}$ . The densities  $n$  and  $c$  for the solid ( $s$ ) and liquid ( $l$ ) phase corresponds to their bulk coexistence values  $n_{l[s], \text{slab}}^{\text{coex}}$  and  $c_{l[s], \text{slab}}^{\text{coex}}$ . Similarly, Fig. 4.3(b) indicates that the chemical potentials

## 4 Investigating the equilibrium properties of the liquid-solid interface

---

for the two species are constant across the simulation box but different from the slab coexistence values,  $\mu_{n[c],\text{drop}}^{\text{coex}} \neq \mu_{n[c],\text{slab}}^{\text{coex}}$ . The densities  $n$  and  $c$  for the solid ( $s$ ) and liquid ( $l$ ) phase are at their coexistence values  $n_{l[s],\text{drop}}^{\text{coex}}$  and  $c_{l[s],\text{drop}}^{\text{coex}}$ . It is important to mention that for both (drop and slab) configurations, the coexisting densities for the solid (liquid) phase  $n_{l[s],\text{drop[slab]}}^{\text{coex}}$  and  $c_{l[s],\text{drop[slab]}}^{\text{coex}}$  are defined as the bulk densities in the solid (liquid) phase having the chemical potentials  $\mu_{n,\text{drop[slab]}}^{\text{coex}}$  and  $\mu_{c,\text{drop[slab]}}^{\text{coex}}$  using a solid (liquid) unit cell. The simulation results showed that for larger nuclei the average densities extracted from the center of the nucleus agrees with the pure bulk densities, however, for smaller nuclei, this is not necessarily the case.

As it is well-known from droplet thermodynamics, there is some arbitrariness in the definition of the interface tension due to the freedom in the choice of radius  $r$  [90]. However, an excess grand free energy of a solid droplet can be uniquely defined as the difference in grand potential,  $\Omega = \int d\vec{r}(F - \mu_n n(\vec{r}) - \mu_c c(\vec{r}))$ , between the system with droplet and the system without droplet at the same chemical potentials  $\mu_{n,\text{drop}}^{\text{coex}}$  and  $\mu_{c,\text{drop}}^{\text{coex}}$  (which gives rise to the densities  $n_{l,\text{drop}}^{\text{coex}}$  and  $c_{l,\text{drop}}^{\text{coex}}$  in the bulk liquid):

$$\Delta\Omega = \int_{\text{box}} d\vec{r} \left[ F(n(\vec{r}), c(\vec{r})) - F_l(n_{l,\text{drop}}^{\text{coex}}, c_{l,\text{drop}}^{\text{coex}}) - \mu_{n,\text{drop}}^{\text{coex}} (n(\vec{r}) - n_{l,\text{drop}}^{\text{coex}}) - \mu_{c,\text{drop}}^{\text{coex}} (c(\vec{r}) - c_{l,\text{drop}}^{\text{coex}}) \right]. \quad (4.16)$$

Here, the densities  $n(\vec{r}), c(\vec{r})$  and the corresponding free energy density  $F(n(\vec{r}), c(\vec{r}))$  are evaluated from the full stable droplet solution in the finite box with volume  $A_{\text{box}}$ . In physical terms, this excess grand free energy is the nucleation barrier and it does not depend on the choice of a dividing surface between liquid and solid. It contains a contribution proportional to the droplet volume  $A_{\text{drop}}$  (which has the dimension of an area in the current 2D system). For large droplets (thermodynamic limit) it is clear that this contribution is proportional to the grand free energy difference of the bulk solid and liquid phase, i.e.

#### 4.4 Method of the investigation of the interfacial energy

$$\Delta\Omega_{\text{drop}} = \Omega_{\text{sol,drop}}(n_{s,\text{drop}}^{\text{coex}}, c_{s,\text{drop}}^{\text{coex}}) - \Omega_{\text{liq,drop}}(n_{l,\text{drop}}^{\text{coex}}, c_{l,\text{drop}}^{\text{coex}}), \quad (4.17)$$

where the bulk average solid densities  $n_{s,\text{drop}}^{\text{coex}}$ ,  $c_{s,\text{drop}}^{\text{coex}}$  correspond to the chemical potentials  $\mu_{n,\text{drop}}^{\text{coex}}$  and  $\mu_{c,\text{drop}}^{\text{coex}}$  evaluated over  $A_{\text{drop}}$ . The interfacial free energy  $\mathcal{F}_I$  for smaller droplets can be expressed by defining a dividing surface between solid and liquid (thus defining  $A_{\text{drop}}$ ) and then subtracting this bulk contribution  $\Delta\Omega_{\text{drop}}$  from the nucleation barrier  $\Delta\Omega$ , i.e.

$$\begin{aligned} \mathcal{F}_I &= \Delta\Omega - \Delta\Omega_{\text{drop}} \\ &= \int_{\text{box}} d\vec{r} (F(n(\vec{r}), c(\vec{r})) - \\ &\quad \int_{\text{box} \setminus \text{drop}} d\vec{r} F_l^{\text{coex}} - \int_{\text{drop}} d\vec{r} F_s^{\text{coex}} - \\ &\quad \mu_{n,\text{drop}}^{\text{coex}}(N - N_l - N_s) - \mu_{c,\text{drop}}^{\text{coex}}(C - C_l - C_s)). \end{aligned} \quad (4.18)$$

Here,  $F_s^{\text{coex}} = F_s(n_{s,\text{drop}}^{\text{coex}}, c_{s,\text{drop}}^{\text{coex}})$  is the solid free energy density of the coexisting solid (extractable from a solid unit cell with the average densities given by  $n_{s,\text{drop}}^{\text{coex}}$  and  $c_{s,\text{drop}}^{\text{coex}}$ ) and  $F_l^{\text{coex}} = F_l(n_{l,\text{drop}}^{\text{coex}}, c_{l,\text{drop}}^{\text{coex}})$  is the liquid free energy density (obtained by evaluation of Eq. (4.5) with the liquid coexisting densities). Capital  $N$ 's correspond to integrated densities, i.e.  $N = \int_{\text{box}} d\vec{r} n(\vec{r})$ ,  $N_l = n_{l,\text{drop}}^{\text{coex}}(A_{\text{box}} - A_{\text{drop}})$ ,  $N_s = n_{s,\text{drop}}^{\text{coex}} A_{\text{drop}}$ , and likewise for capital  $C$ 's. This interface free energy  $\mathcal{F}_I$  depends on the choice of radius  $r$  which enters in the extend of the drop domain and in the integrated densities. The particular choice of  $r$  with the condition

$$\mu_n(N_l + N_s - N) + \mu_c(C_l + C_s - C)|_{r=r_{\text{equim}}} = 0 \quad (4.19)$$

defines a generalized equimolar dividing surface. The equimolar dividing surface is known from one-component systems by the condition that the excess number of

particles relative to the thermodynamic bulk values in the drop and outside the drop adds up to zero. By considering only the density field  $n(\vec{r})$ , this condition reads:

$$\begin{aligned} 0 &= \int_{\text{box}} d\vec{r} (n(\vec{r}) - n_{s,\text{drop}}^{\text{coex}}) + \int_{\text{box} \setminus \text{drop}} d\vec{r} (n(\vec{r}) - n_{l,\text{drop}}^{\text{coex}}) \\ &= N - N_s - N_l. \end{aligned} \quad (4.20)$$

Thus the generalized condition for the equimolar dividing surface, given by Eq. (4.19), weighs the one-component condition with the values of the chemical potentials. By using  $r = r_{\text{equim}}$  defined by Eq. (4.19), the intuitive results state that the interface free energy is the total free energy minus the sum of bulk free energy of solid drop and liquid:

$$\begin{aligned} \mathcal{F}_{I,\text{equim}} &= \int_{\text{box}} d\vec{r} (F(n(\vec{r}), c(\vec{r}))) \\ &\quad - \int_{\text{drop}} d\vec{r} F_s - \int_{\text{box} \setminus \text{drop}} d\vec{r} F_l. \end{aligned} \quad (4.21)$$

This intuitive result only holds for the generalized equimolar surface defined by Eq. (4.19).

### 4.4.2 Interfacial energy based on numerical analysis

In the numerical analysis, a circular droplet is defined in the center of the simulation domain as initial configuration. Numerical simulations are performed for the following two cases:

- (1) A circular solid droplet surrounded by the liquid phase for solid fractions less than 50.
- (2) A circular liquid droplet surrounded by the solid phase for solid fractions greater than 50.

In order to reach the stable coexistence state, the initial values of  $n_0$  and  $c$  for the liquid and solid phases are chosen such that these values for the liquid phase correspond to the lower end point of the dashed line in Fig. 4.2, whereas, for the solid phase, these values correspond to a point on the dashed line continued into the solid region (these values are larger than the equilibrium coexistence values).

The average values of the densities  $\bar{c}$  and  $\bar{n}$  of the system are calculated from integration over the simulation box, i.e.

$$\bar{g} = \frac{1}{A_{\text{box}}} \int_{\text{box}} d\vec{r} g(\vec{r}). \quad (4.22)$$

The average values of the densities  $\bar{c}$  and  $\bar{n}$  depend on the initial parameters as

$$\begin{aligned} \bar{c} &= c_s^{\text{in}} P_s + c_l^{\text{in}} (1 - P_s), \\ \bar{n} &= n_s^{\text{in}} P_s + n_l^{\text{in}} (1 - P_s), \end{aligned} \quad (4.23)$$

and remain constant during the simulation run. Here,  $P_s \in [0, 1]$  is the solid fraction and  $P_l = 1 - P_s$  is the liquid fraction.

The equimolar solid/liquid fractions and the corresponding equimolar radius of the droplet are recalculated at the end of each simulation run until the stable state is reached (which indicates that the droplet is in equilibrium with the surrounding phase). The resulting solid phase fraction is calculated by using the condition expressed in Eq. (4.19), i.e.

$$P_{s,\text{equim}} = \frac{\mu_n^{\text{coex}}(\bar{n} - n_l^{\text{coex}}) + \mu_c^{\text{coex}}(\bar{c} - c_l^{\text{coex}})}{\mu_n^{\text{coex}}(n_s^{\text{coex}} - n_l^{\text{coex}}) + \mu_c^{\text{coex}}(c_s^{\text{coex}} - c_l^{\text{coex}})}. \quad (4.24)$$

The corresponding equimolar radius is calculated as

$$r_{\text{equim}} = \frac{\sqrt{A_{\text{box}} P_{s[l],\text{equim}}}}{\sqrt{\pi}} \quad (4.25)$$

for the solid and the liquid droplet, respectively. The equimolar excess energy density,  $F_{I,\text{equim}} = \mathcal{F}_{I,\text{equim}}/A_{\text{box}}$ , is evaluated from Eq. (4.21) by using the equimolar radius, i.e.

$$F_{I,\text{equim}} = \bar{F} - (F_s^{\text{coex}} P_{s,\text{equim}} + F_l^{\text{coex}} P_{l,\text{equim}}) \quad (4.26)$$

where  $\bar{F}$  is the average free energy density of the system. The corresponding interfacial energy per unit length for the equimolar excess energy defined in Eq. (4.26), is calculated as

$$f_{I,\text{equim}}(r) = \frac{\mathcal{F}_{I,\text{equim}}}{2\pi r_{\text{equim}}}. \quad (4.27)$$

For a slab crystal configuration with two planar interfaces, the interfacial tension is calculated as

$$f_{I,\text{equim}}^{\text{slab}} = \frac{\mathcal{F}_{I,\text{equim}}}{2L_y}, \quad (4.28)$$

where  $L_y$  is the width of the simulation box.

### 4.5 Simulation parameters

The governing equations (4.7) and (4.8) are numerically solved in 2D on a domain of size  $L_x \times L_y$ . Taking into account the triangular crystal structure,  $L_x = La$  and  $L_y = \sqrt{3}/2La$  are defined as the length and the width of the domain, respectively.

The number of discretization points in one unit cell (with dimensions of  $a^2\sqrt{3}/2$ ) is chosen to be 9 for these simulations. Therefore, the discretization size used in these simulations is  $\Delta x = a/9$ . A forward Euler scheme is used for the time derivative with a sufficiently small time step of  $\Delta t = 0.0015$  to ensure the stability of the scheme. Periodic boundary conditions are used on all boundaries of the simulation box. The values of the model parameters used in these simulations are given in Table 4.1.

$B_0^l$	$B_2^l$	$B_0^s$	$R_0$	$R_1$	$t$	$v$	$\Gamma$	$w$	$\xi$	$u$	$\epsilon$
1.05	-1.8	1.0	1.0	0.0	0.6	1.0	0.0	0.008	0.0	4.0	1.1

**Table 4.1:** Values of the model parameters used in the simulations.

The initial values of  $n_0$  and  $c$  for the liquid and solid phases are given in Table 4.2. These initial values correspond to the lower end point of the dashed line (for the liquid phase) and point on the dashed line continued into the solid region of the isothermal phase diagram shown in Fig. 4.2.

$n_l^{in}$	$n_s^{in}$	$c_l^{in}$	$c_s^{in}$
-0.006	0.01505	0.10363	0.178066

**Table 4.2:** Initial values of  $n_0$  and  $c$  for the liquid and solid phases.

Typical initial states with respect to various values of solid fractions  $P_s$  are shown in Fig. 4.4.

## 4.6 Liquid-solid coexistence

The equilibrium properties of solid nuclei are analyzed by stabilizing the circular solid crystals of various radii in the surrounding liquid phase. The initial solid phase fraction value  $P_s$  is varied from 0 to 1 for each system size, i.e.  $L = 20$  unit cells, 30 unit cells ... 70 unit cells in order to study the effect of solid phase fractions  $P_s$  and the system size  $L$  on the final results. The dimensions of the simulation

#### 4 Investigating the equilibrium properties of the liquid-solid interface

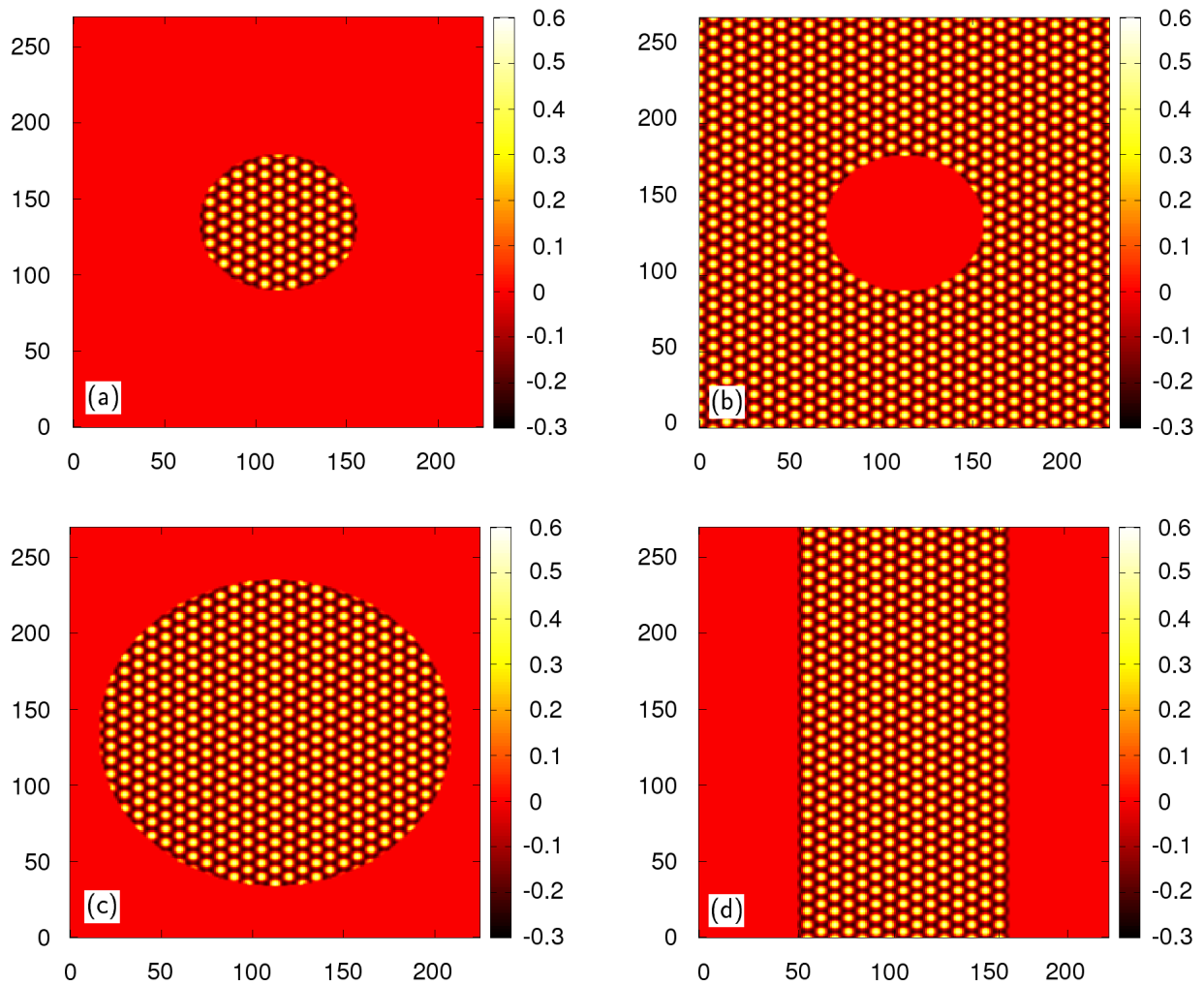


**Figure 4.4:** Typical initial states for the system size  $L = 30$  unit cells and (a)  $P_s = 0.1$ , (b)  $P_s = 0.9$ , (c)  $P_s = 0.5$  and (d)  $P_s = 0.5$  (slab configurations). The x-axis represents  $Lx/\Delta x$  whereas the y-axis represents  $Ly/\Delta y$ .

domain is chosen to be much larger compared to the lattice constant  $a$  in order to minimize the boundary effects on the simulation results. As an example, a typical crystal of the solid phase in equilibrium with the surrounding liquid phase, obtained from simulations performed with  $P_s = 0.2$  for  $L = 30$  unit cells, is depicted in Fig. 4.5.

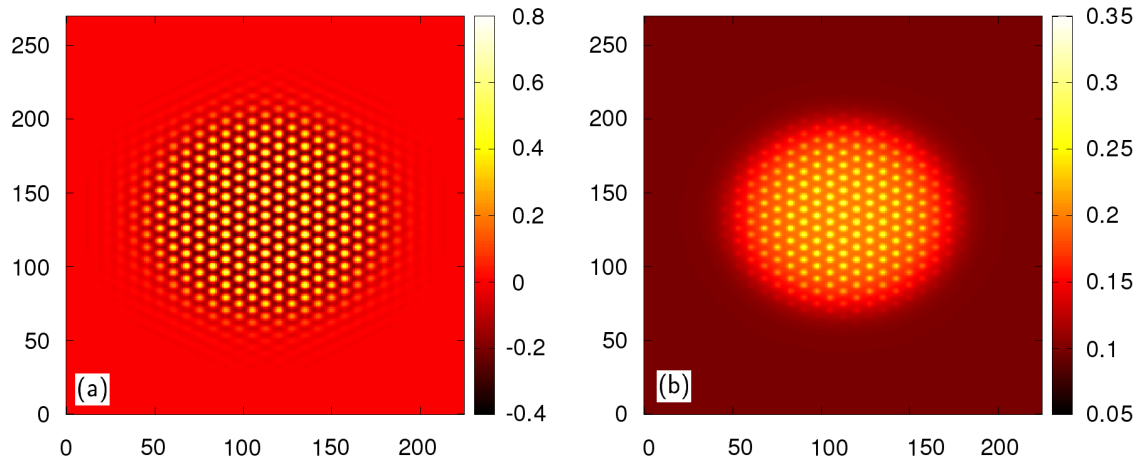


**Figure 4.5:** The resulting (a) atomic density field and (b) the concentration field of a stabilized solid crystal in the surrounding liquid phase obtained from the simulations performed with  $P_s = 0.2$  and  $L = 30$  unit cells. The x-axis represents  $Lx/\Delta x$  whereas the y-axis represents  $Ly/\Delta y$ . Figure already published in [12].

In order to analyze the equilibrium properties of a liquid droplet (a system with solid fractions more than 50 %), simulations are initialized by placing a liquid droplet in the simulation box. The liquid droplets of various radii are stabilized in the surrounding solid phase. An example of a typical liquid droplet in equilibrium with the surrounding solid phase, obtained from simulations performed with  $P_s = 0.8$  and  $L = 30$  unit cells, is shown in Fig. 4.6.

The precision of the chemical potentials ( $\mu_n$  and  $\mu_c$ ) for both phases at coexistence state is ensured up to the 8th digit after the decimal point. The resulting values of the chemical potentials ( $\mu_n$  and  $\mu_c$ ) for the liquid and solid phase at coexistence state for  $P_s = 0.2$  are given in Table 4.3. Such a precision is needed for further determination of the interface tension and the nucleation barriers.

## 4 Investigating the equilibrium properties of the liquid-solid interface

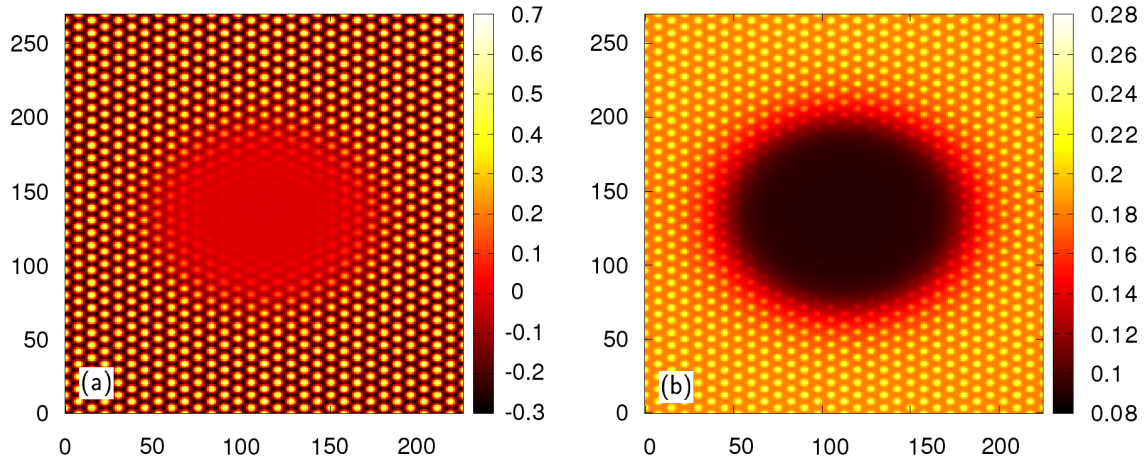


**Figure 4.6:** The resulting (a) atomic density field and (b) the concentration field of a stabilized liquid droplet in the surrounding solid phase obtained from the simulations performed with  $P_s = 0.8$  and  $L = 30$  unit cells. The x-axis represents  $Lx/\Delta x$  whereas the y-axis represents  $Ly/\Delta y$ . Figure already published in [12].

$\mu_{n,l}^{\text{coex}}$	$\mu_{n,s}^{\text{coex}}$	$\mu_{c,l}^{\text{coex}}$	$\mu_{c,s}^{\text{coex}}$
-0.007775424	-0.007775424	0.00440647	0.00440647

**Table 4.3:** Typical values of the chemical potentials ( $\mu_n$  and  $\mu_c$ ) for both phases at coexistence state with  $P_s = 0.2$ .

### 4.7 Influence of droplet size on the interfacial energy

The equimolar excess energy  $F_{L,\text{equim}}$  is calculated from Eq. (4.26) for the set of model parameters given in Table 4.1. The resulting equimolar excess free energy density and its areal density  $F_{L,\text{equim}}/(L_x L_y)$  is plotted as a function of the solid phase fraction in Fig. 4.7. For  $P_s \leq 0.5$  (solid droplet surrounded by the liquid phase) and fixed system size, the areal density of the excess free energy increases with increasing solid fraction because of the increase in the circumference of the droplet. For  $P_s > 0.5$  (liquid droplet surrounded by the solid phase), the situation is reverse, i.e. the circumference of the droplet as well as the excess free energy decrease with increasing solid fractions in the system. The simulation results also show that

## 4.7 Influence of droplet size on the interfacial energy

the equimolar excess free energy density curves obtained for different system sizes differs from each other, since the excess energy density is inversely proportional to  $\sqrt{A_{\text{box}}}$  (as follows from Eqs. (4.26) and (4.28)).

The results from numerical simulations also demonstrated that it is impossible to stabilize droplets with  $P_s > 0.1$  for system sizes smaller than 60 unit cells (here the droplet distance to the box boundaries becomes smaller than  $15a$ ), which may be due to the influence of the neighbouring droplets through the used periodic boundary conditions.

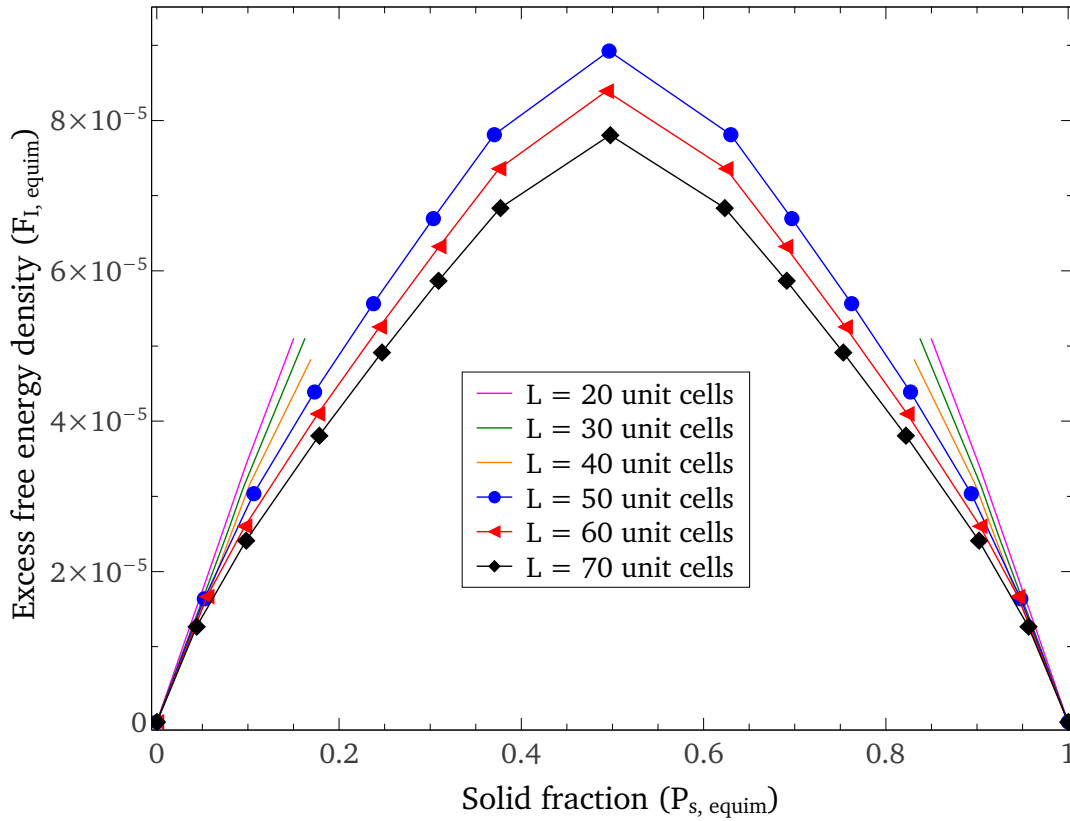


**Figure 4.7:** Equimolar excess free energy density ( $F_{I, \text{equim}}/A_{\text{box}}$ ) as a function of the solid fraction ( $P_{s, \text{equim}}$ ) for various system sizes. Figure already published in [12].

The scaling of the interfacial energy with the droplet radius and the independence on the system size can be better seen by considering the interface line tension  $f_{I, \text{equim}}$  which is calculated from the equimolar excess energy by using Eq. (4.28). The

## 4 Investigating the equilibrium properties of the liquid-solid interface

resulting equimolar interfacial tension as function of the equimolar droplet radius is plotted in Fig. 4.8.

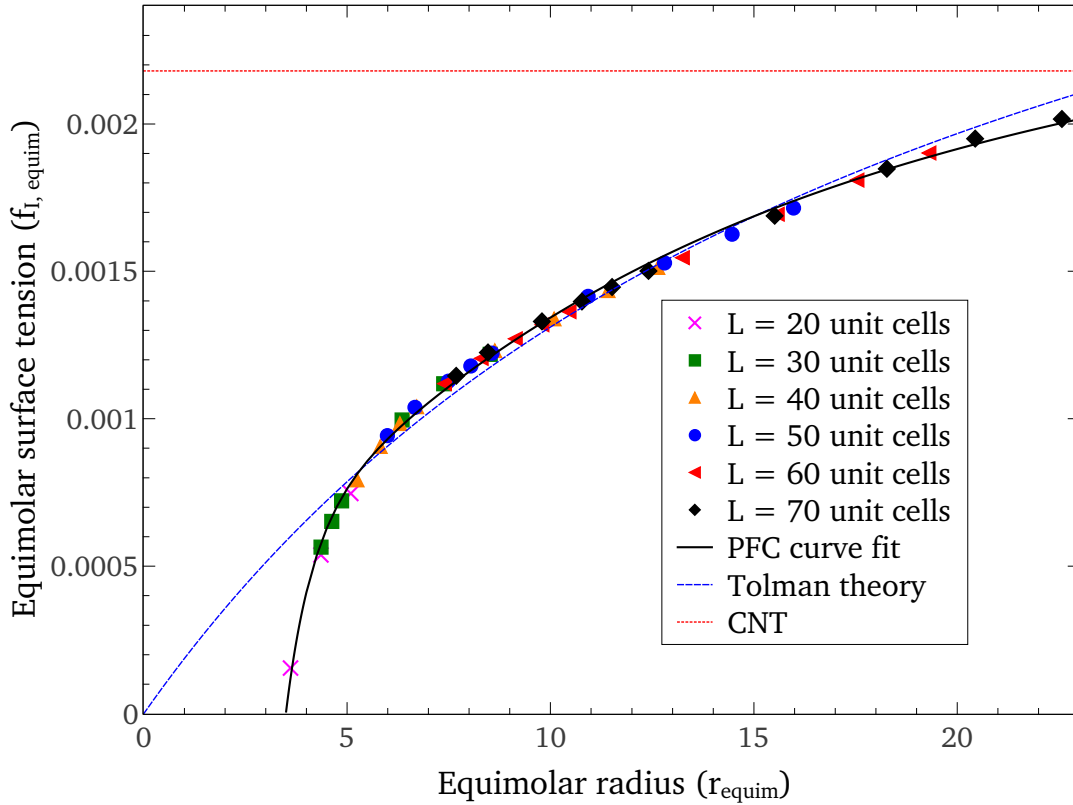


**Figure 4.8:** Equimolar interfacial line tension ( $f_{I, \text{equim}}$ ) as a function of the equimolar radius of the droplet ( $r_{\text{equim}}$ ) obtained from simulation performed for various system sizes. The dotted line is the interface tension for the slab configuration. Figure already published in [12].

The simulation results for  $f_{I, \text{equim}}$  approximately follow a master curve which demonstrates the possibility to extract droplet interface tensions by deliberately using finite system size approach. For the investigated model, the equimolar interface tension shows a steep rise for  $r_{\text{equim}}/a > 3$  and smoothly reaches the value of the slab interface tension (for  $L = 70$  unit cells) which is calculated as  $f_{I, \text{equim}}^{\text{slab}} = 0.00217978$ . This slab tension value is indicated by a dotted red line in Fig. 4.8.

### Comparison of simulation results with CNT and non-classical theories

The behavior of the interfacial line tension curves obtained from the simulations can be compared with CNT (shown as a constant value  $f_I^{\text{slab}}$  independent of  $r_{\text{equim}}$ ) as well as to the well-established non-classical Tolman theory which describes the dependence of the interfacial tension on the radius through curvature expansions (originally developed for liquid droplets in vapor in three dimensions) [90]. The expression which describes the dependence of the interfacial energy on the equimolar radius of the droplet obtained from the simulation results (through curve fitting), is approximated as:

$$f_{I,\text{equim}} = \gamma_{\infty} \left( 1 - \frac{\delta_P}{r} + \frac{1}{A_1} \left[ \frac{\delta_P}{r} \right]^2 - \frac{1}{A_2} \left[ \frac{\delta_P}{r} \right]^3 \right), \quad (4.29)$$

where  $r$  is the equimolar radius ( $r_{\text{equim}}$ ) and the values of the other fitting parameters used in the above expression as well as the correlation coefficients are given in Table 4.4.

$\delta_P$	$A_1$	$A_2$	$\gamma_{\infty}$ (PFC)	Corr. Coeff.
1.19 $a$	1.84150	8.6246	0.002901	0.99952

**Table 4.4:** Values of the fitting parameters for the resulting expression of interfacial energy obtained from PFC based simulations.

The fit of the master curve obtained from simulations, i.e. Eq. (4.29), and the equations based on Tolman's theory, i.e. Eq. (4.1), is shown in Fig. 4.8. The parameters of the Tolman formula, i.e.  $\delta_T$  and  $\gamma_{\infty}$  are estimated from the fits as  $2.7604a$  and  $0.003930$ , respectively. The interfacial tension values obtained for the Tolman formula are indicated by dotted blue lines in Fig. 4.8.

The comparison of simulation results with the Tolman formula illustrated in Fig. 4.8 shows that the Tolman formula [102] fit very well with the simulation results but only for a certain range of droplet radius and it could not explain the behaviour of interfacial energy for the smaller range of droplet radius. This comparison clearly

demonstrates that the numerical PFC results can not be fully described with the non-classical curvature expansion based on the non-classical Tolman formula. The difference allows for further realization of physical interpretation and it still needs to be investigated more closely with more experiments and DDFt.

### 4.8 Calculation of the grand potential difference

In addition to the radial dependence of the interfacial tension, the grand potential difference  $\Delta\Omega$  (nucleation barrier) is also calculated by using the procedure discussed in section 4.7. This grand potential difference can be written as a sum of bulk and surface contributions:

$$\Delta\Omega = \Delta\Omega_{\text{drop}}^{\text{equim}} + 2\pi r_{\text{equim}} f_{I,\text{equim}}, \quad (4.30)$$

where  $\Delta\Omega_{\text{drop}}^{\text{equim}} = \pi r_{\text{equim}}^2 \Delta\omega_{\text{drop}}$  with  $\Delta\omega_{\text{drop}}$  being the difference in the grand potential density of solid and liquid phases at (droplet) coexistence. The resulting values of  $\Delta\Omega$  as a function of the equimolar radius are plotted in Fig. 4.9.

The resulting nucleation barriers obtained from the simulations are also compared with the nucleation barrier based on the CNT ( $\Delta\Omega_{\text{CNT}}$ ), i.e.

$$\Delta\Omega_{\text{CNT}} = \pi r_{\text{equim}} f_{I,\text{equim}}^{\text{slab}}. \quad (4.31)$$

The above expression is derived from Eq. (4.30) by the capillary condition  $\Delta p = f_{I,\text{equim}}^{\text{slab}}/r_{\text{equim}}$ , where  $\Delta p = -\Delta\omega_{\text{drop}}$  is a pressure difference between interior and exterior of the droplet.

It can be seen in Fig. 4.9 that the resulting values of  $\Delta\Omega$  lies below  $\Delta\Omega_{\text{CNT}}$ . The difference between the  $\Delta\Omega$  and  $\Delta\Omega_{\text{CNT}}$  values is partly due to the droplet interfacial tension (for small radii) being smaller than the slab tension. The second reason is the dependence of pressure difference  $\Delta\omega_{\text{drop}}$  on the nucleus radius. Fig. 4.9 also

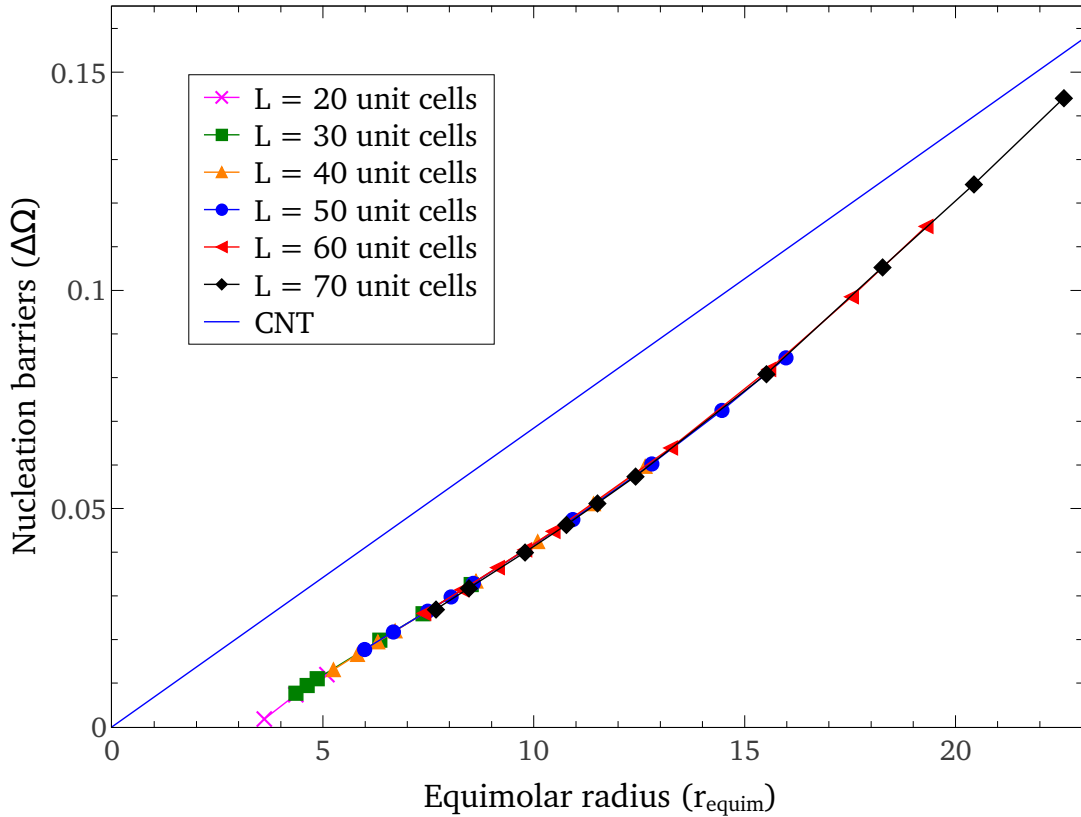


**Figure 4.9:** The difference in grand potential (nucleation barrier)  $\Delta\Omega$  as a function of the equimolar radius  $r_{\text{equim}}$  calculated from the numerical simulations for various system sizes and the predictions based on CNT ( $\Delta\Omega_{\text{CNT}}$ ). Figure already published in [12].

demonstrates that the nucleation barrier results for various system sizes fall on a master curve and thus provides a consistency validation.

## 4.9 Discussion

In this chapter, a precise assessment of the equilibrium properties of the curved liquid-solid interface as well as the nucleation barriers by means of the PFC method for a binary system is presented. The phase diagram of the model is further extended and a full phase diagram in  $n$ - $c$  space is developed by validating the PFC simulation results in close comparison with the results obtained from the mode ex-

pansion technique. Furthermore, the critical liquid and solid nuclei (droplets) were investigated in a PFC model for a binary system in two dimensions. In an infinite system, such critical nuclei correspond to metastable states (saddle points) in the free energy landscape. Instead of a numerical search for these saddle points, the idea of stabilizing critical droplets in finite systems was employed. In general, the simulation results demonstrate the usefulness of the finite system size approach to extract droplet size-dependent interface tensions and nucleation barriers also for liquid-solid phase transitions. The approximate independence of these quantities on the system size was exemplified by the simulation results. The calculation of droplet interface tensions requires the specification of a dividing interface (the droplet radius). A natural extension of the well-known equimolar surface definition for one-component systems was used in these simulations, which however requires the knowledge of the species chemical potentials under droplet equilibrium conditions. The simulation results demonstrated that the dependence of the interface tension on the generalized equimolar radius can not be fully described with the CNT and non-classical Tolman formula. Even though the PFC model is computationally much more accessible and an attractive alternative to the still more demanding non-local DFT calculations for crystals, the equilibration of the droplet solutions is occasionally slow. However, as demonstrated here in conjunction with PFC simulations, the finite system size technique certainly has prospective to assess also more sophisticated systems with perhaps a richer composition or variety of shapes of critical nuclei.

## 5 Summary

The purpose of this dissertation was the development of a more comprehensive understanding of the kinetics associated with the nucleation and successive initial microstructure evolution phenomena through a combination of theoretical model development and the application of these models to explore characteristic material's morphological features. Although the PFC method, introduced only a decade ago, has already proven itself as an attractive computational alternative to model various crystal growth phenomena, several important issues about the model's conceptual frame, remain unsolved from both theoretical and practical perspectives. In this work, some of these issues concerning the applicability limitation as well as the computational efficiency of the PFC model were addressed.

### Summary

The applicability of the originally introduced PFC model [7] is limited to model materials with Poisson's ratio of  $1/3$ , as discussed in chapter 2. To overcome this limitation and in order to extend the applicability of the PFC approach to a wider class of material systems, a more generalized theoretical model (APFC model) within the framework of the PFC method was developed (chapter 3). The APFC model has the capability of simulating isotropic as well as anisotropic crystal lattice systems of arbitrary Poisson's ratio [8]. The parameters of the APFC model were derived from DDFT which provided the physical justification for the model. The anisotropy in the system was quantified through specific model parameters and the theoretical derivation of the elastic constants in terms of the model parameters demonstrated that the parameters of the APFC model can be adjusted to match the given system in order to establish the connection with the real material systems [9]. The features

of the stable state phases of the APFC model were investigated through numerical simulations and the resulting morphologies were further analysed with respect to their characteristic morphological features. The simulation results of the stable state phases were summarized in form of a phase diagram of the model.

Apart from the above mentioned limitation, the use of the PFC method is quite often limited to certain applications because the periodic field of the PFC model demands higher computational resources, since it needs 8 – 10 spacial grid points per atomic spacing. Several new algorithms were developed to address these computational efficiency issues [42, 43]. In order to address the numerical efficiency issues and to establish a link with the standard PF models, the amplitude formulation for the APFC model was derived (chapter 3). The simulations performed with the resulting complex amplitude evolution equations maintained many of the salient features from the microscopic theory. In particular, the connection between the amplitude evolution equations and the standard PF models (with elasticity) is established which bridges the PF and PFC approaches for anisotropic crystals [10]. Sample simulations of these amplitude equations demonstrated that this simple model can effectively model solidification of isotropic as well as anisotropic with relatively much higher computational efficiency.

The dissertation is finished by going a step further and switching the focus from material systems with arbitrary Poisson's ratio to nucleation mechanisms associated with binary systems which certainly have higher industrial relevance (chapter 4). More specifically, a PFC model for binary alloys [1] was used to investigate the liquid-solid surface tensions of critical nuclei and nucleation barriers using finite system size approach [11, 12]. For these investigations, an extended phase diagram was developed based on the binary PFC model. Critical liquid and solid nuclei (droplets) were stabilized in finite systems of various sizes, however, the calculated interface tension as function of the nucleus radius was found to be independent of the system size. The natural extension of the well-known equimolar surface definition was used to specify the dividing interface (the droplet radius). The simulation results demonstrated that the nucleus size dependence of the liquid-solid interface tension as well as of the nucleation barrier can not be fully described with the CNT and non-classical Tolman formula. Therefore, a new phenomenological expression (based on the simulation

---

results) was introduced in chapter 4 to describe the dependence of the liquid-solid interface tension on the nucleus radius. Moreover, these investigations established the usefulness of the finite box size approach to study the droplet size-independent interface tensions and nucleation barriers for the liquid-solid transition as well as to address the problem of defining droplet radii in a two-component mixture, as it was successfully demonstrated as a quantitative route in MC simulations [88, 89, 90] as well as in DFT [89, 90] to study the liquid-vapor system.

### **Future outlook**

The research work presented in this dissertation contributed to the development of a better understanding of the nucleation kinetics as well as the initial microstructure formation from basic physics perspectives which includes model development, extension of existing model and the application of these models to study important physical phenomena which resulted in new scaling relations and the interpretation of these relations in close interaction with the existing theories. Despite all these advances, still a wide range of avenues remain which need further investigations and relevant model extensions. The following are only some selected issues of the many possible directions of future research.

The APFC model, which has been developed to model material systems with arbitrary Poisson's ratio, can be extended to a three-dimensional model in order to explore more features of the model. The APFC model can also be further extended in the direction of a two component model for binary mixtures. This extension would bring many more practical applications within the range of the model such as phase transformation, grain growth in anisotropic systems with multiple crystal orientations. A closer calibration of the APFC model to the colloids used in experiments would be desirable to facilitate an exact matching of numerical results with the experimental findings. This experimental comparison can also provide ways to test different boundary interaction conditions which leads to derive a theory for a consistent boundary condition formulation describing wetting angles, which is still an open issue as discussed in more detail in [60].

## 5 Summary

---

Furthermore, the finite size technique, which has been successfully established for liquid-solid systems, can be applied to solid-solid systems in order to investigate the equilibrium properties of the solid-solid phase transition (a process for which an accurate quantitative description is still lacking in the PFC formalism). The model used to perform simulation in chapter 4 has been chosen due to its potential for future investigations, i.e. besides a liquid-solid transition its phase diagram has an eutectic point and thus it can also be used to investigate the solid-solid phase transition. The finite system size technique can be further used for the extraction of properties of critical nuclei in more sophisticated density functional models or in other systems with perhaps a richer composition or variety of shapes of critical nuclei. With respect to specific material science phenomenon where atomic and microscale are tightly coupled, PFC is lately discussed as good candidate to explore details of grain boundary dynamics.

Overall, this research has set a stage for a wide range of relevant and interesting future studies that will support the development of a better understanding of these complex physical phenomena.

## 6 Zusammenfassung

Die vorliegende Arbeit soll einen Beitrag für die Erschließung eines umfassenderen Verständnisses der Kinetik leisten, welche mit der Keimbildung und den anschließenden anfänglichen Mikrostrukturentwicklungsphänomenen verbunden ist. Dabei werden die charakteristischen morphologischen Besonderheiten durch die Kombination von Entwicklung und Anwendung theoretischer Modelle erläutert. Obwohl sich das PFC-Modell, welches erst vor 10 Jahren eingeführt wurde, bereits als eine attraktive computertechnische Alternative für die Modellierung verschiedener Kristallwachstumsphänomene bewährt hat, bleiben hinsichtlich des Modells verschiedene wichtige Punkte, die die theoretischen als auch die praktischen Perspektiven betreffen, ungelöst. In dieser Arbeit werden einige dieser Punkte in Bezug auf die Anwendungsgrenzen des PFC-Modells sowie die Rechneffizienz angegangen.

### Zusammenfassung

Die Anwendbarkeit des ursprünglich entwickelten PFC-Modells [7] ist, wie in Kapitel 2 erläutert, auf die Modellierung von Werkstoffen mit einer Poissonzahl von  $1/3$  begrenzt. Um diese Anwendungsgrenze zu überwinden und die Anwendbarkeit der PFC-Methode auf eine breite Klasse von Materialsystemen zu erweitern, wurde ein allgemeineres theoretisches Modell (APFC-Modell) im Rahmen der PFC-Methode entwickelt (Kapitel 3). Mittels des APFC-Modells können isotropische als auch anisotropische Materialien mit unterschiedlichen Poissonzahlen simuliert werden [8]. Die Parameter des APFC-Modells wurden von der DDFT abgeleitet, welche die theoretische Begründung für das Modell lieferte. Die Anisotropie im System wurde durch spezifische Modellparameter quantifiziert. Darüber hinaus zeigte auch die theoretische Herleitung der elastischen Konstanten in Bezug auf die Modellparameter,

dass die Poissonzahl als Funktionen der Anisotropieparameter ist [9]. Die einzigartigen Charakteristika der stabilen Zustandsphasen wurden mittels numerischer Simulationen untersucht und die daraus resultierenden Morphologien wurden weiter in Bezug auf ihre charakteristischen morphologischen Eigenschaften analysiert. Die Simulationsergebnisse der stabilen Zustandsphasen wurden in Form eines Phasendiagramms des Modells zusammengefasst.

Abgesehen von den bereits erwähnten Grenzen ist die Verwendung der PFC-Methode ziemlich oft limitiert, da die periodische Struktur des PFC-Modells höhere Rechnerressourcen aufgrund der notwendigen 8-10 räumlichen Gitterpunkte pro Atomzwischenraum erfordert. Verschiedene neue Algorithmen wurden entwickelt, um dieses Problem der Computereffizienz anzugehen [42, 43]. Um das Thema der numerischen Effizienz zu bewältigen und um eine Verbindung zum Standard-PF-Modell herzustellen, wurde die Amplitudenformulierung für das APFC-Modell entwickelt (Kapitel 3). Die Simulationen, welche mit der resultierenden komplexen Amplituden-Evolutionsgleichung durchgeführt wurden, enthalten viele der hervorstehenden Merkmale aus der eher mikroskopischen Theorie. Insbesondere wird die Verbindung zwischen den Amplitudengleichungen und dem Standard-PF-Modell mit Elastizität hergestellt, was eine Brücke zwischen der PF- und der PFC-Methode für anisotropische Kristalle schlägt [10]. Beispielsimulationen dieser Amplitudengleichungen demonstrierten, dass dieses einfache Modell effektiv die Erstarrung von anisotropischen Kristallen mit relativ hoher Rechereffizienz modellieren kann.

Den Abschluss der Arbeit bildet eine quantitative Studie der Keimbildungskinetik in Verbindung mit flüssig-fest Grenzflächen für binäre Legierungen (Kapitel 4). Hier wurde ein PFC-Modell für binäre Legierungen verwendet [1], um die flüssig-fest-Oberflächenspannung eines kritischen Keims und die Keimbildungsbarrieren mit Hilfe einer Methode von finiten Systemgrößen zu untersuchen [11, 12]. Für diese Untersuchungen verwendete PFC-Modell wurde ein Phasendiagramm entwickelt. Kritische flüssige und feste Keime (Droplets) wurden in finiten Systemen verschiedener Größe stabilisiert, jedoch konnte ermittelt werden, dass die berechnete Oberflächenspannung als Funktion des Keimradius unabhängig von der Systemgröße ist. Die normale Erweiterung der bekannten equimolaren Oberflächendefinition wurde für die Spezifizierung der trennenden Grenzfläche (Dropletradius)

---

verwendet. Die Simulationsergebnisse zeigten, dass die Keimgrößenabhängigkeit der flüssig-fest-Oberflächenspannung als auch die Keimbildungsbarriere nicht vollständig mit Hilfe der CNT und der nichtklassischen Tolman-Formel beschrieben werden kann. Daher wurde in Kapitel 4 ein neuer phänomenologischer Ausdruck eingeführt, der die Abhängigkeit der flüssig-fest-Grenzflächenspannung vom Keimradius beschreibt. Darüber hinaus begründen diese Untersuchungen den Nutzen der "Finite-Box-Size- Methode" für die Untersuchung der größenunabhängigen Droplet-Grenzflächenspannung sowie der Keimbildungsbarrieren für den flüssig-fest-Übergang und spricht außerdem das Problem der Definition der Droplet-Radien in einer Zweikomponentenmischung an. Dies wurde bereits erfolgreich mit Hilfe einer quantitativen Methode in MC-Simulationen [88, 89, 90] als auch in der DFT [89, 90] für die Untersuchung des flüssig-Gas-Systems demonstriert.

## **Ausblick**

Die hier dargestellte Forschungsarbeit lieferte einen Beitrag zur Entwicklung eines besseren Verständnisses der Keimbildungskinetik als auch der anfänglichen Mikrostrukturentwicklung aus fundamentaler physikalischer Sicht. Sie schließt die Modellenentwicklung, die Weiterentwicklung vorhandener Modelle sowie die Anwendung dieser Modelle für die Untersuchung wichtiger physikalischer Phänomene ein, was in neuen Skalenrelationen sowie der Interpretation dieser Relationen in engen Zusammenspiel mit den bereits existierenden Theorien resultiert. Trotz all dieser Fortschritte bleibt eine große Auswahl an Möglichkeiten erhalten, welche weitere Untersuchungen und relevante Modellerweiterungen benötigen.

Das APFC-Modell, welches für die Modellierung von Werkstoffen mit unterschiedlichen Poissonzahlen entwickelt wurde, kann zu einem 3D-Modell erweitert werden, um mehr Charakteristika dieses Modells zu erforschen. Das APFC-Modell kann außerdem auch weiter in Richtung eines Zweikomponentenmodell für binäre Mischungen erweitert werden. Diese Erweiterung würde noch mehr praktische Anwendungen innerhalb der Grenzen des Modells nach sich ziehen, zum Beispiel Phasenumwandlungen oder Kornwachstum in anisotropen Systemen mit multiplen Kristallorientierungen. Eine engere Kalibrierung der APFC-Modells für Kolloide wie sie in Ex-

perimenten verwendet werden, wäre wünschenswert, um einen exakten Abgleich der numerischen Ergebnisse mit den experimentellen zu ermöglichen. Dieser experimentelle Vergleich kann auch Wege für den Test verschiedener Randbedingungen aufweisen, was zur Ableitung einer Theorie für eine konsistente Randbedingungsformulierung führen kann. Das stellt einen noch offenen Punkt dar, wie genauer in [60] erläutert.

Die Finite-Size-Methode, welche erfolgreich für flüssig-fest-Systeme eingeführt wurde, kann auf fest-fest-Systeme angewendet werden, um die Gleichgewichtseigenschaften des fest-fest-Phasenübergangs zu untersuchen (ein Prozess mit einer akuraten quantitativen Beschreibung fehlt im PFC-Formalismus noch). Das in Kapitel 4 verwendete Modell weist in Phasendiagramm, neben dem untersuchten flüssig-fest Übergang, zum Beispiel auch einem eutektischen Punkt auf. Damit eignet es sich ebenfalls für die weitere Erforschung von fest-fest Phasenübergängen. Die Finite-Size-Methode kann darüber hinaus für die Bestimmung der Eigenschaften eines kritischen Keimes in anspruchsvolleren Dichtefunktionalmodellen oder in anderen Systemen mit mehr Komponenten oder unterschiedlichen Formen des kritischen Keimes angewendet werden.

Insgesamt konnte mit der vorliegenden Arbeit eine Voraussetzung für eine breite Auswahl an relevanten und interessanten Untersuchungen geschaffen werden, welche die Entwicklung eines besseren Verständnisses dieser komplexen physikalischen Phänomene unterstützt.

## Bibliography

- [1] K. R. Elder, N. Provatas, J. Berry, P. Stefanovic and M. Grant. Phase-field crystal modeling and classical density functional theory of freezing. *Phys. Rev. B*, 75 (6):064107, 2007.
- [2] V. Vuorinen et al. *Interfacial compatibility in microelectronics: Moving away from the trial and error approach*, Springer, 2012.
- [3] L. Q. Chen. Phase-field models for microstructure evolution. *Annu. Rev. Mater. Res.*, 45 (10):7424, 1992.
- [4] W. J. Boettinger, J. A. Warren, C. Beckermann and A. Karma. Phase-field simulation of solidification. *Annu. Rev. Mater. Res.*, 32:163-194, 2002.
- [5] H. Emmerich. Modeling elastic effects in epitaxial growth. *Cont. Mech. Thermodyn.*, 15:197-215, 2003.
- [6] H. Emmerich, P. Virnau, G. Wilde and R. Spatschek. Heterogeneous nucleation and microstructure formation: Steps towards a system and scale bridging understanding. *Eur. Phys. J. Special Topics*, 223:337-346, 2014.
- [7] K. R. Elder, M. Katakowski, M. Haataja and M. Grant. Modeling elasticity in crystal growth. *Phys. Rev. Lett.*, 88:245701, 2002.
- [8] M. A. Choudhary, D. Li, H. Emmerich and H. Löwen. DDFT calibration and investigation of an anisotropic phase-field crystal model. *J. Phys.: Condens. Matter*, 23 (26):265005, 2011.
- [9] M. A. Choudhary, J. Kundin and H. Emmerich. Phase-field crystal modeling of anisotropic material systems of arbitrary Poisson's ratio. *Philos. Mag. Lett.*, 92 (9):451-458, 2012.
- [10] J. Kundin, M. A. Choudhary and H. Emmerich. Bridging the phase-field and phase-field crystal approaches for anisotropic material systems. *Eur. Phys. J. Special Topics*, 223:363-372, 2014.

- [11] M. A. Choudhary, J. Kundin and H. Emmerich. Numerical study of the liquid-solid interface properties for binary alloys using phase-field crystal approach. *MRS Proceedings*, 1535:mmm12-a, Cambridge University Press, 2013.
- [12] M. A. Choudhary, J. Kundin, M. Oettel and H. Emmerich. Solid-liquid surface tensions of critical nuclei and nucleation barriers from a phase-field-crystal study of a model binary alloy using finite system sizes. *Phys. Rev. E*, 90 (2):022403, 2014.
- [13] L. I. Rubinshtein. The Stefan problem. American mathematical society, USA, 1979.
- [14] V. L. Ginzburg and L. D. Landau. On the theory of superconductivity. *Zh. Eksp. Teor. Fiz.*, 20:1064, 1950.
- [15] J. W. Cahn and J. E. Hilliard. Free energy of a nonuniform system. 1. Interfacial energy. *J. Chem. Phys.*, 28:258, 1958.
- [16] G. Caginalp and W. Xie. Phase-field and sharp-interface alloy models. *Phys. Rev. E*, 48 (3):1897, 1993.
- [17] O. Penrose and P. C. Fife. Thermodynamically consistent models of phase-field type for the kinetic of phase transitions. *Physica D: Nonlinear Phenomena*, 43:44-62, 1990.
- [18] A. A. Wheeler, W. J. Boettinger and G. B. McFadden. Phase-field model for isothermal phase transitions in binary alloys. *Phys. Rev. A*, 45 (10):7424, 1992.
- [19] R. Kobayashi. Modeling and numerical simulations of dendritic crystal growth. *Physica D: Nonlinear Phenomena*, 63 (3):410-423, 1993.
- [20] A. Karma and W. J. Rappel. Phase-field method for computationally efficient modeling of solidification with arbitrary interface kinetics. *Phys. Rev. E*, 53 (4):R3017, 1996.
- [21] T. Ala-Nissila, S. Majaniemi and K. Elder. *Phase-field modeling of dynamical interface phenomena in fluids*, volume 640:357-388. Novel methods in soft matter simulations, Springer Berlin Heidelberg, 2004.
- [22] B. Böttger, J. Eiken and I. Steinbach. Phase field simulation of equiaxed solidification in technical alloys. *Acta materialia*, 54:2697-2704, 2006.
- [23] I. Steinbach. Phase-field models in materials science. *Modeling simul. Mater.*

- Sci. Eng.*, 17:073001, 2009.
- [24] M. Haataja and F. Leonard. Influence of mobile dislocations on phase separation in binary alloys. *Phys. Rev. B*, 69:081201, 2004.
- [25] J. Müller and M. Grant. Model of surface instabilities induced by stress. *Phys. Rev. Lett.*, 82:1736, 1999.
- [26] K. R. Elder and M. Grant. Modeling elastic and plastic deformations in nonequilibrium processing using phase field crystals. *Phys. Rev. E*, 70:051605, 2004.
- [27] P. M. Stefanovic, M. Haataja and N. Provatas. Phase-field crystals with elastic interactions. *Phys. Rev. Lett.*, 96:225504, 2006.
- [28] J. Berry, M. Grant and K. R. Elder. Diffusive atomistic dynamics of edge dislocations in two dimensions. *Phys. Rev. E*, 73 (3):031609, 2006.
- [29] K. Elder. Heterogenous nucleation Lecture Notes. *Summer School of DFG Priority Program*, 1296: 2008.
- [30] N. Provatas and K. Elder. *Phase-field methods in materials science and engineering*. John Wiley and Sons, 2011.
- [31] H. Emmerich. *The diffuse interface approach in materials science: thermodynamic concepts and applications of phase-field models.*, volume 73. Springer, 2003.
- [32] H. Emmerich. Advances of and by phase-field modelling in condensed-matter physics. *Adv. in Physics*, 57(1):1-87, 2008.
- [33] L. D. Landau and E. M. Lifshitz. *Statistical Physics*. Pergamon, Oxford, 1958.
- [34] J. Swift and P. C. Hohenberg. Hydrodynamic fluctuations at the convective instability. *Phys. Rev. A*, 15:319, 1977.
- [35] T. V. Ramakrishnan and M. Yussouff. First-principles order-parameter theory of freezing. *Phys. Rev. B*, 19:2775, 1979.
- [36] R. Evans. *Fundamentals of Inhomogeneous Fluids*. Marcel Dekker, New York, 1992.
- [37] Y. Singh. Density-functional theory of freezing and properties of the ordered phase. *Phys. Reports*, 207 (6):351-444, 1991.

- [38] K. A. Wu and A. Karma. Phase-field crystal modeling of equilibrium bcc-liquid interfaces. *Phys. Rev. B*, 76 (18):184107, 2007.
- [39] D. H. Yeon, Z. F. Huang, K. R. Elder, and K. Thornton. Density-amplitude formulation of the phase-field crystal model for two-phase coexistence in two and three dimensions. *Philos. Mag.*, 90:237-263, 2010.
- [40] R. Spatschek and A. Karma. Amplitude equations for polycrystalline materials with interaction between composition and stress. *Phys. Rev. B*, 81:214201, 2010.
- [41] K. R. Elder, Z. F. Huang and N. Provatas. Amplitude expansion of the binary phase-field-crystal model. *Phys. Rev. E*, 81 (1):011602, 2010.
- [42] R. Backofen, A. Rätz and A. Voigt. Nucleation and growth by a phase field crystal (PFC) model. *Philos. Mag. Lett.*, 87 (11):813-820, 2007.
- [43] M. Cheng and J. A. Warren. An efficient algorithm for solving the phase field crystal model. *J. Comput. Phys.*, 227 (12):6241-6248, 2008.
- [44] N. Goldenfeld, B. P. Athreya, and J. A. Dantzig. Renormalization group approach to multiscale modelling in materials science. *J. Stat. Phys.*, 125:1015-1023, 2006.
- [45] B. P. Athreya, N. Goldenfeld and J. A. Dantzig. Renormalization-group theory for the phase-field crystal equation. *Phys. Rev. E*, 74:011601, 2006.
- [46] B. P. Athreya, N. Goldenfeld, J. A. Dantzig, M. Greenwood and N. Provatas. Adaptive mesh computation of polycrystalline pattern formation using a renormalization-group reduction of the phase-field crystal model. *Phys. Rev. E*, 76 (5):056706, 2007.
- [47] R. Graham. Systematic Derivation of a Rotationally Covariant Extension of the Two-Dimensional Newell-Whitehead-Segel Equation. *Phys. Rev. Lett.* , 76:2185, 1996.
- [48] K. I. Matsuba and K. Nozaki. Comment on "Systematic Derivation of a Rotationally Covariant Extension of the Two-Dimensional Newell-Whitehead-Segel Equation". *Phys. Rev. Lett.* , 80:3886, 1996.
- [49] R. Graham. Erratum: Systematic Derivation of a Rotationally Covariant Extension of the Two-Dimensional Newell-Whitehead-Segel Equation. *Phys. Rev. Lett.* , 80:3888, 1996.

- 
- [50] P. Stefanovic, M. Haataja and N. Provatas. Phase field crystal study of deformation and plasticity in nanocrystalline materials. *Phys. Rev. E*, 80:046107, 2009.
- [51] S. van Teeffelen, R. Backofen, A. Voigt and H. Löwen. Derivation of the phase-field-crystal model for colloidal solidification. *Phys. Rev. E*, 79:051404, 2009.
- [52] G. Tegze, L. Granasy, G. I. Tóth, F. Podmaniczky, A. Jaatinen, T. Ala-Nissila and T. Pusztai. Diffusion-controlled anisotropic growth of stable and metastable crystal polymorphs in the phase-field crystal model. *Phys. Rev. Lett.*, 103:035702, 2009.
- [53] A. Jaatinen, C. V. Achim, K. R. Elder and T. Ala-Nissila. Thermodynamics of bcc metals in phase-field-crystal models. *Phys. Rev. E*, 80:031602, 2009.
- [54] Y. Yu, B. Liu and A. Voigt. Phase-field modeling of anomalous spiral step growth on Si (001) surface. *Phys. Rev. B*, 79:235317, 2009.
- [55] J. Mellenthin, A. Karma and M. Plapp. Phase-field crystal study of grain-boundary premelting. *Phys. Rev. B*, 78:184110, 2008.
- [56] I. M. McKenna, M. P. Gururajan and P. W. Voorhees. Phase field modeling of grain growth: effect of boundary thickness, triple junctions, misorientation, and anisotropy. *J. Mater. Sci.*, 44:2206-2217, 2009.
- [57] J. Berry and M. Grant. Modeling multiple time scales during glass formation with phase-field crystals. *Phys. Rev. Lett.*, 106:175702, 2011.
- [58] P. F. Tupper and M. Grant. Phase field crystals as a coarse-graining in time of molecular dynamics. *Europhys. Lett.*, 81:40007, 2008.
- [59] A. Jaatinen and T. Ala-Nissila. Extended phase diagram of the three-dimensional phase field crystal model. *J. Phys.: Condens. Matter*, 22(20):205402, 2010.
- [60] R. Prieler, J. Hubert, D. Li, B. Verleye, R. Haberkern and H. Emmerich. An anisotropic phase-field crystal model for heterogeneous nucleation of ellipsoidal colloids. *J. Phys.: Condensed Matter*, 21(46):464110, 2009.
- [61] K. E. Evans, M. A. Nkansah, I. J. Hutchinson and S. C. Rogers. Molecular network design. *Nature*, 353:124, 1991.
- [62] K. E. Evans, M. A. Nkansah and I. J. Hutchinson. Auxetic foams: modelling

- negative Poisson's ratios. *Acta Metall. Mater.*, 42 (4):1289-1294, 1994.
- [63] G. W. Milton. Composite materials with Poisson's ratios close to -1. *J. Mech. Phys. Solids*, 40 (5):1105-1137, 1992.
- [64] D. A. Konyok, Y. M. Pleskachevsky and S. V. Shilko. Materials with negative Poisson's ratio. *Mech. Compos. Mater. Construct.*, 10 (1):35-69, 2004.
- [65] T. Li, J. W. Morris, N. Nagasako, S. Kuramoto, and D. C. Chrzan. Ideal Engineering Alloys. *Phys. Rev. Lett.*, 98 (10):105503, 2007.
- [66] R. Evans. The nature of the liquid-vapour interface and other topics in the statistical mechanics of non-uniform, classical fluids. *Adv. Phys.*, 28 (2):143-200, 1979.
- [67] H. Löwen. Melting, freezing and colloidal suspensions. *Phys. Reports*, 237 (5):249-324, 1994.
- [68] H. Löwen. Density functional theory of inhomogeneous classical fluids: recent developments and new perspectives. *J. Phys.: Condens. Matter*, 14 (46):11897, 2002.
- [69] A. M. Bohle, R. Holyst and T. Vilgis. Polydispersity and ordered phases in solutions of rodlike macromolecules. *Phys. Rev. Lett.*, 76 (8):1396, 1996.
- [70] H. Löwen. Interaction between charged rodlike colloidal particles. *Phys. Rev. Lett.*, 72 (3):424, 1994.
- [71] H. Löwen. Charged rodlike colloidal suspensions: An ab initio approach. *J. Chem. Phys.*, 100:6738, 1994.
- [72] S. Prestipino and F. Saija. Phase diagram of Gaussian-core nematics. *J. Chem. Phys.*, 126 (19):194902, 2007.
- [73] D. van der Beek, P. Davidson, H. H. Wensink, G. J. Vroege and H. N. W. Lekkerkerker. Influence of a magnetic field on the nematic phase of hard colloidal platelets. *Phys. Rev. E*, 77:031708, 2008.
- [74] V. N. Manoharan, M. T. Elsesser and D. J. Pine. Dense packing and symmetry in small clusters of microspheres. *Science*, 301:483-487, 2003.
- [75] E. Bianchi, J. Largo, P. Tartaglia, E. Zaccarelli and F. Sciortino. Phase diagram of patchy colloids: towards empty liquids. *Phys. Rev. Lett.*, 97 (16):168301,

- 2006.
- [76] E. Allahyarov, H. Löwen, A. A. Louis and J. P. Hansen. Discrete charge patterns, Coulomb correlations and interactions in protein solutions. *Europhys. Lett.*, 57:731, 2002.
- [77] E. Allahyarov, H. Löwen, J. P. Hansen and A. A. Louis. Nonmonotonic variation with salt concentration of the second virial coefficient in protein solutions. *Phys. Rev. E*, 67:051404, 2003.
- [78] M. Rex, H. H. Wensink and H. Löwen. Dynamical density functional theory for anisotropic colloidal particles. *Phys. Rev. E*, 76:021403, 2007.
- [79] M. M. Tirado, C. L. Martinez and J. G. de la Torre. Comparison of theories for the translational and rotational diffusion coefficients of rod-like macromolecules: Application to short DNA fragments. *J. Chem. Phys.*, 81:2047, 1984.
- [80] H. Löwen. Brownian dynamics of hard spherocylinders. *Phys. Rev. E*, 50(2):1232, 1994.
- [81] A. B. Fontecha, H. J. Schöpe, H. König, T. Palberg, R. Messina and H. Löwen. A comparative study on the phase behaviour of highly charged colloidal spheres in a confining wedge geometry. *J. Phys.: Condens. Matter*, 17:S2779-S2786, 2005.
- [82] H. J. Schöpe, A. B. Fontecha, H. König, J. M. Hueso and R. Biehl. Fast Microscopic Method for Large Scale Determination of Structure, Morphology, and Quality of Thin Colloidal Crystals. *Langmuir*, 22:1828-1838, 2006.
- [83] M. C. Cross and P. C. Hohenberg. Pattern formation outside of equilibrium. *Rev. Mod. Phys.*, 65(3):851, 1993.
- [84] N. Zhou, C. Shen, M. J. Mills and Y. Wang. Large-scale three-dimensional phase field simulation of gamma-rafting and creep deformation. *Philos. Mag.*, 90:405, 2010.
- [85] R. Spatschek, E. Brener and A. Karma. Phase field modeling of crack propagation. *Philos. Mag.*, 91:75, 2011.
- [86] U. O. M. Vázquez, W. Shinoda, P. B. Moore, C. C. Chiu and S. O. Nielsen. Calculating the surface tension between a flat solid and a liquid: a theoretical and computer simulation study of three topologically different methods. *J. Math. Chem.*, 45(1):161-174, 2009.

- [87] Y. Lin, H. Skaff, T. Emrick, A. D. Dinsmore and T. P. Russell. Calculating the surface tension between a flat solid and a liquid: a theoretical and computer simulation study of three topologically different methods. *Science*, 299:226-229, 2003.
- [88] A. Tröster and K. Binder. Positive Tolman Length in a Lattice Gas with Three-Body Interactions. *Phys. Rev. Lett.*, 107:265701, 2011.
- [89] B. J. Block, S. K. Das, M. Oettel, P. Virnau and K. Binder. Curvature dependence of surface free energy of liquid drops and bubbles: A simulation study. *J. Chem. Phys.*, 133:154702, 2010.
- [90] A. Tröster, M. Oettel, B. Block, P. Virnau and K. Binder. Numerical approaches to determine the interface tension of curved interfaces from free energy calculations. *J. Chem. Phys.*, 136:064709, 2012.
- [91] M. Schrader, P. Virnau and K. Binder. Simulation of vapor-liquid coexistence in finite volumes: A method to compute the surface free energy of droplets. *Phys. Rev. E*, 79:061104, 2009.
- [92] M. Fevre, C. Varvenne, A. Fine and Y. Le Bouar. Influence of atomic size mismatch on binary alloy phase diagrams. *Phil. Mag.*, 93:1563, 2013.
- [93] S. L. Grishick and C. P. Chiu. Kinetic nucleation theory: A new expression for the rate of homogeneous nucleation from an ideal supersaturated vapor. *J. Chem. Phys.*, 93:1273, 1990.
- [94] Z. Kozisek. Influence of the Curvature Dependence of Interfacial Energy on Homogeneous Nucleation Kinetics. *Cryst. Res. Technol.*, 26:3-10, 1991.
- [95] P. Harrowell and D. W. Oxtoby. A molecular theory of crystal nucleation from the melt. *J. Chem. Phys.*, 80:1639, 1984.
- [96] M. Yussouff. Generalized structural theory of freezing. *Phys. Rev. B*, 23:5871, 1981.
- [97] C. K. Bagdassarian and D. W. Oxtoby. Crystal nucleation and growth from the undercooled liquid: A nonclassical piecewise parabolic free-energy model. *J. Chem. Phys.*, 100:2139, 1994.
- [98] L. Granasy. Diffuse interface approach to crystal nucleation. *Mater. Sci. Forum*, 215:451-458, 1996.

- 
- [99] L. Granasy, T. Pusztai, E. Hartmann. Diffuse interface model of nucleation. *J. Cryst. Growth*, 167:756-765, 1996.
- [100] L. Granasy and F. Igloi. Comparison of experiments and modern theories of crystal nucleation. *J. Chem. Phys.*, 107:3634, 1997.
- [101] V. M. Fokin and E. D. Zanotto. Crystal nucleation in silicate glasses: the temperature and size dependence of crystal/liquid surface energy. *J. Non-Crystalline Solid*, 265:105-112, 2000.
- [102] R. C. Tolman. The effect of droplet size on surface tension. *J. Chem. Phys.*, 17:333, 1949.
- [103] M. J. Haye and C. Bruin. Molecular dynamics study of the curvature correction to the surface tension. *J. Chem. Phys.*, 100:556, 1994.
- [104] V. Talanquer and D. W. Oxtoby. Density functional analysis of phenomenological theories of gas-liquid nucleation. *J. Chem. Phys.*, 99 (9):2865-2874, 1995.
- [105] M. A. Anisimov. Divergence of Tolman's length for a droplet near the critical point. *Phys. Rev. Lett.*, 98:035702, 2007.
- [106] G. I. Tóth and L. Granasy. Phase field theory of interfaces and crystal nucleation in a eutectic system of fcc structure: I. Transitions in the one-phase liquid region. *J. Chem. Phys.*, 127:074709, 2007.
- [107] S. Auer and D. Frenkel. Quantitative prediction of crystal-nucleation rates for spherical colloids: A computational approach. *Annu. Rev. Phys. Chem.*, 55:333-361, 2004.
- [108] J. Bokeloh, R. E. Rozas, J. Horbach and G. Wilde. Nucleation barriers for the liquid-to-crystal transition in Ni: experiment and simulation. *Phys. Rev. Lett.*, 107:145701, 2011.
- [109] K. Lichtner, A. J. Archer and S. H. L. Klapp. Phase separation dynamics in a two-dimensional magnetic mixture. *J. Chem. Phys.*, 136:024502, 2012.
- [110] R. Backofen and A. Voigt. A phase-field-crystal approach to critical nuclei. *J. Phys.: Condens. Matter*, 22:364104, 2010.
- [111] G. I. Tóth, G. Tegze, T. Pusztai and L. Granasy. Heterogeneous crystal nucleation: The effect of lattice mismatch. *Phys. Rev. Lett.*, 108:025502, 2012.

## Bibliography

---

- [112] R. Backofen and A. Voigt. A phase field crystal study of heterogeneous nucleation - application of the string method. *Eur. Phys. J. Special Topics*, 223:337, 2014.
- [113] W. H. Press, B. P. Flannery, S. A. Teukolsky and W. T. Vetterling. Numerical Recipes (Fortran Version). *Cambridge University Press, Cambridge*, 1989.

# List of Publications

## Articles

M. A. Choudhary, D. Li, H. Emmerich and H. Löwen  
DDFT calibration and investigation of an anisotropic phase-field crystal model  
*J. Phys.: Condens. Matter* **23**, 265005 (2011).

M. A. Choudhary, J. Kundin, and H. Emmerich  
Phase-field crystal modeling of anisotropic material systems of arbitrary Poisson's ratio  
*Phil. Mag. Lett.* **92** (9), 451-458 (2012).

J. Kundin, R. Kumar, A. Schlieter, M. A. Choudhary, T. Gemming, U. Kühn and H. Emmerich  
Phase-field modeling of eutectic Ti-Fe alloy solidification  
*Comp. Mater. Sci.* **63**, 319-328 (2012).

M. A. Choudhary, J. Kundin and H. Emmerich  
Numerical study of the liquid-solid interface properties for binary alloys using phase-field crystal approach  
*MRS Proceedings* **1535**, mmm12-a-0071 (2013).

J. Kundin, M. A. Choudhary and H. Emmerich  
Bridging the phase-field and phase-field crystal approaches for anisotropic material systems  
*Eur. Phys. J. Special Topics* **223**, 363-372 (2014).

M. A. Choudhary, J. Kundin, M. Oettel and H. Emmerich  
Solid-liquid surface tensions of critical nuclei and nucleation barriers from a phase-field-crystal study of a model binary alloy using finite system sizes  
*Phys. Rev. E* **90**, 022403 (2014).

## List of Publications

---

M. A. Choudhary, J. Kundin and H. Emmerich

Investigation of the diffuse solid-liquid interface by mean of a phase-field crystal model

In prepration, (2016).

---

## Scientific award

First Poster Prize Winner

*Kinetic Seminar, Deutsche Gesellschaft für Kristallzüchtung und Kristallwachstum e. V. (DGKK), Bayreuth, 04 - 05 May 2015.*

## Contribution in scientific conferences (As an invited guest speaker)

M. A. Choudhary, Julia Kundin, Martin Oettel and H. Emmerich

"A phase-field crystal study of anisotropic crystals and binary alloys"

*Multiscale modeling of materials with atomic scale resolution using phase-field-crystal methods (MULTIMAT), Lausanne, Switzerland, 2014.*

M. A. Choudhary, J. Kundin, M. Oettel and H. Emmerich

"Integrated phase-field crystal approach to investigate interface tension and nucleation barriers"

*The 20th American Conference on Crystal Growth and Epitaxy (ACCGE), Big Sky, USA, 2015.*



---

## Contribution in scientific conferences

M. A. Choudhary, D. Li and H. Emmerich

"Investigation of an anisotropic phase-field crystal model"

*Frühjahrstagung der Deutsche Physikalische Gesellschaft (DPG)*, Dresden, Germany, 2011.

M. A. Choudhary, M. Oettel and H. Emmerich

"Aspects of phase-field crystal modeling: anisotropic crystals and eutectic mixtures"

*The 18th American Conference on Crystal Growth and Epitaxy (ACCGE)*, Monterey, USA, 2011.

M. A. Choudhary, M. Oettel, H. Emmerich and H. Löwen

"Investigating the process of crystal growth and successive microstructure formation within the frame work of phase-field crystal approach"

*Colloidal Dispersions in External Fields (CODEF - III)*, Bonn, Germany, 2012.

M. A. Choudhary, M. Oettel and H. Emmerich

"Modeling the crystal growth phenomena on atomistic scale in single crystals and binary alloys"

*Frühjahrstagung der Deutsche Physikalische Gesellschaft (DPG)*, Berlin, Germany, 2012.

M. A. Choudhary, Julia Kundin, M. Oettel and H. Emmerich

"A novel approach for the investigation of the materials parameters by means of PFC method"

*Materials Science Engineering (MSE)*, Darmstadt, Germany, 2012.

M. A. Choudhary, Julia Kundin, M. Oettel and H. Emmerich

"Phase-field crystal modeling of solid-liquid equilibria in binary alloys"

*Multiscale Material Modeling (MMM)*, Biopolis, Singapore, 2012.

M. A. Choudhary, Julia Kundin and H. Emmerich

"PFC modeling of crystal growth phenomena on the atomic scale"

*European Congress and Exhibition on Advance Material and Processes (EURO-MAT)*, Sevilla, Spain, 2013.

## List of Publications

---

M. A. Choudhary, Julia Kundin and H. Emmerich

"Modeling phase transformations in binary alloys for eutectic systems"

*Frühjahrstagung der Deutsche Physikalische Gesellschaft (DPG)*, Dresden, Germany, 2014.

M. A. Choudhary, J. Kundin, M. Oettel and H. Emmerich

"Phase equilibria and interfacial properties of a curved liquid-solid interface"

*Frühjahrstagung der Deutsche Physikalische Gesellschaft (DPG)*, Berlin, Germany, 2015.

# Curriculum vitae

## **PERSÖNLICHE ANGABEN**

---

Name: Muhammad Ajmal Choudhary

Staatsangehörigkeit: Pakistan

Geburtsdatum: 18.01.1985

Geburtsort: Sargodha / Pakistan

## **AUSBILDUNG UND BERUFLICHER WERDEGANG**

---

2002	Higher Secondary School Certificate ABICS, Pakistan
2002 – 2006	Bachelor of Science in Mechanical Engineering GIK Institute of Engineering Science and Technology, Pakistan
2006 – 2007	Master of Science in Mechanical Engineering with specialization in Engineering Mechanics Royal Institute of Technology (KTH), Sweden
2007 – 2009	Master of Science in Computational Mechanics of Materials and Structures Universität Stuttgart, Germany.
2012	Beginn der Promotion am Lehrstuhl für Material- und Prozesssimulation, Universität Bayreuth

Muhammad Ajmal Choudhary

in Februar 2016